A single-cell transcriptomic and anatomic atlas of mouse dorsal raphe *Pet1* neurons

Authors: Benjamin W. Okaty*#, Nikita Sturrock*, Yasmin Escobedo Lozoya, YoonJeung Chang, Rebecca A. Senft, Krissy A. Lyon, Olga V. Alekseyenko, Susan M. Dymecki#

Department of Genetics, Harvard Medical School, Boston, MA, USA.

* These authors contributed equally

Corresponding Authors

Abstract

Among the brainstem raphe nuclei, the dorsal raphe nucleus (DR) contains the greatest number of *Pet1*-lineage neurons, a predominantly serotonergic group distributed throughout DR subdomains. These neurons collectively regulate diverse physiology and behavior and are often therapeutically targeted to treat affective disorders. Characterizing *Pet1* neuron molecular heterogeneity and relating it to anatomy is vital for understanding DR functional organization, with potential to inform therapeutic separability. Here we use high-throughput and DR subdomain-targeted single-cell transcriptomics and intersectional genetic tools to map molecular and anatomical diversity of DR-*Pet1* neurons. We describe up to fourteen neuron subtypes, many showing biased cell body distributions across the DR. We further show that *P2ry1-Pet1* DR neurons – the most molecularly distinct subtype – possess unique efferent projections and electrophysiological properties. These data complement and extend previous DR characterizations, combining intersectional genetics with multiple transcriptomic modalities to achieve fine-scale molecular and anatomic identification of *Pet1* neuron subtypes.

Introduction

Brainstem neurons that synthesize the monoamine neurotransmitter serotonin (5-hydroxytryptamine, 5-HT) (Baker et al., 1991a; Baker et al., 1991b; Baker et al., 1990; Dahlstroem and Fuxe, 1964; Ishimura et al., 1988; Steinbusch, 1981; Steinbusch et al., 1978) derive from embryonic precursors that express the transcription factor PET1 (alias FEV) upon terminal cell division (Hendricks et al., 1999). PET1 shapes the serotonergic identity of neurons by regulating expression of genes required for 5-HT biosynthesis, packaging in synaptic vesicles, reuptake, and metabolism (Hendricks et al., 2003; Krueger and Deneris, 2008; Liu et al., 2010; Wyler et al., 2015; Wyler et al., 2016), though some *Pet1*-lineage cells in the brain have ambiguous phenotypes with respect to their ability to synthesize and release 5-HT (Alonso et al., 2013; Barrett et al., 2016; Okaty et al., 2015; Pelosi et al., 2014; Sos et al., 2017). Aside from shared expression of 5-HT marker genes (to varying degrees), *Pet1*-lineage neurons display wide-ranging phenotypic heterogeneity, including diverse brainstem anatomy, hodology, and expression of neurotransmitters in addition to or other than 5-HT, suggestive of distinct *Pet1* neuron subtypes with divergent neural circuit functions (recently reviewed in (Okaty et al., 2019)). We have previously shown that the mature molecular identities of *Pet1*-lineage neurons strongly correlate with both the embryonic progenitor domain (rhombomeric domain) from which they derive and with their mature anatomy (Jensen et al., 2008; Okaty et al., 2015), largely consistent with (Alonso et al., 2013). However, even within a given *Pet1* rhombomeric sublineage and anatomical subdomain, *Pet1* neurons may display different molecular and cellular phenotypes (Niederkofler et al., 2016; Okaty et al., 2015). *Pet1* neurons project widely throughout the brain and are functionally implicated in numerous life-sustaining biological processes and human pathologies. Thus, assembling a taxonomy of *Pet1* neuron subtypes based on molecular and cellular properties and linking identified *Pet1* neuron subtypes to specific biological functions is important for basic neuroscience and human health, including the development of targeted therapeutics. Here we provide a high-resolution, single-cell transcriptomic atlas of dorsal raphe *Pet1*-lineage neurons revealing hierarchically and spatially organized molecular subtypes, each expressing unique repertoires of neurotransmitters, plasma membrane receptors, ion channels, cell adhesion molecules, and other gene categories important for specifying neuronal functions.

61 The dorsal raphe (DR) nucleus comprises the largest anatomically defined subgroup of
62 *Pet1* expressing cells in the brain, and these cells are derived from embryonic
63 progenitors in the isthmus and rhombomere 1 (Alonso et al., 2013; Jensen et al., 2008).
64 Multiple studies have demonstrated neuronal diversity within the DR, in *Pet1*-expressing
65 5-HT neurons as well as other resident cell populations (Calizo et al., 2011; Challis et al.,
66 2013; Crawford et al., 2010; Fernandez et al., 2016; Huang et al., 2019; Kirby et al.,
67 2003; Niederkofler et al., 2016; Prouty et al., 2017; Ren et al., 2018; Ren et al., 2019;
68 Spaethling et al., 2014; Vasudeva and Waterhouse, 2014; Zeisel et al., 2018). In the
69 present study, we extend these findings by transcriptionally profiling *Pet1*-lineage
70 marked DR neurons using microfluidic cell sorting and droplet-based single-cell RNA
71 sequencing (scRNA-seq). Our particular experimental approach combining intersectional
72 mouse genetics, high-throughput cell-type-specific purification (using the On-chip Sort),
73 and newly improved scRNA-seq library construction chemistry (using the 10X Genomics
74 Chromium Single Cell 3' v3 kit) allowed us to surpass prior resolution of DR *Pet1* neuron
75 molecular diversity, both in terms of the number of DR *Pet1* cells profiled and the
76 number of transcriptomically distinct *Pet1* neuron subtypes identified. To further
77 characterize the anatomical organization of these molecularly defined *Pet1* neuron
78 subtypes, we used intersectional mouse transgenic tools, crossing *Pet1::Flpe* mice with
79 various subtype-relevant Cre-driver mice and dual Flpe- and Cre-responsive fluorescent
80 reporter lines. In addition to performing histological analyses of these intersectionally
81 defined *Pet1*-lineage neuron subpopulations, we further characterized them using
82 manual cell-sorting from microdissected subdomains of the DR followed by scRNA-seq.
83 Comparing this data with our high-throughput droplet-based scRNA-seq approach
84 allowed us to map *Pet1* neuron molecular diversity onto DR anatomy. We found that DR
85 *Pet1*-lineage neurons comprise as many as fourteen distinct molecularly defined
86 subtypes, several of which we show are anatomically biased within rostral-caudal,
87 dorsal-ventral, and medial-lateral axes. Additionally, by combining intersectional genetics
88 with projection mapping and *ex vivo* slice electrophysiology we show examples of
89 distinct *Pet1* neuron molecular subtypes that also differ in other cellular phenotypes
90 important for function, such as hodology and electrophysiology.

91 **Results**

92 **Droplet-based scRNA-seq of *Pet1* fate-mapped DR neurons reveals new**
93 **molecularly defined neuron subtypes**

94 To characterize the molecular diversity of *Pet1*-lineage DR neurons in a targeted, high-
95 throughput, high-resolution manner we partnered recombinase-based genetic fate
96 mapping, microfluidic fluorescence-based cell sorting, and droplet-based single-cell
97 barcoding followed by RNA-seq library preparation and next-generation sequencing
98 using the 10X Genomics Chromium Single Cell 3' v3 kit (**Figure 1A; Methods**).
99 Fluorescent labeling of *Pet1*-lineage DR neurons was achieved in mice of the following
100 genotypes: (1) *Pet1::Flpe* (Jensen et al., 2008); *En1::cre* (Kimmel et al., 2000);
101 *RC::FrePe* (the latter transgene a dual Flpe- and Cre-dependent fluorescent reporter
102 inserted into the *ROSA26* (*R26*) locus (Brust et al., 2014; Dymecki et al., 2010; Okaty et
103 al., 2015)), in which *Pet1*-lineage neurons derived from the *En1*$^+$ isthmus and
104 rhombomere 1 (r1) embryonic progenitor domains are marked by EGFP expression or
105 (2) *Pet1::Flpe; RC*::*FL-hM3Dq* (Sciolino et al., 2016), in which all *Pet1* neurons are
106 EGFP-labeled (Cre was not utilized in these experiments, thus only EGFP, not hM3Dq,
107 was expressed).

108 Brains were acutely dissected from 6-10 week old mice of both genotypes (4 males and
109 6 females), and DR cells were dissociated as previously described (Okaty et al., 2015)
110 (also see **Methods**). EGFP-expressing neurons were selectively purified using the On-
111 chip Sort (On-chip Biotechnologies Co., Ltd.), a recently developed technology that
112 greatly reduces the pressure forces typically exerted on cells in conventional flow
113 sorters, thereby achieving higher levels of cell viability (Watanabe et al., 2014). Indeed,
114 examination of sorted neurons revealed that many still had intact processes emanating
115 from their somas. Cells were then run through the 10X Genomics Chromium Single Cell
116 3' v3 protocol, followed by Illumina NextSeq 500 sequencing. The Cell Ranger pipeline
117 was used for transcript mapping and single-cell de-multiplexing, and all analyses of
118 transcript counts were performed using the R package Seurat (Butler et al., 2018; Stuart
119 et al., 2019) (also see **Methods**). After stringently filtering out "suspect" single-cell
120 libraries (e.g. libraries with high levels of non-neuronal or mitochondrial genes, outlier
121 library complexity, or absence/low levels of *Pet1* transcripts), we obtained 2,350 single
122 cells for further analysis, with a mean of 7,521 genes detected per single cell library
123 (mean of 57,678 UMIs per cell), and a total of 17,231 genes detected in aggregate (after
124 filtering out genes that were expressed in fewer than ten cells).

125 As the principal goal of our scRNA-seq experiments was to characterize molecular
126 diversity of *Pet1*-lineage neurons, our analyses were aimed at identifying genes with

127 significantly variable transcript expression across single neurons, and using these gene
128 expression differences to classify *Pet1*-lineage neuron subtypes. Typical clustering
129 approaches used to classify cell types (or cell states) based on scRNA-seq data are
130 largely unsupervised, but do require supervised input regarding a number of parameters
131 that have the potential to significantly alter the resulting cluster assignments. These
132 parameters include the data reduction used prior to clustering (such as principal
133 components analysis), the number of components included in the reduction, and a
134 resolution or granularity parameter that determines the "community" size of clusters (i.e.
135 whether cluster boundaries are more or less inclusive; coarse-grained or fine-grained).
136 Rather than arbitrarily choosing a set of parameters for our *Pet1*-lineage neuron subtype
137 classification, we chose a more exploratory approach by systematically varying key
138 parameters and examining how sensitive the resulting clusters were to these
139 combinations of parameters.

140 First, single-cell transcript counts were log-normalized, and we carried out principal
141 components analysis (PCA) on the scaled and centered expression values of the top two
142 thousand genes with the highest variance (after applying a variance-stabilizing
143 transform, see **Methods**) in order to reduce the dimensionality of the data onto a smaller
144 set of composite variables that represent the most salient gene expression differences.
145 Plotting the variance explained by each principal component we observed an inflection
146 point, or "elbow", around the fiftieth component suggesting a drop-off in the information
147 content of subsequent components (**Figure 1–figure supplement 1A**), and found that
148 roughly forty percent of the total variance was explained by these first fifty components.
149 Further examination of the gene loadings of each component revealed that components
150 six and seven were heavily weighted towards sex-specific transcripts and transcripts that
151 largely correlated with batch. As our experiments were not designed to explicitly
152 compare sex as a variable, and given the difficulties of interpreting batch-correlated
153 gene expression differences (e.g. these could stem from population sampling biases of
154 the different cell sorts, different genotypes used, different balance of sexes, or any
155 number of idiosyncratic biological and technical differences) we ultimately chose to
156 remove components six and seven from downstream analyses (though we found that
157 their inclusion had only modest effects on data clustering).

158 Next, we varied: (1) the number of PCs included in the data reduction (from one to fifty,
159 excluding PCs six and seven) used as input to the Seurat FindNeighbors function, and

160 (2) the resolution parameter in the Seurat FindClusters function (from 0.1 to 2.0, in
161 intervals of 0.1, using the Louvain algorithm). The results of this analysis are
162 summarized in the heatmap in **Figure 1–figure supplement 1B**. Including only the first
163 few principal components led to highly variable numbers of clusters depending on the
164 resolution parameter (resulting in as many as 40 clusters at the highest resolution).
165 However, for all resolutions the number of clusters mostly stabilized after including the
166 first thirty PCs. In this regime of parameter space the number of clusters was, for the
167 most part, bounded between five and twenty depending on the resolution. As a first pass
168 at homing in on the "optimum" number of clusters (strictly in a heuristic sense), we
169 calculated the frequency of obtaining a given number of clusters over all combinations of
170 parameters, reasoning that cluster numbers that are less sensitive to precise tuning of
171 parameters would appear more frequently, and the "robustness" of these cluster
172 numbers might more faithfully reflect biologically meaningful subgroup structure in the
173 data. The cluster number frequency plot in **Figure 1–figure supplement 1C** shows that
174 there are four local maxima and one global maximum corresponding to five, eight,
175 eleven, fourteen, and seventeen clusters respectively. Given the high frequency of these
176 cluster numbers, we chose to examine their composition more carefully. As multiple
177 combinations of parameters lead to the same number of clusters (**Figure 1–figure**
178 **supplement 1D**), in some cases leading to differences in cluster composition (generally
179 subtle), we decided to err on the side of including more data and thus fixed the number
180 of PCs at one to fifty, excluding PCs six and seven, and varied the resolution to obtain
181 five, eight, eleven, fourteen, and seventeen clusters.

182 We characterized cluster structure through hierarchical dendrograms, uniform manifold
183 approximation and projection for dimension reduction (UMAP) (a technique recently
184 developed by McInness, Healy, and Melville as described in a manuscript available at
185 arXiv.org, and implemented in Seurat), and differential expression analysis using
186 Wilcoxon rank-sum tests to identify transcripts that are significantly enriched or depleted
187 among clusters (**Figure 1–figure supplement 2A-I**, **Figure 1 B-D**). We ultimately
188 judged seventeen clusters (resolution = 1.5) to be excessive, due to the inclusion of
189 clusters with very few enriched genes as well as clusters that appeared somewhat
190 intermixed in UMAP space (analysis not shown). We thus focused our analyses on lower
191 resolution clusters. Across all resolutions analyzed (0.1, 0.3, 0.7, and 0.9), we found a
192 common set of genes that was useful in characterizing cluster structure, namely *Tph2,*

193 *Gad2, Gad1, Slc17a8 (*alias *Vglut3*)*,* and *Met*. The *Tph2* gene encodes for tryptophan
194 hydroxylase 2, the rate-limiting enzyme involved in 5-HT biosynthesis in the central
195 nervous system (Walther and Bader, 2003; Walther et al., 2003), and all but one cluster
196 showed consistently high *Tph2* transcript expression. In the five- and eight-cluster-
197 number analyses (resolution = 0.1 and 0.3, respectively), one cluster displayed a
198 strikingly bi-modal distribution of *Tph2* transcript expression (**Figure 1–figure**
199 **supplement 2A, D**, clusters four and six, respectively), however increasing the
200 resolution further divided this group into a *Tph2*-low group (**Figure 1–figure**
201 **supplement 2G** and **Figure 1B**, clusters eight and thirteen, respectively, corresponding
202 to resolutions of 0.7 and 0.9) and a *Tph2*- "variable" group, displaying a broader
203 distribution of single-cell expression than other clusters (**Figure 1–figure supplement**
204 **2G** and **Figure 1B**, clusters ten and fourteen, respectively). Beyond *Tph2* expression,
205 cluster thirteen (and to a lesser extent cluster fourteen) displayed lower and more
206 variable expression of several 5-HT neuron marker genes (**Figure 1–figure supplement**
207 **3**). Interestingly, we found that expression of these genes was significantly correlated
208 with the level of *Pet1* expression in these cells (**Figure 1–figure supplement 4**),
209 consistent with demonstrated transcriptional regulation of 5-HT terminal identity markers
210 by PET1 (Hendricks et al., 2003; Krueger and Deneris, 2008; Liu and Deneris, 2011;
211 Spencer and Deneris, 2017; Wyler et al., 2015; Wyler et al., 2016).

212 *Gad1* and *Gad2* are paralogous genes that encode two distinct forms of the gamma-
213 aminobutyric acid (GABA) synthetic enzyme glutamate decarboxylase (Erlander et al.,
214 1991), and we found a sizable group of *Pet1* neurons (~50%) that express high levels of
215 *Tph2* and *Gad2*, and to a lesser extent *Gad1* (generally detected in fewer cells than
216 *Gad2*) (**Figure 1 – figure supplement 2A, B**, clusters one and two), which could be
217 further subdivided into five sub-clusters at finer resolution (**Figure 1B, C,** clusters two-
218 six**)**. One of these clusters, cluster six (**Figure 1B,C**), contained *Pet1* neurons
219 additionally expressing intermediate levels of transcripts for *Vglut3,* encoding the
220 vesicular glutamate transporter 3 (Fremeau et al., 2002; Gras et al., 2002). Notably, this
221 group of neurons also had the highest expression of *Gad1* relative to other groups. High
222 expression levels of *Vglut3* transcripts were detected in ~46% of profiled *Pet1* neurons,
223 comprising eight clusters at finer resolution (**Figure 1B, C,** clusters seven to fourteen), ,
224 including the *Tph2*-low and *Tph2*-variable clusters (**Figure 1B, C,** clusters 13 and 14).
225 The most striking outlier group of *Pet1* neurons (cluster twelve in **Figure 1B, C**) is

226 characterized by high transcript expression of *Tph2*, *Vglut3,* and *Met,* the latter encoding
227 the MET proto-oncogene (also known as hepatocyte growth factor receptor) (Iyer et al.,
228 1990). This group of cells consistently clustered separately from all other groups at all
229 resolutions analyzed (**Figure 1 – figure supplement 2**). At the finest resolution of 0.9,
230 the remaining 4% of *Pet1* neurons, comprising cluster one, expressed high levels of
231 *Tph2* transcripts but only sporadically expressed transcripts for *Gad2*, *Gad1*, or *Vglut3*
232 (**Figure 1B,C**).

233 Examination of the dendrogram in **Figure 1B** and the UMAP plot in **Figure 1C** (as well
234 as examining the successively parcelled UMAP clusters in **Figure 1–figure supplement**
235 **2B, E, and H** with increasing resolution) gives a sense of "relatedness" among clusters.
236 For example, *Gad1/2-Tph2* clusters two to four are more similar to each other than to
237 *Vglut3-Tph2* clusters, while cluster six, the *Gad1/2-Vglut3-Tph2* cluster, and cluster five
238 are situated between the other *Gad1/2-Tph2* and *Vglut3-Tph2* groups. Like cluster
239 twelve, clusters thirteen and fourteen appear as outliers from the other clusters in the
240 dendrogram (**Figure 1B)**, but despite showing low and variable expression of the 5-HT
241 neuron marker gene *Tph2*, respectively, they nonetheless cluster more closely to other
242 *Pet1* neurons than do *Met-Vglut3-Tph2-Pet1* neurons (cluster twelve) in the UMAP plot
243 (**Figure 1C)**.

244 *Met*-expressing *Pet1* neurons have been previously reported in mice, both at the
245 transcript and protein levels, specifically in the caudal DR and the median raphe (MR)
246 (Kast et al., 2017; Okaty et al., 2015; Wu and Levitt, 2013) and more recently (Huang et
247 al., 2019; Ren et al., 2019). Likewise, *Vglut3-* and *Gad1/2*-expressing DR *Pet1* neurons
248 have been previously reported in mice and rats, as demonstrated by mRNA *in situ*,
249 immunocytochemistry, and RNA-seq (Amilhon et al., 2010; Commons, 2009; Fu et al.,
250 2010; Gagnon and Parent, 2014; Gras et al., 2002; Herzog et al., 2004; Hioki et al.,
251 2004; Hioki et al., 2010; Huang et al., 2019; Okaty et al., 2015; Ren et al., 2018; Ren et
252 al., 2019; Rood et al., 2014; Shikanai et al., 2012; Spaethling et al., 2014; Voisin et al.,
253 2016). Consistent with functional expression of VGLUT3, which allows for filling of
254 synaptic vesicles with the excitatory neurotransmitter glutamate, depolarization-induced
255 glutamate release by DR *Pet1*/5-HT neurons has been demonstrated by a number of
256 groups (Johnson, 1994; Kapoor et al., 2016; Liu et al., 2014; Sengupta et al., 2017;
257 Wang et al., 2019). Additionally, VGLUT3 is thought to interact with vesicular
258 monoamine transporter two (encoded by *Slc18a2,* alias *Vmat2* (Erickson et al., 1992)) to

259 enhance the loading of 5-HT into synaptic vesicles by increasing the pH gradient across
260 vesicular membranes, a process referred to as “vesicle-filling synergy” (Amilhon et al.,
261 2010; El Mestikawy et al., 2011; Munster-Wandowski et al., 2016). GABA-release by
262 *Pet1* DR neurons, on the other hand, has not been reported, thus the functional
263 consequences of *Gad1* and *Gad2* transcript expression are presently unknown.

264 **Differentially expressed genes span functional categories relevant to neuronal**
265 **identity**

266 Scaled expression of the top five marker genes for each cluster (ranked by Bonferroni
267 corrected p-value or in some cases fold enrichment) are represented in the heatmaps in
268 **Figure 1–figure supplement 2C, F, I**, and **Figure 1D,** depending on the cluster
269 resolution. For all further analyses, we chose to focus on the 0.9 resolution clustering, as
270 we felt that these fourteen clusters did the best job of parcellating UMAP space. For
271 example, visually-distinguishable groups of cells, like clusters five and six, clusters ten
272 and eight, and clusters seven and fourteen, are each consolidated into a single cluster at
273 resolution = 0.7. While sharing some similarities, these groups differ in the expression of
274 many genes, to an extent that we felt constituted separate classification as supported by
275 the resolution = 0.9 analysis. To aid interpretation of the functional significance of
276 differentially expressed genes, expression patterns of a subset of significantly variable
277 genes and cluster markers are represented in the dot plots in **Figure 2**, organized by
278 categories of biological function (identified by Gene Ontology annotations and literature
279 searches). These gene categories were selected based on general importance for
280 shaping neuronal functional identity – e.g. genes that encode transcription factors which
281 broadly regulate molecular phenotypes, as well as genes that encode ion channels,
282 plasma membrane receptors, calcium-binding proteins, kinases, and cell adhesion and
283 axon guidance molecules, which collectively govern neuronal electrophysiology, signal
284 transduction, and synaptic connectivity.

285 *Transcription Factors*

286 History of expression of *Pet1/Fev,* encoding the FEV transcription factor, ETS family
287 member (Fyodorov et al., 1998; Hendricks et al., 1999) defines the *Pet1* neuronal
288 lineage. As can be observed from the transcription factor dot plot in **Figure 2** (as well as
289 the violin plot in **Figure 1–figure supplement 3**), *Pet1/Fev* displays broad expression

290 across clusters but is expressed at significantly lower levels in cluster thirteen *Pet1*
291 neurons. Several genes known to be directly regulated by *Pet1* (Hendricks et al., 2003;
292 Liu et al., 2010; Wyler et al., 2015; Wyler et al., 2016), such as *Tph2*, *Slc6a4* (*Sert*)
293 (encoding the serotonin transporter (Hoffman et al., 1991; Lesch et al., 1993)), and
294 *Slc18a2* (*Slc18a2*) likewise show reduced expression in cluster thirteen. The
295 transcription factor engrailed 1 (*En1*) (Joyner et al., 1985), in its expression overlap with
296 *Pet1,* is a marker of having derived from progenitors in the isthmus and r1 (Alonso et al.,
297 2013; Jensen et al., 2008; Okaty et al., 2015), and, as expected, *En1* transcripts are
298 detected broadly across all DR clusters. The paralogous gene engrailed 2 (*En2*) (Joyner
299 and Martin, 1987), shows a more variable expression profile across *Pet1* DR neurons,
300 being largely absent in cluster eight and twelve, and significantly lower in cluster seven.
301 *En1* and *En2* are required for normal development of DR *Pet1* neuron cytoarchitecture
302 and for perinatal maintenance of serotonergic identity (Fox and Deneris, 2012). *Nr3c1*,
303 encoding the nuclear receptor subfamily 3, group C, member 1, aka the glucocorticoid
304 receptor, which binds the stress hormone corticosterone (cortisol in humans), is
305 expressed broadly across clusters one through eleven, but is de-enriched in cluster
306 twelve, and to a lesser extent clusters thirteen and fourteen, suggesting differential
307 sensitivity to corticosterone across different *Pet1* neuron molecular subtypes. Numerous
308 studies have highlighted the functional importance of DR glucocorticoid signaling for 5-
309 HT neuron activity and behavioral modulation (Bellido et al., 2004; Evrard et al., 2006;
310 Judge et al., 2004; Laaris et al., 1995; Vincent et al., 2018; Vincent and Jacobson,
311 2014).

312 Other transcription factor encoding genes show more striking expression specificity.
313 Transcripts for neuronal pas domain 1 and 3 (encoded by *Npas1* and *Npas3*) and POU
314 class 3 homeobox 1 (*Pou3f1*) are significantly enriched in cluster one *Pet1* neurons.
315 From mouse genetic studies, both NPAS1 and NPAS3 are associated with regulation of
316 genes and behavioral endophenotypes implicated in psychiatric disorders, such as
317 schizophrenia, though NPAS1/3 are also expressed by other cell types in the brain, such
318 as cortical interneurons, which may contribute to observed behavioral effects of *Npas1/3*
319 loss of function (Erbel-Sieler et al., 2004; Michaelson et al., 2017; Stanco et al., 2014).

320 *Pax5*, encoding paired box 5 (Asano and Gruss, 1992), a transcription factor involved in
321 the regulation of isthmic organizer activity during development (Funahashi et al., 1999;
322 Ye et al., 2001) is significantly enriched in clusters two, four, and five, and highly

323 expressed in clusters three and six as well. *Pou6f2* (POU class 6 homeobox 2) and *Klf5*
324 (Kruppel like factor 5) show a similar pattern of expression. *Sox14* (SRY-box
325 transcription factor 14) and *Satb2* (SATB homeobox 2) show an even more restricted
326 expression profile, limited to clusters two through four. Notably, clusters two through six
327 are also enriched for expression of *Gad2*, which, like *Sox14*, is most highly expressed in
328 cluster four. *Sox14* expression has been shown to regulate GABAergic cell identity in the
329 dorsal midbrain (Makrides et al., 2018), and *Pax5* expression has been implicated in
330 GABAergic neurotransmitter specification in the dorsal horn of the spinal cord (Pillai et
331 al., 2007), suggesting that these genes may play similar roles in DR *Pet1* neurons.
332 Interestingly, *Nr2f2* (encoding nuclear receptor subfamily 2, group F, member 2, alias
333 COUP-TFII) shows an expression profile that is complementary to *En2* and *Pax5,*
334 enriched in cluster eight, nine, and twelve, all of which are enriched for *Vglut3*
335 transcripts, and are largely devoid of *Gad1/2* expression.

336 Overall, each of the fourteen transcriptome-defined clusters of DR *Pet1* neurons can
337 largely be classified by the combinatorial expression of two to three transcription factors.
338 For example, *Pou3f2* (POU class three homeobox 2), *Bcl11a* (B cell CLL/lymphoma 11A
339 zinc finger protein), and *Id2* (inhibitor of DNA binding 2) show enriched expression in
340 cluster six, and to a lesser extent cluster thirteen. Other notable transcription factor
341 markers of *Pet1* neuron subgroups include *Foxp1* (forkhead box P1), enriched in
342 clusters seven and fourteen, *Rorβ* (RAR-related orphan receptor beta), enriched in
343 cluster eight, *Maf* (avian musculoaponeurotic fibrosarcoma oncogene homolog),
344 enriched in cluster nine, *Foxa1* (forkhead box A1), enriched in cluster eleven, *Zeb2* (zinc
345 finger E-box binding homeobox 2) enriched in cluster twelve, *Zfp536* (zinc finger protein
346 536), *Nfix* (nuclear factor I/X), and *Nfib* (nuclear factor I/B), enriched in cluster thirteen
347 (detected in cluster six as well), and *Ldb2* (LIM domain binding 2), enriched in clusters
348 thirteen and fourteen.

349 *Neurotransmitters and Neuropeptides*

350 *Pet1* neuron subtypes defined by transcriptomic clustering also show differential
351 expression of a number of neurotransmitter-related and neuropeptide-encoding genes
352 (**Figure 2** Neurotransmitters and Neuropeptides dot plot). Transcript profiles related to
353 classic neurotransmitter production, including *Tph2, Gad2, Gad1,* and *Slc17a8,* have
354 already been described above (see also **Figure 1B**). Transcript expression of *Trh*,

355 encoding thyrotropin-releasing hormone, is significantly enriched in cluster two *Pet1*
356 neurons and detected in clusters four and six (**Figure 1D** and **Figure2**). Another gene
357 involved in thyroid hormone signaling, *Crym*, encoding crystalline mu, also known as
358 NADP-regulated thyroid-hormone-binding protein shows a similar expression profile
359 (**Figure 1D**). *Pdyn*, encoding the preprohormone prodynorphin is enriched in clusters
360 five, six, and fourteen. Prodynorphin is the precursor protein to the opioid polypeptide
361 dynorphin, which predominately binds the kappa-opioid receptor to produce a variety of
362 effects, such as analgesia and dysphoria (Bruchas et al., 2010; Chavkin et al., 1982;
363 Land et al., 2008; Land et al., 2009). Expression of *Nos1*, encoding nitric oxide synthase
364 1, is significantly enriched in cluster five, nine, and eleven. The anatomical distribution of
365 nitric oxide expressing DR 5-HT neurons in rodents has been characterized previously
366 as being predominately midline in the DR (Fu et al., 2010; Prouty et al., 2017; Vasudeva
367 et al., 2011; Vasudeva and Waterhouse, 2014). Cluster nine also shows enriched
368 expression of *Crh*, encoding corticotropin-releasing hormone. Several other
369 neuropeptide encoding genes show sporadic, significantly variable expression among
370 different clusters, including growth hormone-releasing hormone (*Ghrh),* neuromedin B
371 (*Nmb),* neuropeptide B (*Npb),* proenkephalin (*Penk),* and somatostatin (*Sst).*

372 *Ionotropic and G-Protein Coupled Receptors*

373 Cluster one and cluster thirteen *Pet1* neurons show the most prominent specificity with
374 respect to ionotropic receptor markers (**Figure 2 Ionotropic Receptors**), though in
375 general we found relatively few *Pet1* neuron subtype-specific ionotropic gene markers
376 relative to other categories of gene function. *Gabrq* and *Gabre*, encoding GABA type A
377 receptor subunits theta and epsilon, respectively, are significantly enriched in cluster
378 one, as well as *Gria1,* encoding glutamate ionotropic receptor AMPA type subunit 1.
379 GABA type A receptor subunit gamma3 (*Gabrg3*) and glutamate ionotropic receptor
380 NMDA type subunit 2A (*Grin2a*) transcripts are largely de-enriched in clusters two
381 through four and twelve, are significantly enriched in cluster nine, and variably
382 expressed in other clusters. GABA A receptor subunit alpha 2 (*Gabra2*) is expressed in
383 all clusters but is significantly enriched in cluster twelve, and GABA A receptor subunit
384 alpha 1 (*Gabra1*) and glutamate ionotropic receptor AMPA type subunit 3 (*Gria3*)
385 transcripts both show significant enrichment in cluster thirteen.

386 Transcripts encoding G protein-coupled receptors (GPCRs) show patterns of enrichment
387 largely across blocks of clusters (e.g. *Vglut3*-expressing versus non-*Vglut3*-expressing
388 *Tph2-Pet1* neurons), or highly specific enrichment in either cluster twelve or clusters
389 thirteen and fourteen (**Figure 2 G Protein-coupled Receptors**). For example, cluster
390 twelve neurons show strong enrichment for opioid receptor mu (*Oprm1*), purine receptor
391 y1 (*P2ry1)*, relaxin receptor (*Rxfp1)*, sphingosine-1-phosphate receptor *3* (*S1pr3*), and
392 tachykinin receptor 3 (*Tacr3)* transcripts. Moreover, they lack expression of transcripts
393 for many GPCRs expressed by the majority of other *Pet1* neurons, such as presynaptic
394 5-HT autoreceptors, encoded by *Htr1b* and *Htr1d*, as well as orexin and histamine
395 receptors (e.g. *Hcrtr1*, *Hcrtr2*, *Hrh1*, *Hrh3*), whose protein products are involved in the
396 regulation of arousal. We found that histamine receptor 1 (*Hrh1*) and hypocretin (alias
397 orexin) receptor 1 (*Hcrtr1*) transcripts were the most abundant in clusters one through
398 four, and histamine receptor 3 (*Hrh3*) transcripts were the most abundant in clusters two
399 through six. Hypocretin receptor 2 (*Hcrtr2*) transcripts showed a somewhat
400 complementary expression pattern, with the highest levels in clusters seven through
401 eleven, as well as cluster three. Other GPCR transcripts with notable expression
402 patterns are neuropeptide Y receptor Y2 (*Npy2r*), enriched in clusters seven and ten,
403 cannabinoid receptor 1 (*Cnr1*) and 5-HT receptor 2C (*Htr2c*), enriched in clusters
404 thirteen and fourteen, and *Gpr101*, an "orphan" GPCR thought to play a role in the
405 growth hormone releasing-growth hormone signaling axis (GHRH-GH axis) (Trivellin et
406 al., 2016; Trivellin et al., 2018), enriched in cluster fourteen.

407 *Regulators of Neuron Projections, Synaptic Connectivity, and Heparan Sulfate*
408 *Proteoglycans*

409 Similar to transcription factor expression patterns, most DR *Pet1* neuron subgroups can
410 be classified by combinatorial enrichment of transcripts for genes encoding regulators of
411 neuron projections and synaptic connectivity (**Figure 2 Regulators of Neuron**
412 **Projections and Synaptic Connectivity**). Differential expression of these genes likely
413 contributes to differential innervation patterns of distinct DR *Pet1* neuron subgroups,
414 such as reported by various studies (Fernandez et al., 2016; Huang et al., 2019; Kast et
415 al., 2017; Muzerelle et al., 2016; Niederkofler et al., 2016; Ren et al., 2018; Ren et al.,
416 2019; Teng et al., 2017), and yet to be uncovered. Genes encoding regulators of
417 heparan sulfate proteoglycans may also play a role in projection specificity and synaptic
418 organization (Condomitti and de Wit, 2018; Di Donato et al., 2018; Lazaro-Pena et al.,

419 2018; Minge et al., 2017; Zhang et al., 2018), and likewise show patterns of enrichment
420 across different *Pet1* neuron clusters (**Figure 2 Regulators of Heparan Sulfate**
421 **Proteoglycans**). For example, transcript expression of heparan sulfate-glucosamine 3-
422 sulfotransferase 4 (*Hs3st4*) is enriched across clusters one through four, heparan
423 sulfate-glucosamine 3-sulfotransferase 5 (*Hs3st5*) expression is significantly enriched in
424 cluster ten (and expressed at high levels in clusters one, eight, nine, and eleven), and
425 sulfatase 2 (*Sulf2*) and heparan sulfate-glucosamine 3-sulfotransferase 2 (*Hs3st2*)
426 transcripts are enriched in cluster thirteen.

427 **Intersectional genetic labeling of *Pet1* neuron subgroups in combination with**
428 **histology and manual scRNA-seq reveals spatial distributions of DR *Pet1* neuron**
429 **subtypes**

430 Having identified transcriptomically distinct DR *Pet1* neuron subtypes in a largely
431 unsupervised manner, we next sought to determine whether the cell bodies of these
432 molecularly defined *Pet1* neuron subtypes show differential distributions within
433 anatomical subfields of the DR. Using intersectional genetics to fluorescently label *Pet1*
434 neuron subgroups defined by pairwise expression of *Pet1* and one of an assortment of
435 identified subtype marker genes, we iteratively mapped molecular subtypes to anatomy
436 in two ways – (1) using histology and microscopy to directly characterize cell body
437 locations in fixed brain sections (**Figure 3**), and (2) performing manual scRNA-seq on
438 labeled cells dissociated and hand sorted from microdissected anatomical subdomains
439 of the DR, and comparing these expression profiles to our above described high-
440 throughput scRNA-seq data (which we will refer to as our 10X scRNA-seq data) (**Figure**
441 **4**). We iteratively bred triple transgenic mice harboring (1) our *Pet1::Flpe* transgene, (2)
442 one of two dual Flpe- and Cre- responsive reporter constructs (*RC::FrePe* or *RC*::*FL-*
443 *hM3Dq*), and (3) one of five Cre-encoding transgenes (*Sert::cre*, *Vglut3::IRES-cre*,
444 *Npy2r::IRES-cre*, *Crh::cre*, or *P2ry1::IRES-cre*), where *cre* expression is driven by either
445 the endogenous promoter of the marker gene or by a gene-specific bacterial artificial
446 chromosome (BAC). In selecting candidate markers from our list of differentially
447 expressed genes, we sought gene drivers that could potentially divide *Pet1* neurons into
448 subgroups at varying resolutions and were available as *cre* lines. Representative
449 images for each triple transgenic genotype are given in **Figure 3** (organized by marker
450 genes, columns A-E, at different rostrocaudal levels of the DR, rows 1-6). For each
451 genotype, the intersectionally defined subpopulation of neurons is labeled in green (i.e.

452 history of Flpe and Cre expression) whereas the “subtractive” subpopulation is labeled in
453 red (i.e. history of Flpe but not Cre expression).

454 *Histology of Pet1-Intersectionally Defined Neuron Populations*

455 High *Sert* expression, like high *Tph2* expression, defines *Pet1* neuron clusters one
456 through eleven. Cluster twelve shows consistently lower mean expression of *Sert*
457 transcripts (and to a lesser extent *Tph2* transcripts) than clusters one through eleven
458 (**Figure 3A**), cluster fourteen shows a broader distribution of *Sert* transcript levels
459 (**Figure 3A**) and many 5-HT markers (**Figure 1–figure supplement 3**), and cluster
460 thirteen shows very low levels of *Sert* transcripts (**Figure 3A**) and other 5-HT markers
461 (**Figure 1–figure supplement 3**). Consistent with the majority of profiled *Pet1* neurons
462 expressing high levels of *Sert* and *Pet1* transcripts, we detected intersectional
463 *Sert::cre;Pet1::Flpe* fluorescently marked neurons throughout the full rostrocaudal and
464 dorsoventral extent of the DR (**Figure 3A1-A6**), however the subtractive population
465 (presumably cluster thirteen and perhaps some cluster twelve and fourteen *Pet1*
466 neurons) showed a more limited distribution. These subtractive (Flpe+ but Cre-) neurons
467 were most conspicuously concentrated in the rostromedial DR (**Figure 3A2**), where only
468 a few *Sert::cre;Pet1::Flpe* intersectional (Flpe+ and Cre+) neurons were intermingled.
469 More caudally, the Flpe-only, subtractive neurons remained largely midline, but became
470 more intermixed with the double-positive *Sert::cre;Pet1::Flpe* intersectionally marked
471 cells. As another way of anatomically characterizing putative cluster thirteen *Pet1*
472 neurons, we immunostained for TPH2 in *En1::cre;Pet1::Flpe;RC::FrePe* mice (the same
473 genotype as used in some of our 10X scRNA-seq experiments), and found that the
474 distribution of TPH2 immunonegative *Pet1* neuron cell bodies showed a very similar
475 distribution to the subtractive neurons (Flpe-only) in *Sert::cre;Pet1::Flpe;RC::FrePe*
476 mice. (**Figure 3–figure supplement 1A**), further confirming the existence of *Pet1*-
477 expressing neurons that do not express TPH2 protein (Barrett et al., 2016; Pelosi et al.,
478 2014). To explicitly examine the relationship of *Tph2* transcript level to presence or
479 absence of TPH2 protein, we additionally performed concurrent TPH2 immunostaining
480 and *Tph2* single molecule fluorescent in situ hybridization in DR-containing brain
481 sections of an *En1::cre;Pet1::Flpe;RC::FrePe* mouse (**Figure 3–figure supplement 1B-**
482 **G**). Similar to our 10X scRNA-seq data, we found a bimodal distribution of *Tph2*
483 transcript abundance, with the majority of single cells distributing in the higher mode
484 (**Figure 3–figure supplement 1D**). Across all subregions of the DR analyzed, we found

485 that dual EGFP and TPH2 immunopositive cells contained significantly more *Tph2*
486 transcripts than EGFP immunopositive TPH2 immunonegative cells (p-value < 0.01,
487 Wilcoxon Rank Sum tests with Benjamini and Hochberg correction for multiple
488 comparisons, see **Methods, Figure 3–figure supplement 1E**). However, as the TPH2
489 immunopositive and negative *Tph2* transcript distributions showed some overlap, cells
490 with low *Tph2* transcript counts occasionally expressed TPH2 protein and cells with
491 higher transcript counts occasionally did not. In particular we found that the third and
492 fourth deciles (the "transition zone" between modes) of the *Tph2* transcript distribution
493 displayed the greatest degree of intermixing of TPH2 positive and negative cells (**Figure**
494 **3–figure supplement 1D**). Intriguingly, we also found that the somata of EGFP positive
495 TPH2 negative cells were significantly smaller than dual EGFP and TPH2 positive cells
496 (p-value < 0.01, Wilcoxon Rank Sum tests with Benjamini and Hochberg correction for
497 multiple comparisons**, Figure 3–figure supplement 1F,G).**

498 *Vglut3-Pet1* expression defines *Pet1* neuron clusters seven through fourteen, and to a
499 lesser extent cluster six (**Figure 3B**). We observed that *Vglut3::cre;Pet1::Flpe*
500 intersectionally marked neurons show a strong ventromedial bias in rostral portions of
501 the DR (**Figure 3B1-B3**), and are the predominant *Pet1* neuron subgroup in the more
502 caudal midline DR (**Figure 3B3-B6**). By contrast, the subtractive *Pet1* neuron subgroup
503 (presumably comprising *Pet1* neurons from clusters one through five and partly six)
504 show a strong dorsal and lateral bias and are largely absent from the most caudal
505 portions of the DR. We further characterized VGLUT3 protein expression in *Pet1*
506 neurons by VGLUT3 immunohistology in *Vglut3::IRES-cre;Pet1::Flpe; RC*::*FL-hM3Dq*
507 mice. We found consistent overlap between intersectional recombination marked
508 neurons and VGLUT3 protein expression, especially in medial, ventromedial, and caudal
509 portions of the DR (**Figure 3–figure supplement 1C-J**). In the dorsal and lateral
510 portions of the DR, however, where there are far fewer intersectionally labeled neurons,
511 we observed a small number of *Vglut3::cre;Pet1::Flpe* intersectionally marked neurons
512 that were negative for VGLUT3 antibody staining, suggesting transient expression of
513 *Vglut3* (and *Vglut3::IRES-cre)* by these cells at an earlier time in their developmental
514 history (or low *Vglut3* expression sufficient to drive Cre expression, but not VGLUT3
515 immunodetection).

516 Transcripts for *Npy2r*, encoding the neuropeptide Y receptor 2, are strongly enriched in
517 clusters six, seven, and ten, with less consistent expression in clusters eleven, thirteen,

518 and eight, and only sporadic expression elsewhere (**Figure 3C**). In mid-rostral portions
519 of the DR, we found that *Npy2r::cre;Pet1::Flpe* intersectionally marked cell bodies show
520 a largely midline bias, with a greater density of cells ventrally than dorsally, and the
521 occasional labeled cell body appearing more laterally (**Figure 3C2-C3**). In more caudal
522 extents of the DR, *Npy2r::cre;Pet1::Flpe* intersectionally marked cell bodies appear to be
523 concentrated more medially (**Figure 3C4-C6**).

524 Transcripts for *Crh*, encoding corticotropin-releasing hormone, are most highly enriched
525 in neurons comprising cluster nine and to a lesser extent cluster five, with sporadic
526 expression in other clusters (**Figure 3D**). *Crh::cre;Pet1::Flpe* intersectionally labeled
527 neurons do not show an obvious overall anatomical bias, distributing widely throughout
528 the DR (**Figure 3D1-D6**). At the most rostral levels of the DR, they appear to be more
529 consistently medially and ventrally localized (**Figure 3D1-D2**), but additionally appear in
530 the dorsal and lateral DR at mid-rostral levels, and are preferentially localized off the
531 midline more ventrally in these same sections (in regions sometimes referred to as the
532 ventrolateral wings) (**Figure 2D3-D4**). At the most caudal levels they distribute dorsally
533 and ventrally, with an apparent gap between these two domains (**Figure 3D5-D6**).

534 The most molecularly distinct *Pet1* neuron subtype we identified, cluster twelve *Met-*
535 *Vglut3-Tph2-Pet1* neurons, shows highly specific enrichment for a number of transcripts,
536 including *P2ry1*, encoding purinergic receptor P2Y1, which is only sporadically
537 expressed in other clusters (**Figure 3E**). *P2ry1::cre;Pet1::Flpe* intersectionally marked
538 neurons likewise show a strikingly unique anatomical distribution from the other
539 subgroups examined, being largely restricted to the caudal DR where they are densely
540 clustered dorsally, just beneath the aqueduct (**Figure 3E5-E6**). This is consistent with
541 previous characterizations of *Met*-expressing *Pet1/*5-HT neurons (Okaty et al., 2015; Wu
542 and Levitt, 2013), as well as other more recent characterizations (Huang et al., 2019;
543 Kast et al., 2017; Ren et al., 2019). Notably the distribution of *P2ry1::cre;Pet1::Flpe*
544 intersectional neurons within the cDR is distinct from *Npy2r:: cre;Pet1Flpe* intersectional
545 neurons, and only partially overlaps with where *Crh::cre;Pet1::Flpe* intersectional
546 neurons are found, arguing for *Pet1/*5-HT neuron subtype diversity within the caudal DR,
547 consistent with (Kast et al., 2017).

548 It should be noted that the precise anatomical boundaries of the caudal DR (cDR), also
549 referred to as B6 (Dahlstroem and Fuxe, 1964; Jacobs and Azmitia, 1992)), are variably

550 described in the literature. Alonso and colleagues divide B6 into dorsal and ventral sub-
551 compartments, referred to as r1DRd and r1DRv, respectively, where “r1” designates the
552 putative developmental domain of origin of *Pet1* neurons residing in this DR subregion
553 (i.e. originating from r1, as opposed to isthmus)(Alonso et al., 2013). r1DRv likely
554 corresponds to what others have described as the caudal portion of the “interfascicular”
555 DR (DRI), a medioventral band of DR cells flanked on either side by the medial
556 longitudinal fasciculi. 5-HT neurons of the caudal DRI merge with the more dorsal B6 DR
557 sub-nucleus roughly at the level of the DR where dorsolateral 5-HT neurons become
558 sparse (coronal sections 5 and 6 in **Figure 3**) (Hale and Lowry, 2011; Jacobs and
559 Azmitia, 1992). Depending on the plane and angle of sectioning these caudal DRI cells
560 also appear to merge with MR 5-HT neurons more ventrally, and it has been proposed
561 that caudal DRI cells may be more similar to MR 5-HT neurons developmentally,
562 morphologically, and hodologically than to DR 5-HT neurons (Commons, 2015, 2016;
563 Hale and Lowry, 2011; Jacobs and Azmitia, 1992). In the present study, our designation
564 of cDR is inclusive of r1DRd/r1DRv/caudal DRI/B6, as indicated in **Figure 4A**. Moreover,
565 we do not discount the possibility that this region as drawn partially overlaps with what
566 Alonso and colleagues would call the most dorsal portion of the caudal median raphe
567 (MnRc), as the boundary between the MnRc and r1DRv is poorly defined. Thus, the
568 territory between the cluster of *Met-Vglut3-Tph2-Pet1* neurons beneath the aqueduct in
569 the cDR and the MR is difficult to classify strictly based on cytoarchitecture,
570 underscoring the importance of alternative classification schemes, such as offered by
571 transcriptomics.

572 *Manual scRNA-seq of Pet1-Intersectionally Defined Neuron Populations*

573 Having mapped the spatial distributions of intersectionally labeled *Pet1* neuron
574 subgroups, next we wanted to explore the correspondence of molecular subtype identity
575 with DR subregions more comprehensively. To do this, we microdissected subdomains
576 of the DR in a subset of the intersectional mouse lines just described, dissociated and
577 sorted fluorescently labeled neurons, harvested mRNA from single cells, and prepared
578 scRNA-seq libraries (n = 70 single-cell libraries in total) using the SMART-Seq v4 kit,
579 followed by Illumina sequencing (**Figure 4A**). Specifically, we separately microdissected
580 and manually sorted *Sert::cre;Pet1::Flpe* intersectionally labeled neurons from the
581 dorsolateral DR (dl or dlDR, n = 10 cells), dorsomedial DR (dm or dmDR, n = 9 cells)
582 ventromedial DR (vm or vmDR, n = 8 cells), and caudal DR (cDR, n = 6 cells), as

583 schematized in **Figure 4A**. Additionally, we separately microdissected and manually
584 sorted *Npy2r::cre;Pet1::Flpe* intersectional neurons from the rostral (rDR, n = 9 cells)
585 versus caudal (n = 10 cells) DR, *P2ry1:: cre;Pet1::Flpe* intersectional neurons from the
586 cDR (n = 10 cells) , and *Crh::cre;Pet1::Flpe* intersectional neurons from the rostromedial
587 DR (n = 8 cells). We then used the fourteen *Pet1* neuron subtype identities derived from
588 our 10X scRNA-seq data as a reference to "query" the corresponding identities of our
589 manually sorted and transcriptomically profiled single cells (using the Seurat functions
590 FindTransferAnchors and TransferData as described in (Stuart et al., 2019)). A summary
591 of this analysis is shown in the dot plot in **Figure 4B**. We found that the majority of
592 *Sert::cre;Pet1::Flpe* dlDR neurons mapped to cluster two, with a smaller percentage of
593 single cells mapping to clusters one, three, and six. *Sert::cre;Pet1::Flpe* dmDR neurons
594 were split between clusters two and three, and to a lesser extent four, five, and nine.
595 *Sert::cre;Pet1::Flpe* vmDR neurons mostly corresponded to cluster ten, and were
596 additionally mapped to clusters one, four, seven, and thirteen (note, this may suggest
597 that some *Pet1* neurons expressing little or no *Sert* nor *Tph2* in the adult may yet
598 express the *Sert::cre* transgene). Finally, *Sert::cre;Pet1::Flpe* cDR neurons mapped
599 exclusively to clusters eight and seven (note, cluster twelve neurons do not appear to be
600 well marked by *Sert::cre;Pet1::Flpe;RC::FrePe* EGFP expression – see **Figure 3A5**
601 compared with **Figure 3E5** – perhaps reflecting the lower levels of *Sert* transcripts
602 detected in these neurons).

603 The majority of *Npy2r::cre;Pet1::Flpe* neurons in the rDR were found to correspond to
604 cluster six, with additional mapping to clusters five, seven, ten, and thirteen (consistent
605 with the expression profile of *Npy2r* transcripts in the 10X scRNA-seq data) whereas the
606 majority of *Npy2r:: cre;Pet1::Flpe* neurons from the cDR were found to correspond to
607 cluster seven, with a smaller percentage corresponding to clusters ten and fourteen.
608 *P2ry1::cre;Pet1::Flpe* cDR manually sorted and profiled neurons were mapped
609 exclusively to cluster twelve as expected. *Crh::cre;Pet1::Flpe* profiled neurons were split
610 across clusters in a manner consistent with sporadic *Crh* expression in our 10X scRNA-
611 seq data, however, we found more cluster three than cluster nine *Crh::cre;Pet1::Flpe*
612 neurons, perhaps reflecting that our sampling of this population was biased towards
613 rostromedial DR (or a potential discrepancy between endogenous *Crh* expression and
614 *Crh::cre* expression). Finally, we also included *Drd2::cre;Pet1::Flpe* intersectional
615 scRNA-seq data (n = 17 cells) associated with a previous study from our lab

616 (Niederkofler et al., 2016). *Drd2::cre;Pet1::Flpe* intersectional neurons show a largely
617 dorsolateral and dorsomedial bias within the DR. The majority of these neurons map to
618 clusters three and four, with a much smaller percentage mapping to clusters eight and
619 eleven.

620 Thus combining intersectional genetics, histological analyses, and precisely targeted
621 manual scRNA-seq we were able to infer the anatomical distributions of our fourteen
622 clusters to varying degrees of specificity. Clusters one through six appear to be rostrally
623 and dorsally biased, with cluster two showing a strong dorsolateral bias as well. Clusters
624 seven, eight, and twelve appear to be caudally and medially biased, with cluster twelve
625 showing a clear dorsal bias and clusters seven and eight showing more ventral bias
626 based on **Figure 3A5-6, C5-6** (though a nontrivial degree of intermixing of different
627 genetically defined *Pet1* neuron subpopulations in the dorsal cDR is apparent from these
628 images). *Pet1-Tph2*^{low} neurons (comprising cluster thirteen and to a lesser extent cluster
629 14 neurons) show a prominent enrichment in the dorsomedial and medial-rostral DR,
630 though they are also scattered throughout the DR (but very rarely found dorsolaterally).
631 The remaining clusters appear to be more ventromedially biased in the more rostral DR.
632 Expression patterns of cluster marker genes showing strong anatomical biases in our
633 manual scRNA-seq data are depicted in the dot plot in **Figure 4–figure supplement 1** in
634 comparison with our 10X scRNA-seq data.

635 These inferred anatomical distributions of molecularly distinct *Pet1* neuron populations
636 shed further light on the potential developmental significance of transcription factor
637 expression patterns described above. As noted, *Pax5*, a gene associated with isthmic
638 organizer activity during embryonic development (Funahashi et al., 1999; Ye et al.,
639 2001), shows a complementary expression pattern to *Nr2f2*, which encodes a
640 transcription factor that appears to be excluded from the isthmus, but is expressed in r1
641 and other rhombomeres during development, at least in zebrafish (Love and Prince,
642 2012). We further validated the anatomical expression profile of these genes, as well as
643 *Satb2* (expressed by cluster two through four), at the level of protein expression by
644 performing immunohistology in tissue sections prepared from *Vglut3::IRES-*
645 *cre;Pet1::Flpe;RC*::*FL-hM3Dq* mice (**Figure 4–figure supplement 2 A-E**). Consistent
646 with our anatomically-targeted, manual scRNA-seq data, PAX5 and SATB2 display a
647 rostrodorsal bias in predominately non-*Vglut3*-expressing DR *Pet1* neurons (**Figure 4–**
648 **figure supplement 2B-C,E**), whereas NR2F2 has a ventromedial and caudal

649 expression bias in predominately *Vglut3*-expressing DR *Pet1* neurons (**Figure 4–figure**
650 **supplement 2D,E**). Alonso and colleagues have proposed that cDR *Pet1* neurons are
651 derived from r1 progenitors, whereas more rostral *Pet1* neurons are derived from
652 isthmus (Alonso et al., 2013), however further fate-mapping experiments would be
653 helpful to clarify isthmic versus r1-derived *Pet1* neuron populations (Okaty et al., 2019).
654 Moreover, while rostral DR *Pet1* neurons may derive from isthmus and cDR *Pet1*
655 neurons may derive from r1, our scRNA-seq data nonetheless show substantial *Pet1*
656 neuron molecular heterogeneity within both DR domains, suggesting factors beyond
657 isthmus and r1-lineage driving molecular diversity.

658 **cDR *P2ry1::cre;Pet1::Flpe* neurons display unique hodological and**
659 **electrophysiological properties**

660 Having established correlations between DR *Pet1* neuron molecular expression profiles
661 and anatomical distribution of cell bodies, we next wanted to explore corresponding
662 differences in other cellular phenotypes. We chose to focus on cluster twelve *Met-*
663 *Vglut3-Tph2 Pet1* neurons, captured intersectionally by *P2ry1::IRES-cre;Pet1::Flpe,* as
664 they are the most distinct from other *Pet1* neurons molecularly. To determine if these
665 neurons are likewise unique from other DR *Pet1* neurons with respect to other features
666 we explored the hodological and electrophysiology properties of *P2ry1::cre;Pet1::Flpe*
667 neurons using the intersectional expression of TdTomato (*RC::Ai65*). The anatomical
668 location of cell somata labeled in *P2ry1::IRES-cre;Pet1::Flpe;RC::Ai65* animals was
669 similar to that found in the previously characterized *P2ry1::IRES-*
670 *cre;Pet1::Flpe;RC::FrePe* mice, with a dense population of neurons directly under the
671 aqueduct in the cDR. In addition, there were slightly higher numbers of intersectionally
672 labeled cells in the rostral part of the dorsal raphe as well as scattered cells in the
673 median raphe, consistent with the sporadic expression of *P2ry1* revealed by the present
674 RNA-seq data and the scRNA-seq data of *Pet1* neurons from the MR (Okaty et al.,
675 2015; Ren et al., 2019). Strikingly, most fibers from *P2ry1::cre;Pet1::Flpe;RC::Ai65*
676 neurons were supra-ependymal and were found throughout the third, lateral, and fourth
677 ventricles, a property previously attributed to 5-HT neurons within the cDR (Kast et al.,
678 2017; Mikkelsen et al., 1997; Tong et al., 2014). Sparser fibers were found in regions
679 such as the lateral hypothalamus, medial and lateral septum, hippocampus, olfactory
680 bulb, lateral parabrachial nucleus, and the amygdala. To gain a better perspective of the
681 extent of *P2ry1::cre; Pet1::Flpe;RC::Ai65* fibers in the lateral ventricle we stained for

682 *P2ry1::cre;Pet1::Flpe;RC::Ai65* fibers on a flat mount of the lateral wall as previously
683 described (Mirzadeh 2010). *P2ry1::cre; Pet1::Flpe;RC::Ai65* fibers were found on all
684 aspects of the wall except for the adhesion area, including regions that contain
685 proliferating cells and migrating neuroblasts from the subventricular zone (Mirzadeh et
686 al., 2010)(**Figure 5**). Further, *P2ry1::cre;Pet1::Flpe;RC::Ai65* fibers were closely
687 apposed to proliferating cells (Ki67+) and migrating neuroblasts (doublecortin, DCX+)
688 within the subventricular zone (SVZ) and within the rostral migratory stream (RMS)
689 (**Figure 5**). The proximity of *P2ry1::cre;Pet1::Flpe;RC::Ai65* fibers to adult neural stem
690 cells suggests that they may constitute a serotonergic population of neurons that
691 regulate SVZ proliferation, a process known to be regulated by 5-HT levels and that has
692 previously been associated with the cDR (Aghajanian and Gallager, 1975; Banasr et al.,
693 2004; Brezun and Daszuta, 1999; Hitoshi et al., 2007; Kast et al., 2017; Lorez and
694 Richards, 1982; Mirzadeh et al., 2010; Negoias et al., 2010; Siopi et al., 2016; Soumier
695 et al., 2010; Tong et al., 2014).
696 To determine if supra-ependymal projections are unique to *Pet1* neurons in the
697 caudal dorsal raphe, we injected a retrograde AAV virus leading to expression of Cre
698 under the synapsin reporter (pENN.AAV.hSyn.Cre.WPRE.hGH) unilaterally into the
699 lateral ventricle of double transgenic *Pet1::Flpe;FrePe* or *Pet1::Flpe;Ai65 mice*, where
700 expression of both Cre and Flpe leads to cell labeling by EGFP or TdTomato
701 respectively (Figure 5 – figure supplement 1 A). The predominant labeled population in
702 both genotypes was in the caudal dorsal raphe, just under the aqueduct, suggesting that
703 *P2ry1::cre;Pet1::Flpe* neurons constitute the major supraependymal projecting group of
704 Pet1 neurons (Figure 5 – figure supplement 1 B,C). However, in agreement with other
705 studies that have included retrograde labeling via the lateral ventricle, some cell bodies
706 were also found in the median raphe (Kast et al., 2017, Tong et al., 2014). Thus, supra-
707 ependymal projections, while predominantly originating from the caudal dorsal raphe,
708 are not entirely unique to this region.

709 We next characterized electrophysiological properties of *P2ry1::IRES-cre;*
710 *Pet1::Flpe;RC::Ai65* neurons in comparison with other more broadly defined *Pet1*
711 neuron subpopulations using whole-cell patch clamp in acute slice preparations. As
712 comparison groups we chose: (1) "subtractive" *P2ry1::IRES-cre; Pet1::Flpe;RC::FL-*
713 *hM3Dq* neurons in the cDR (i.e. cDR neurons with a history of *Pet1::Flpe* expression but
714 not *P2ry1::IRES-cre* expression; we chose to use *RC::FL-hM3Dq* as opposed to

715 *RC::Ai65* or *RC::FrePe* because the subtractive population is identifiable in acute brain
716 slices by EGFP fluorescence without the need for secondary staining), and (2)
717 *Gad2::IRES-cre;Pet1::Flpe;RC::Ai65* neurons from the more rostral and mostly dorsal
718 DR (**Figure 6**). Recording from *P2ry1::IRES-cre;Pet1::Flpe;RC*::*FL-hM3Dq* subtractive
719 cDR neurons allowed us to assess the degree to which electrophysiology may differ
720 within a given DR subdomain depending on molecularly-defined neuron subtype,
721 whereas *Gad2::IRES-cre;Pet1::Flpe;RC::Ai65* neuron recordings provided a comparison
722 group that is both anatomically and molecularly distinct. As demonstrated in the
723 frequency-current (F-I) curves in **Figure 6A,** we found that *P2ry1::IRES-*
724 *cre;Pet1::Flpe;RC::Ai65* neurons have dramatically lower excitability than the two
725 comparison populations, requiring substantially more injected current to reach action
726 potential threshold, and showing a roughly three-fold lower maximum firing rate. Even
727 within the regime of current injection that *P2ry1::IRES-cre;Pet1::Flpe;RC::Ai65* neurons
728 are excitable, we found that they displayed very different spiking characteristics from
729 other *Pet1* neuron groups (**Figure 6B, C**), specifically showing a longer latency to first
730 action potential (AP, **Figure 6B, 3**). Altogether, we observed four distinct firing types
731 exemplified by the voltage traces displayed in **Figure 6B**: short-latency to first AP
732 (regular spiking/non-adapting) (**Figure 6B, 1**), mid-latency to first AP (**Figure 6B, 2**),
733 long-latency to first AP (**Figure 6B, 3**), and short-latency to first AP with spike frequency
734 adaptation (**Figure 6B, 4**). The heatmap in **Figure 6C** shows the percentage of single-
735 neuron recordings from each genotype that correspond to a given firing type. **Figure 6-**
736 **figure supplement 1** displays differences in measured electrophysiological properties
737 when cells are grouped by firing type, as opposed to genotype. All *P2ry1::IRES-*
738 *cre;Pet1::Flpe;RC::Ai65* neurons recorded (twelve neurons from three animals) showed
739 long latency to first AP, whereas only one out of nine subtractive neurons in the
740 *P2ry1::IRES-cre;Pet1::Flpe;RC*::*FL-hM3Dq* cDR (from three animals) showed this
741 phenotype and none of the *Gad2::IRES-cre;Pet1::Flpe;RC::Ai65* neurons (twelve
742 neurons from two animals). These latter two groups of neurons showed greater
743 heterogeneity with respect to firing characteristics, as might be expected given that
744 labeled cells from both genotypes comprise multiple molecular subtypes identified by our
745 scRNA-seq experiments. While the full extent of electrophysiological heterogeneity of
746 these populations is likely under-sampled by the present dataset, the uniqueness of
747 *P2ry1::IRES-cre;Pet1::Flpe;RC::Ai65* neurons nonetheless stands out.

748 **Comparison to other DR scRNA-seq datasets**

749 Recent scRNA-seq studies of mouse DR cell types have been published (Huang et al.,
750 2019; Ren et al., 2019), reporting using either the InDrops platform to profile dissociated
751 DR neurons (Huang et al., 2019) or fluorescence-activated cell sorting to purify
752 dissociated Cre-dependent tdTomato-expressing *Sert::cre* neurons from mouse DR and
753 MR, followed by SMART-Seq v2 library preparation and sequencing (Ren et al., 2019).
754 Huang and colleagues identified six distinct *Pet1*-expressing DR neuron subtypes – five
755 serotonergic and one glutamatergic – while Ren and colleagues identified seven *Pet1*-
756 expressing serotonergic DR neuron subtypes (note they did not identify a glutamatergic
757 *Tph2*^{low} group, presumably because these neurons do not typically express *Sert::cre*). To
758 directly compare our subtype classifications, we used the fourteen *Pet1* neuron subtype
759 identities derived from our 10X scRNA-seq data as a reference to query the
760 corresponding identities of the Huang and Ren datasets (using the Seurat functions
761 FindTransferAnchors and TransferData, as described above for comparison with our
762 manual scRNA-seq data). The results of this analysis are shown in the dot plot in **Figure**
763 **7**. Some *Pet1* neuron subgroup classifications were highly consistent across studies. For
764 example, one hundred percent of single neurons making up the Huang 5-HT V and Ren
765 cDR subgroups map to our cluster twelve *Pet1* neuron subgroup (*Met-Vglut3-Tph2-Pet1*
766 neurons, corresponding to neurons intersectionally captured by *P2ry1::cre;Pet1::Flpe*
767 expression in the cDR shown in **Figure 3E**). Likewise, there is high correspondence
768 between Huang 5-HT I, Ren DR 1, and our cluster-two *Pet1*-neuron subgroup
769 (dorsolateral DR *Gad2-Trh-Tph2-Pet1* neurons). Huang 5-HT II and Ren 2 subgroups
770 are largely split between our cluster two and cluster three subgroups, with a smaller
771 portion of each mapping to our cluster four subgroup (which also corresponds to a small
772 subset of Huang 5-HT I and Ren DR 1 neurons). Huang 5-HT III and Ren DR 3
773 correspond to our cluster five and six subgroups, with a larger percentage of Huang 5-
774 HT III neurons mapping to cluster five and a larger percentage of Ren DR 3 neurons
775 mapping to cluster six.

776 In other cases, there is better correspondence between our identified *Pet1* neuron
777 subgroups and one or the other study, likely due in part to technological differences
778 between studies. For example, Huang Glu V corresponds well with our cluster thirteen
779 *Pet1* neuron subgroup (*Vglut3-Tph2*^{low}*-Pet1* neurons) but very few neurons profiled in
780 the Ren study map to cluster thirteen. As mentioned above, the absence of a prominent

781 glutamatergic *Tph2*^{low} group of neurons in the Ren study likely stems from the fact that
782 the low level of *Sert* transcription in these neurons does not reliably drive *Sert::cre*
783 transgene expression and thus reporter expression for their cell sorting. However, the
784 fact that a small number of *Sert::cre* expressing neurons from the Ren study do map to
785 our cluster thirteen subgroup indicates that there may be exceptions (moreover, these
786 cells may more specifically map to cluster thirteen neurons at the higher end of the
787 distribution of *Sert* and *Tph2* transcript levels **Figure 1–figure supplement 3**).

788 On the other hand, Ren DR 6 corresponds well with our cluster one subgroup (*Npas1/3-*
789 *Tph2-Pet1* neurons) and Ren DR 4 corresponds well with our cluster nine subgroup
790 (*Maf-Nos1-Tph2-Pet1* neurons), but there is no such one-to-one correspondence
791 between these groups and the neuron groups identified in the Huang study. Rather,
792 cluster one and cluster nine neurons get "pulled" from other groups identified by Huang.
793 This likely reflects the different sensitivities of the various approaches. Specifically, our
794 study and the Ren study achieved more than three-fold higher gene detection per single
795 cell library on average than the Huang study, thus allowing for finer-scale molecular
796 subgroup classification. However our higher single-cell sampling resolution – we profiled
797 2,350 DR *Pet1* neurons, whereas Huang and Ren profiled roughly seven hundred and
798 600 DR *Pet1* neurons, respectively – likely allowed us to resolve more subgroups.
799 Huang 5-HT IV and Ren DR 5 show the greatest degree of dispersion into different
800 clusters identified in our study. Ren DR 5 is split predominately between clusters seven,
801 ten, and fourteen, while Huang 5-HT IV is split into clusters ten and fourteen, as well as
802 across several other clusters. Lastly, we also found that Ren MR 1 (identified as being a
803 median raphe 5-HT neuron subtype in that study) shows similarity to our cluster eight
804 subgroup, which we have mapped to the cDR based on histology and our manual
805 scRNA-seq data. As described above, the boundary between the cDR and the MR,
806 specifically the portion of the MR attributed to r1-derived neurons (Alonso et al., 2013;
807 Okaty et al., 2015), is poorly defined, thus Ren MR 1 and our cluster eight neurons may
808 indeed partially overlap anatomically. Notably, some Huang 5-HT IV neurons
809 (microdissected from what was considered the DR in that study) also map to our cluster
810 eight subgroup.

811 Importantly, our higher number of identified clusters does not appear to stem from
812 analytic differences between studies *per se*, given that we identified more clusters using
813 a lower resolution parameter in our clustering analysis than the other two studies.

814 Huang, et al. reported using a Seurat FindCluster resolution of 2.0, Ren, et al. used a
815 resolution of 1.0, whereas the highest resolution we used was 0.9. In order to explicitly
816 investigate how specific aspects of our experimental design may have led to
817 identification of more DR *Pet1* neuron subgroups than the other two studies, we
818 modeled how the number of cells sampled and the number of UMIs identified per cell
819 influence the number of identified clusters in our dataset. Specifically, we randomly sub-
820 sampled variable numbers of cells (twenty times per iteration) and re-clustered the
821 resulting data in the same manner described for the full dataset (using a Seurat
822 FindClusters resolution of 0.9), varying the number of sampled cells from 200 to 2300
823 (**Figure 7 – figure supplement 1A**). As expected, we found that increasing the number
824 of cells increased the number of clusters. Identification of fourteen clusters did not occur
825 until at least 1,700 cells were included in the analysis, and this number of clusters began
826 to stabilize as 2,100 or more cells were included. Similarly, we randomly sub-sampled
827 UMIs, varying the maximum number of UMIs per cell from 500 to 100,000, and repeated
828 our clustering analysis twenty times per sub-sampled max UMI (**Figure 7 – figure**
829 **supplement 1B**). In this case we found a much steeper relationship between max UMIs
830 and number of clusters identified, with fourteen clusters being identified with as few as
831 4500 max UMIs per cell, and completely stabilizing at roughly 60,000 max UMIs. With
832 respect to our ability to resolve fine-scale DR *Pet1* neuron subgroup structure, these
833 results indicate that while both variables are important, the number of cells sampled was
834 more limiting than the number of UMIs in our dataset; i.e. we could have uncovered a
835 similar degree of overall cellular diversity (fourteen subtypes) with less “complex”
836 libraries (e.g. from more shallow sequencing), however we needed nearly 90% of the
837 cells we sampled to consistently uncover fourteen molecular subgroups.

838 The results of these analyses shed light on the most likely reasons why we were able to
839 achieve more fine-grained classification of DR *Pet1* neuron subtypes than the other two
840 studies. For example, the Ren study had a similar degree of library complexity to ours
841 (slightly higher, in fact), however as noted above they profiled fewer cells – 567 to our
842 2350 cells (~2200 excluding *Tph2-low* cells). When we sub-sample our data to a similar
843 number of cells, we find between six and nine clusters, and similarly, Ren, et al. reported
844 seven DR 5-HT neuron clusters. When we simultaneously sub-sample both the number
845 of cells profiled and the maximum number of UMIs detected per single cell to levels
846 similar to the Huang, et al. study (750 cells and 2500 max UMIs, **Figure 7 – figure**

847 **supplement 1C**), we uncover between four and seven subgroup clusters – Huang, et al.
848 found six. Thus, all other methodological sources of variation between studies aside,
849 these two parameters plausibly explain differences in the degree of diversity uncovered
850 across studies.

851 **Discussion**

852 The dorsal raphe nucleus is likely one of the most extensively connected hubs in the
853 mammalian brain. Efferent DR fibers, predominantly serotonergic (but also glutamatergic
854 and GABAergic), collectively innervate much of the forebrain and midbrain, as well as
855 some hindbrain nuclei (Azmitia and Segal, 1978; Bang and Commons, 2012; Bang et al.,
856 2012; Beaudet and Descarries, 1976; Fernandez et al., 2016; Gagnon and Parent, 2014;
857 Hale and Lowry, 2011; Kast et al., 2017; Kosofsky and Molliver, 1987; Lidov et al., 1980;
858 Lidov and Molliver, 1982; Maddaloni et al., 2017; McDevitt et al., 2014; Molliver, 1987;
859 Muzerelle et al., 2016; O'Hearn and Molliver, 1984; Prouty et al., 2017; Ren et al., 2018;
860 Steinbusch, 1981; Steinbusch et al., 1980; Vasudeva et al., 2011; Vertes, 1991; Vertes
861 and Kocsis, 1994), and DR afferents have been identified from as many as eighty
862 distinct anatomical brain regions, including other brainstem raphe nuclei (Celada et al.,
863 2001; Commons, 2015; Goncalves et al., 2009; Levine and Jacobs, 1992; Mosko et al.,
864 1977; Ogawa et al., 2014; Peyron et al., 1998; Peyron et al., 2018; Pollak Dorocic et al.,
865 2014; Weissbourd et al., 2014). As such, the DR is hodologically poised to send and
866 receive signals related to a wide range of sensory, motor, affective, and cognitive
867 processes. Indeed, DR neuropathology is associated with several human disorders (or
868 disease models thereof) with broad symptomatology, such as major depressive disorder,
869 autism, and Alzheimer's disease (Chen et al., 2000; Dengler-Crish et al., 2017; Doan et
870 al., 2019; Ellegood et al., 2015; Guo and Commons, 2017; Ji et al., 2020; Luo et al.,
871 2017; Michelsen et al., 2008; Miyazaki et al., 2005; Simic et al., 2017; Vakalopoulos,
872 2017; Wang et al., 2018; Zweig et al., 1988). Outside of DR-specialist research, the DR
873 has often been viewed by the wider neuroscience community as a "black box" source of
874 a single neurochemical, namely 5-HT. Accordingly, development of therapeutics for
875 associated disorders has largely focused on modulating overall serotonergic tone.
876 However, DR-focused research over several decades has revealed layers of functional
877 complexity and compositional heterogeneity warranting a more nuanced view (reviewed
878 in (Abrams et al., 2004; Andrade and Haj-Dahmane, 2013; Gaspar and Lillesaar, 2012;
879 Hale and Lowry, 2011; Michelsen et al., 2007; Okaty et al., 2019; Vasudeva et al.,

880 2011)). While these studies have reached into the black box of the DR and described a
881 variety of features at different levels of observation, integration across levels to arrive at
882 principles of DR organization has proved challenging. Elucidating how molecular,
883 neurochemical, anatomical, hodological, electrophysiological, and functional descriptions
884 of the DR overlap is essential to understanding the structure-function relationship of the
885 DR and other raphe nuclei (Brust et al., 2014; Fernandez et al., 2016; Huang et al.,
886 2019; Kast et al., 2017; Niederkofler et al., 2016; Okaty et al., 2015; Prouty et al., 2017;
887 Ren et al., 2018; Ren et al., 2019), and will likely facilitate improved therapies for human
888 disorders. Here we have focused on one broadly defined subgroup of DR cells –
889 neurons that express the gene *Pet1/Fev* – and applied scRNA-seq, iterative
890 intersectional genetics, histology, and slice electrophysiology to provide a transcriptomic
891 and anatomic atlas of mouse DR *Pet1* neurons with examples of links between
892 molecular, neurochemical, anatomical, hodological, and electrophysiological levels of
893 description. We identify as many as fourteen distinct molecularly defined subtypes of
894 *Pet1* neurons that show biased cell body distributions in DR subregions. We further
895 characterize projections and electrophysiology of the most molecularly unique DR *Pet1*
896 neuron subtype – *Met-Vglut3-Tph2-Pet1* cDR neurons (cluster twelve), genetically
897 accessed by intersectional *P2ry1::cre;Pet1::Flpe* expression. The present study
898 complements other recent characterizations of DR cell types (Huang et al., 2019; Ren et
899 al., 2019), increasing the sampling resolution of *Pet1* neurons in particular through our
900 experimental approach to achieve fine-scale identification of *Pet1* neuron subtypes.

901 ***Molecular and anatomic organization of Pet1 neuron subtypes***

902 Our data and analysis highlight the hierarchical organization of DR *Pet1* neurons
903 molecularly and anatomically, allowing for identification of features that organize *Pet1*
904 neurons at different levels of granularity (**Figure 8, Figure 8 – figure supplement 1**).
905 Neurochemistry has long served as a principal phenotypic axis for classifying neurons,
906 and concordantly we found that distributions of transcripts associated with distinct
907 neurotransmitters correspond with broad subgroup divisions. The majority of *Pet1*
908 neurons (clusters one through twelve) express high levels of *Tph2* mRNA, encoding
909 tryptophan hydroxylase two, the rate-limiting biosynthetic enzyme for 5-HT, as well as
910 several other genes indicative of a serotonergic phenotype, such as *Slc6a4* (*Sert*),
911 *Slc18a2* (*Vmat2*), and *Maob*. However, we also identified two subgroups of *Pet1*
912 neurons with 5-HT marker gene profiles that differ from the majority (clusters thirteen

913 and fourteen). One subgroup (cluster thirteen) expresses very low transcript levels of 5-
914 HT neuron marker genes, is mostly negative for TPH2 immunolabeling, and shows a
915 biased cell body distribution in the rostromedial DR, as well as distributing sporadically
916 throughout. The other subgroup (cluster fourteen) exhibits a much broader distribution of
917 transcript levels for 5-HT marker genes than other groups. The functional significance of
918 this variable expression can only be hypothesized at present; we speculate that it may
919 reflect a capacity for neurotransmitter plasticity – i.e. experience-dependent induction or
920 up-regulation of 5-HT phenotype, as hinted at by a recent study (Prakash et al., 2019). If
921 this is the case, cluster fourteen neurons may be partially in transition, for example, from
922 a predominately glutamatergic phenotype to a 5-HT phenotype or to a glutamate-5-HT
923 co-transmitter phenotype. Both cluster thirteen and fourteen *Pet1* neuron subgroups
924 express *Slc17a8* (*Vglut3*) transcripts, suggestive of a capacity for synaptic glutamate
925 packaging and release, and show shared enrichment for several transcripts, including
926 *Ldb2*, encoding the transcription factor LIM domain binding 2, and *Cnr1*, encoding
927 cannabinoid receptor 1. Cluster fourteen is also uniquely distinguished by enrichment for
928 *Gpr101* transcripts, encoding an orphan G protein-coupled receptor.

929 Among *Pet1* neurons expressing high levels of *Tph2* and other 5-HT gene markers,
930 expression of genes related to GABA synthesis (*Gad1* and *Gad2*) or glutamatergic
931 synaptic vesicle packaging (*Vglut3*) correlate with major molecular and anatomical
932 subdivisions (evident in the dendrogram in **Figure 1B**, the UMAP plot in **Figure 1C**, and
933 the histological image series in **Figure 3 B1-6 and Figure 3 – figure supplement 1D-**
934 **J**). We found that the cell bodies of non-*Vglut3*, largely *Gad2*-expressing *Pet1* neurons
935 are preferentially distributed in the dorsal and lateral subregions of the rostral DR, and
936 become exclusively lateral and ultimately absent at more caudal extents of the DR.
937 Conversely, *Vglut3-Tph2-Pet1* neuron bodies show a ventromedial bias rostrally and
938 predominate the entire cDR. *Gad2-Tph2-Pet1* neurons and *Vglut3-Tph2-Pet1* neurons
939 show differential enrichment of hundreds of transcripts, including *Pax5* and *Nr2f2*. Both
940 genes encode transcription factors, the expression of which we examined through
941 immunohistology and found a similar distribution of cell body staining as revealed by
942 intersectional genetic labeling of *Vglut3::cre;Pet1::Flpe* neurons – *Pax5* expression
943 overlaps predominately with the non-*Vglut3*-expressing population, whereas *Nr2f2*
944 overlaps with the *Vglut3*-expressing population (**Figure 4 – figure supplement 2**). We
945 also found one *Pet1* neuron subgroup (cluster six) that expresses *Gad1*, *Gad2*, and

946 “intermediate” levels of *Vglut3* transcripts (relative to other *Vglut3*+ clusters). These
947 neurons correspond with the rostral population of neurons labeled by intersectional
948 *Npy2r::cre;Pet1::Flpe* expression (**Figure 3C**), which we characterized by manual
949 scRNA-seq (**Figure 4**).

950 Altogether we identified five *Pet1* neuron subgroups that express *Gad1* or *Gad2*
951 transcripts (clusters two through six), and found *Gad2* to be expressed more consistently
952 and at higher levels than *Gad1* (with the exception of cluster six). *Gad1* and *Gad2*
953 encode two distinct isoforms of glutamate decarboxylase, referred to as GAD67 and
954 GAD65, respectively. In many neuron types, these proteins are often co-expressed, but
955 localize to different subcellular compartments and differ in their interaction with the co-
956 factor pyridoxol phosphate (Chen et al., 2003; Erlander et al., 1991; Soghomonian and
957 Martin, 1998). GAD65 (encoded by *Gad2*) is typically found in axon terminals where it is
958 thought to play a role in GABA synthesis specifically for synaptic vesicular release,
959 whereas GAD67 is typically localized to the soma and may be more involved with non-
960 vesicular GABA release. While we did not reliably detect transcripts for the vesicular
961 GABA transporter (*Slc32a1*), we did detect expression of transcripts encoding VMAT2
962 which has been shown to package GABA into synaptic vesicles in dopaminergic
963 neurons, allowing for monoaminergic-GABAergic co-transmission (Tritsch et al., 2012).
964 Thus it is plausible that *Gad2-Tph2-Pet1* neurons may likewise co-release GABA,
965 though it has yet to be reported in the literature.

966 Beyond classic neurotransmitters, we also found enrichment of various peptide hormone
967 transmitters in different *Gad2-Tph2-Pet1* neuron subgroups. Cluster two shows
968 enrichment for thyrotropin-releasing hormone transcripts (*Trh*), and clusters five and six
969 show enrichment for prodynorphin (*Pdyn*) (as does cluster fourteen). As can be seen in
970 the dendrogram in **Figure 1B** and UMAP plot in **Figure 1C**, there appears to be a major
971 division between *Gad2-Tph2-Pet1* clusters two through four and clusters five and six,
972 with clusters five and six also sharing many molecular similarities with *Vglut3-Tph2-Pet1*
973 subgroups. This may in part reflect differential expression of transcription factors that
974 regulate divergent gene “modules”. While all *Gad2-Tph2-Pet1* neurons express *Pax5*,
975 clusters two through four also express *Sox14* and *Satb2*. Cluster six, on the other hand,
976 shows enrichment for several transcription factor genes that are also enriched (or trend
977 towards enrichment) in clusters thirteen and fourteen, such as *Pou3f2*, *Bcl11a*, and *Id2*.
978 These molecularly distinct *Gad2-Tph2-Pet1* subgroups also show differences in

979 anatomy. Based on manual scRNA-seq of sub-anatomically targeted *Pet1* neurons, we
980 found that cluster two *Gad2-Trh-Tph2-Pet1* neuron cell bodies are found predominately
981 in the dorsolateral DR, as well as the dorsomedial DR, whereas clusters three, four, and
982 five appear to be more dorsomedially biased, consistent with recent reports (Huang et
983 al., 2019; Ren et al., 2019). Cluster six neurons, as captured by *Npy2r::cre;Pet1::Flpe*
984 expression, show a more diffuse distribution in the rostral DR, illustrating that not all *Pet1*
985 neuron subtypes, as defined transcriptomically, correspond with clear-cut anatomical
986 patterns. Indeed, while there are major differences between predominately dorsal versus
987 ventral or rostral versus caudal DR *Pet1* neuron subtypes, different subtypes
988 nonetheless intermix within these domains, emphasizing the importance of molecular-
989 genetic targeting of *Pet1* neuron subtypes to gain specificity for functional
990 characterization (a point also made by (Huang et al., 2019) and (Okaty et al., 2019)).

991 *Vglut3-Tph2-Pet1* neuron subgroups, as noted above, are found more ventrally than
992 *Gad2-Tph2-Pet1* neurons in the rostral DR, and are the dominant neurotransmitter
993 phenotype in the caudal DR (as inferred by transcript expression and VGLUT3 and
994 TPH2 immunostaining). We found two *Vglut3-Tph2-Pet1* neuron subtypes with cell
995 bodies biased towards the rostral DR (clusters nine and ten) and three subtypes
996 (clusters seven, eight, and twelve) biased towards the more caudal DR (as delineated in
997 **Figure 4**, and see the discussion of varying nomenclature around the cDR in the
998 **Results** section *Histology of Pet1-Intersectionally Defined Neuron Populations* above).
999 Cluster twelve *Pet1* neurons, also marked by expression of the gene *Met*, we found to
1000 be the most different from all other *Pet1* neurons, both in terms of the number of
1001 differentially expressed genes and the magnitudes of enrichment/depletion compared to
1002 other *Pet1* neuron subtypes (as also observed by (Huang et al., 2019; Ren et al., 2019)).
1003 We show by histology of genetically marked neurons (intersectional
1004 *P2ry1::cre;Pet1::Flpe* expression) that the cell bodies of these *Met-Vglut3-Tph2-Pet1*
1005 neurons are clustered beneath the aqueduct in the caudal DR (**Figure 3E**) and send
1006 extensive axonal projections throughout the ventricles (**Figure 5**). Based on retrograde
1007 tracing experiments (Kast et al., 2017; Tong et al., 2014), it is likely that these neurons
1008 constitute the major source of 5-HT innervation to the ventricles. Furthermore, our
1009 demonstration that *P2ry1::cre;Pet1::Flpe* fibers are closely apposed with proliferating
1010 and migrating cells in the SVZ and rostral migratory stream (**Figure 5**), supports a
1011 proposed role for these neurons in regulating adult neural stem cell proliferation in the

1012 SVZ (Tong et al., 2014). Cluster twelve neuron transcript enrichment for several GPCRs
1013 implicated in modulation of adult neurogenesis, such as *P2ry1* (Lin et al., 2007), *Gipr*
1014 (found to be enriched in our *P2ry1::cre;Pet1::Flpe* manual scRNA-seq data) (Nyberg et
1015 al., 2005), *S1pr3* (Alfonso et al., 2015; Ye et al., 2016), and *Oprm1* (Harburg et al., 2007)
1016 lends further support to this hypothesis. Now, with intersectional access to this
1017 population of cDR 5-HT neurons provided by *P2ry1::IRES-cre* with *Pet1::Flpe,* the
1018 function of *Met-Vglut3-Tph2-Pet1* cDR neurons in regulating SVZ proliferation can be
1019 tested directly in a cell type-specific manner using dual Cre- and Flpe- responsive
1020 chemo- or optogenetic approaches (Brust et al., 2014; Hennessy et al., 2017; Kim et al.,
1021 2009; Madisen et al., 2015; Niederkofler et al., 2016; Okaty et al., 2015; Ray et al., 2011;
1022 Sciolino et al., 2016; Teissier et al., 2015).

1023 **DR *Pet1* neuron subtypes have distinct electrophysiological properties**

1024 To further characterize correspondence of molecular identities with other cell
1025 phenotypes we performed whole-cell electrophysiological recordings in acute slices
1026 prepared from mice in which different *Pet1* neuron subsets were genetically labeled. We
1027 found that 5-HT neurons with different molecular identities also exhibit distinct
1028 electrophysiological properties likely to impact their circuit function. While we did not
1029 comprehensively sample all molecularly defined subtypes, our survey of cDR *Pet1*
1030 neurons and rostral dorsal raphe *Gad2::cre;Pet1::Flpe* neurons provides evidence for at
1031 least four distinct electrophysiological types based on four key properties: (1) rheobase
1032 (also known as current threshold), which reflects a neuron's sensitivity to input, (2) delay
1033 to first spike, which reflects the degree to which a neuron is able to activate phasically in
1034 response to input, (3) spike-frequency adaptation, which reflects the degree to which a
1035 neuron is able to continuously signal ongoing input, and (4) maximum firing rate, which
1036 determines the dynamic range of neuron responsiveness to graded inputs. As with
1037 molecular differences, cluster twelve *Met-Vglut3-Tph2-Pet1* cDR neurons
1038 (*P2ry1::cre;Pet1::Flpe* intersectional expression) showed profound differences from
1039 other subtypes, including other cDR *Pet1* neurons. *P2ry1::cre;Pet1::Flpe* neurons
1040 consistently displayed a long latency to first action potential, required substantially more
1041 input to reach action potential threshold, and had a lower maximum firing rate (**Figure 6**
1042 **and Figure 6 – figure supplement 1**). These differences, together with differential
1043 transcript expression of several GPCRs, suggest that *Met-Vglut3-Tph2-Pet1* cDR
1044 neurons respond in a different way and to very different stimuli than other DR *Pet1*

1045 neuron types. For example, low excitability and long-latency to spike suggest that these
1046 neurons may only be recruited by very strong stimuli at relatively slower timescales than
1047 other *Pet1* neurons (to the extent that properties recorded in slice reflect *in vivo*
1048 properties). Notably, 5-HT neurons with this electrophysiological profile have not yet
1049 been reported in the literature. However, the two firing types that we have defined as
1050 "Short-Latency to First AP; Non-Adapting" and "Mid-Latency to First AP" (**Figure 6B, 1**
1051 **and 2**) correspond well to those described by (Fernandez et al., 2016) in groups of *Pet1*-
1052 EGFP serotonergic neurons projecting to the mPFC and the BLA, respectively.
1053 Differential expression of ion channels and receptors identified here suggest molecular
1054 substrates of these different electrophysiological properties.

1055 **Technical aspects of our study allow for high-resolution transcriptome**
1056 **characterization of *Pet1* neurons**

1057 Due to the high-dimensional "richness" of transcriptomic data, together with the capacity
1058 to propose explanations of cellular phenotypes in terms of molecular mechanisms –
1059 RNA-seq dissection of neural circuits has gained traction as a way to define and
1060 enumerate cell types in the brain (and other tissues). Single-cell RNA-sequencing, in
1061 particular, has become an indispensable approach, with different methods achieving
1062 different resolution of underlying cellular diversity (Bakken et al., 2018; Campbell et al.,
1063 2017; Hodge et al., 2019; Huang et al., 2019; Lovatt et al., 2014; Macosko et al., 2015;
1064 Okaty et al., 2015; Poulin et al., 2016; Ren et al., 2019; Rosenberg et al., 2018;
1065 Saunders et al., 2018; Spaethling et al., 2014; Tasic, 2018; Tasic et al., 2016; Tasic et
1066 al., 2018; Usoskin et al., 2015; Zeisel et al., 2018; Zeisel et al., 2015). Droplet-based
1067 scRNA-seq approaches (without cell-type-specific purification) allow for unbiased
1068 classification of major cell types residing in a particular microdissected tissue region of
1069 interest, however lower abundance cell types, such as DR *Pet1* neurons profiled in the
1070 present study, are often insufficiently sampled to achieve high resolution of subtype
1071 molecular diversity. Moreover, different reaction chemistries employed in different
1072 droplet-based scRNA-seq approaches can lead to different gene detection sensitivity.
1073 Low cellular abundance compounded with low gene detection can greatly limit the power
1074 of a study to reveal fine-scale variation in molecular phenotypes that may be important
1075 for identifying neuronal subtypes and subtype "states" (e.g. adaptive or pathological
1076 transcriptional variation). Where cell type-specific markers are available, cell sorting prior
1077 to scRNA-seq library preparation can greatly enhance the resolution of cellular diversity

1078 for less abundant cell classes. While manual sorting approaches combined with RNA-
1079 seq library preparation optimized for low amounts of input RNA achieve high single-cell
1080 gene detection and allow for sampling genetically and anatomically-defined neuron
1081 populations (Niederkofler et al., 2016; Okaty et al., 2015), they are often limited in the
1082 number of cells profiled, and therefore may lack sufficient throughput to fully characterize
1083 subtype diversity. On the other hand, automated sorting approaches achieve greater
1084 throughput but are less well suited to collecting low abundance cell types, such as
1085 defined by fine-scale anatomy or highly restricted marker gene expression. Our
1086 particular experimental approach to characterizing DR *Pet1*-lineage neuron diversity in
1087 the present study was informed by all of the above concerns. By combining
1088 intersectional genetic labeling of DR *Pet1* neurons with both high-throughput
1089 (microfluidic On-chip Sort) and targeted low-throughput (manual) sorting approaches,
1090 followed by high-sensitivity RNA-seq library preparation protocols (10X Genomics
1091 Chromium Single Cell 3' v3 and SMART-Seq v4 kits, respectively) we leveraged the
1092 strengths of multiple approaches to achieve high-resolution transcriptomic profiling of DR
1093 *Pet1* neurons.

1094 ***Resource value of DR Pet1 neuron scRNA-seq data***

1095 While we have highlighted many salient experimental findings in the present report, the
1096 data no doubt have more to reveal, and we thus offer this dataset as a resource to be
1097 mined by the larger community. Towards this end, we have created an interactive web
1098 application allowing users to directly explore our scRNA-seq dataset
1099 (https://dymeckilab.hms.harvard.edu/RNAseq_database). With the web app, users can
1100 plot the expression of a gene or several genes of interest, and perform differential
1101 expression analysis. Newly identified *Pet1* neuron subtype marker genes may guide
1102 development of new recombinase driver lines allowing for subtype-specific genetic
1103 access and functional manipulation, and may potentially shape approaches for
1104 developing more targeted therapeutics. Moreover, we hope this work, together with other
1105 recent studies (Huang et al., 2019; Ren et al., 2019), may lead to the development of a
1106 standardized DR *Pet1* neuron subtype nomenclature that allows for consolidation of
1107 experimental results across different labs and different data modalities.

1108 **Methods**

1109 **Intersectional genetic fate mapping**

1110 Triple transgenic mice were generated by crossing *Pet1::Flpe; FrePe* (Brust et al., 2014;
1111 Jensen et al., 2008; Okaty et al., 2015) or *Pet1::Flpe; Ai65* (Madisen et al., 2015) mice
1112 with *Sert::cre* (Gong et al., 2007), *Npy2r::IRES-cre* (Chang et al., 2015), *En1::cre*
1113 (Kimmel et al., 2000), *Crh::cre*
1114 (https://www.mmrrc.org/catalog/sds.php?mmrrc_id=30850), and *P2ry1::IRES-cre*
1115 (Chang et al., 2015) mice, or by crossing *Pet1::Flpe; hM3Dq* (Sciolino et al., 2016) mice
1116 with *Vglut3::IRES-cre* mice (https://www.jax.org/strain/028534). All animals were group
1117 housed (5 animals per ventilated cage) on a 12hr light/dark cycle with access to food
1118 and water ad libitum and were handled and euthanized in accordance with Harvard's
1119 Institutional Animal Care and Use Committee Protocols.

1120 **Perfusion and immunohistochemistry**

1121 Anesthetized mice were transcardially perfused with cold phosphate-buffered saline
1122 (PBS) followed by 4% paraformaldehyde (PFA). Tissue was dissected and fixed in 4%
1123 PFA overnight followed by cryoprotection in 30% sucrose/PBS until equilibrated (~48
1124 hours) before being frozen in tissue freezing medium (Triangle Biomedical Services).
1125 Tissue was cryosectioned in 40um coronal sections and processed as floating sections.

1126 For fluorescent staining, sections were washed with PBS and PBS with 0.1% Triton-X-
1127 100 (PBS-T), blocked in 5% normal donkey serum (NDS) and 1% bovine serum albumin
1128 (BSA) for 2 hours at room temperature (RT), and incubated with primary antibody at 4°C
1129 for 48 hours: anti-GFP (1:3000, chicken polyclonal, Aves Labs, GFP-1020), anti-DsRed
1130 (1:1000, rabbit polyclonal, Takara, 632496), anti-TPH2 (1:1000, rabbit polyclonal, Novus
1131 Biologicals, NB100-74555), anti-Pax5 (1:1000, goat polyclonal, Santa Cruz, sc-1974),
1132 anti-SATB2 (1:1000, guinea pig polyclonal, Synaptic Systems, 327-004), anti-COUP-TFII
1133 (1:1000, mouse monoclonal, Perseus Proteomics, PP-H7 147-00), anti-ZEB2 (1:200,
1134 rabbit polyclonal, MyBioSource, MBS9601451), anti-VGLUT3 (1:500, guinea pig
1135 polyclonal, Synaptic Systems, 135-204), anti-RFP (1:500, rat monoclonal, Chromotek,
1136 5f8-100), anti-Doublecortin (1:1000, goat polyclonal, Santa Cruz, SC-8066), and anti-Ki-
1137 67(1:1000, rat monoclonal, Invitrogen, 14-5698-80). For fluorescent detection, sections
1138 were washed in PBS-T and incubated with species matched secondary antibodies-
1139 Alexa Fluor 488 (donkey anti-chicken, Jackson, 703-545-155), Alexa Fluor 546 (donkey

1140 anti-rabbit, Invitrogen, A10040), Alexa Fluor 647 (donkey anti-goat, Invitrogen, A21447
1141 or donkey anti-mouse, Jackson, 715-605-151), and Cy5 (donkey anti-guinea pig,
1142 Jackson, 706-175-148)- at 1:500 dilution for two hours. Sections were washed in PBS
1143 and 1:3000 DAPI before rinsing and mounting onto slides.

1144 **Confocal and fluorescent microscopy and quantification**

1145 Overview images**:** Overview images of intersectional subtypes were acquired using a 5x
1146 objective on a Zeiss Axioplan2 fluorescence microscope equipped with an Axiocam
1147 digital camera and Axiovision software using 1x1 binning. Images were then cropped to
1148 a 1000x1000 pixel square containing the dorsal raphe. Images showing the distribution
1149 of PAX5, SATB2, and NR2F2 are 2x2 tiled maximum intensity images acquired using a
1150 Plan Apo λ 20x/0.75 DIC I objective on a spinning disk confocal. Images showing TPH2
1151 and VGLUT3 staining are a single optical slice taken on a spinning disk confocal using a
1152 Plan Apo λ 20x/0.75 DIC I objective or Plan Fluor 40x/1.3 Oil DIC H/N2 objective
1153 respectively. Images were cropped to create a zoomed image of the region of interest.

1154 Flat mount of lateral wall of lateral ventricle: *P2ry1::IRES-cre; Pet1::Flpe; Ai65* mice
1155 (n=4) were transcardially perfused with cold PBS. Lateral wall dissection was completed
1156 as described in Mirzadeh, et.al, 2010. Briefly, brains were dissected into PBS and split
1157 into two hemispheres. The hippocampus was removed, exposing the lateral wall, and
1158 the brain was fixed overnight in 4% PFA in PBS. The remainder of the microdissection of
1159 the lateral wall was then completed and immediately proceeded to
1160 immunohistochemistry as described above.

1161 Quantification of immunofluorescence: Quantification of PAX5, NR2F2, and SATB2 was
1162 completed in *Vglut3::IRES-cre; Pet1::Flpe; hM3Dq* animals, where cells expressing both
1163 *Vglut3::IRES-cre* and *Pet1::Flpe* express an hM3Dq-mCherry fusion and all other *Pet1+*
1164 cells express EGFP. Images were acquired as 2x2 tiles as a z-stack (0.9um step) using
1165 a Plan Apo λ 20x/0.75 DIC I objective on a spinning disk confocal and cropped into
1166 equally sized non-overlapping subregions (1000x1000 pixel) spanning the rostral to
1167 caudal extent of the dorsal raphe. Cells were counted positive if antibody staining for the
1168 protein of interest overlapped with DAPI staining and was within a DsRed + cell
1169 (*Vglut3::cre;Pet1::Flpe* lineage) or a GFP+ cell (subtractive *Pet1* lineage). All counts
1170 were completed in images taken from 2 to 4 animals depending on the brain region.

1171 Images used for the quantification of VGLUT3 antibody staining were acquired using a
1172 Plan Fluor 40x/1.3 Oil DIC H/N2 objective on a spinning disk confocal on non-
1173 overlapping anatomical subdivisions of the dorsal raphe. Cells were counted positive
1174 based on the overlap of VGLUT3 antibody staining with mCherry (*VGlut3::cre;Pet1::Flpe*
1175 lineage) or a EGFP (subtractive *Pet1* lineage) staining. In the case of TPH2
1176 quantification, *En1::cre; Pet1::Flpe; FrePe* animals were used (EGFP+ *En1::cre;*
1177 *Pet1::Flpe* intersectional lineage cells). Images were acquired as 2x2 tiles as a z-stack
1178 (0.9um step) using a Plan Apo λ 20x/0.75 DIC I objective on a spinning disk confocal
1179 and cropped into equally sized non-overlapping subregions (1000x1000 pixel) spanning
1180 the rostral to caudal extent of the dorsal raphe. Cells were counted positive based on
1181 colocalization of TPH2 antibody staining with EGFP. All quantification was performed by
1182 an experienced observer blinded to the anatomical region of the image in a minimum of
1183 two animals per region.

1184 **TPH2/*Tph2* dual immunofluorescence and RNAscope**

1185 Transgenic *En1::cre; Pet1::Flpe; RC::FrePe* mice were briefly anesthetized with
1186 isoflurane and immediately perfused intracardially with phosphate buffered saline (PBS)
1187 followed by 4% paraformaldehyde (PFA) in PBS. Brains were extracted and fixed for 16
1188 hours in 4% PFA at 4˚C, and were then cryoprotected using 30% sucrose in PBS for 48
1189 hours and subsequently embedded in OCT compound (Tissue-Tek). Coronal sections
1190 were cut on a cryostat into PBS at 20 µm thickness, rinsed three times with PBS for 10
1191 min and frozen in cryo-storage solution at -30˚C. The day before RNAscope® (ACDBio)
1192 procedure, the sections were mounted on slides and dried at room temperature (RT)
1193 overnight. Prior to RNAscope, the slides were heated on a slide warmer at 50˚C for 30
1194 min. Sections were re-fixed with 4% PFA for 15 min at RT, followed by Protease III
1195 treatment for 30 min at 40˚C. RNAscope was performed based on the manufacturer's
1196 protocol: mouse *Tph2*-C2 probe (ACDbio Cat# 318691-C2) and Amp4 AltA were used
1197 for hybridization. After the last wash of RNAscope®, the slides were washed briefly with
1198 PBS followed by permeabilization and blocking with 0.3% TritonX-100 and 5% Normal
1199 Donkey Serum (NDS, Jackson ImmunoResearch) in PBS for 1 hour at RT. Then the
1200 sections were incubated with primary antibodies in 0.3% TritonX-100 and 3% NDS in
1201 PBS for 16 hours at 4˚C. Primary antibodies: chicken polyclonal anti-GFP (1:1000; GFP-
1202 1010; Aves Labs), rabbit polyclonal anti-Tph2 (1:1000; NB100-74555; Novus Biological).
1203 Sections were then washed with PBS three times for 10 min and incubated with

1204 secondary antibodies for 2 hours at RT. Secondary antibodies: donkey anti-chicken IgG-
1205 Alexa Fluor® 488 (1:500, Jackson ImmunoResearch Laboratories, Inc.), donkey anti-
1206 rabbit IgG-Alexa Fluor® 647 (1:500, ThermoFisher Scientific.). DAPI (4', 6-diamidino-2-
1207 phenylindole) was used for nuclear counterstaining.
1208

1209 Image acquisition and analysis: Images were collected on a Nikon Ti2 inverted
1210 microscope with a Yokowaga CSU-W1 spinning disk with a 50 µm pinhole disk, using a
1211 Nikon Plan Apo λ 60x/1.4 NA oil-immersion objective and laser lines at 405, 488, 561,
1212 and 640 nm, and captured using an Andor Zyla 4.2 Plus sCMOS monochrome camera
1213 and Nikon Elements Acquisition Softwarre AR 5.02. Laser settings were adjusted for
1214 each sample but kept constant throughout image collection. A custom Fiji (Schindelin et
1215 al., 2012) macro script was used to process and analyze these images in a semi-
1216 automatic manner. Analysis was performed on maximum intensity projections of 5 µm
1217 thick z-stacks. To segment cells, the GFP and TPH2 channels were processed with a
1218 100 pixel rolling ball background subtraction to remove uneven background fluorescence
1219 and a 2 pixel gaussian blur to aid in cell segmentation. Cells were segmented first by
1220 automatic thresholding using the "Default" Fiji autothreshold method. Cells in the
1221 resulting binary images were separated using the Adjustable Watershed plugin (Michael
1222 Schmid, https://imagejdocu.tudor.lu/plugin/segmentation/adjustable_watershed/start),
1223 which allows the user to manually adjust the default ImageJ binary watershed tolerance.
1224 Next, cells were filtered for size (minimum area 70 μm^2) and circularity (minimum 0.3)
1225 using Fiji's "Analyze Particles." Segmented cells were checked manually by a user who
1226 could delete or redraw ROIs using the freehand tool and the ROI manager. After
1227 segmenting both channels sequentially, 2D overlap-based colocalization of the TPH2
1228 and GFP-labeled cells was performed in which a cell was considered as 'colocalized' if
1229 area overlap was greater than 60% of the GFP area (determined empirically). To
1230 quantify *Tph2* RNAscope puncta within cells, a 50 pixel rolling ball background
1231 subtraction was applied before isolating puncta as local intensity maxima using the Fiji
1232 "Find Maxima" function with a prominence level of 100. RNAscope puncta were then
1233 counted within each cell ROI and resulting data were output to a spreadsheet. For GFP^+
1234 soma located close to $TPH2^+$ cells such that their outlines in the maximum projection
1235 partially overlapped with TPH2 signal but did not reach the colocalization criterion,

1236 RNAscope puncta were only counted in the TPH2$^-$ region of the cell soma to avoid
1237 including puncta belonging to the neighboring cell.

1238 **Stereotaxic Surgery**

1239 Mice were anesthetized with 1.5-2.0% isofluorane and placed in a stereotaxic system
1240 (Kopf). Using a Micro4 injector (WPI) and Nanofil sytringe equipped with a metal 33g
1241 beveled needle (WPI) 75nL of pENN.AAV.hSyn.Cre.WPRE.hGH was injected at
1242 50nL/min into the lateral ventricle using using the following stereotaxic coordinates: -
1243 0.34mm AP, + 1.00mm LM, -2.25mm DV (AP is relative to bregma). After surgery, mice
1244 recovered on a heated pad until ambulatory and returned to their home cage.
1245 pENN.AAV.hSyn.Cre.WPRE.hGH was a gift from James M. Wilson (Addgene viral prep
1246 #105553-AAVrg ; httm://n2t.net/addgene:105553 ; RRID:Addgene_105553).

1247 **Single-cell sorting and RNA sequencing**

1248 <u>On-chip Sort, 10X library preparation, and RNA sequencing:</u> Data was derived from two
1249 different experiments composed of brain tissue harvested from *En1::cre; Pet1::Flpe;*
1250 *FrePe* mice (n=4) or *Pet1::Flpe; RC::FL-hM3Dq* mice (n=6). Tissue was sectioned on a
1251 vibratome and protease-digested in ACSF containing activity blockers as described in
1252 (Hempel et al., 2007). The dorsal raphe was micro-dissected under an upright dissection
1253 microscope with fluorescence optics and all tissue was combined in a 1.5mL Eppendorf
1254 tube containing 500ul of filtered ACSF/1%FBS. Tissue was then gently triturated using
1255 glass micropipettes of decreasing diameter until achieving a mostly homogeneous
1256 single-cell suspension without visible tissue chunks. One drop of NucBlue (Thermo
1257 Fisher Scientific) was added to the cell suspension and allowed to sit for 20 minutes (to
1258 aid in sorting and cell quantification). EGFP-marked, NucBlue-positive cells were sorted
1259 using the On-chip Sort (On-chip Biotechnologies Co., Ltd.). Final cell concentration was
1260 determined by counting the number of cells in 10ul of the sorted output using a
1261 hemacytometer. Cells were then run through the 10X Genomics Chromium Single Cell 3'
1262 v3 protocol, and libraries were sequenced on an Illumina NextSeq 500 sequencer to a
1263 mean depth of ~115,000 reads per cell.

1264 <u>Manual Sorting and RNA sequencing</u>: Brain tissue was harvested from triple transgenic
1265 animals – *Sert::cre;Pet1::Flpe;FrePe*, *Npy2r::IRES-cre Pet1::Flpe;FrePe,*

1266 *Crh::cre;Pet1::Flpe;FrePe,* and *P2ry1::IRES-cre* (p60-p120, a minimum of two mice per
1267 condition) and fluorescently labeled cells were sorted as described in (Okaty et al.,
1268 2015). Briefly, the brainstem was sectioned into 400um coronal sections using a
1269 vibratome. Sections were bubbled in artificial cerebrospinal fluid (ACSF) containing
1270 activity blockers for at least 5 minutes before being transferred to ACSF containing
1271 1mg/ml pronase for 1 hour. Slices were then returned to protease-free ACSF for 15
1272 minutes, before regions of interest were micro-dissected. Anatomical subdivisions of the
1273 dorsal raphe were made based on the shape of the dorsal raphe and landmarks
1274 including fiber tracts and the aqueduct (as indicated in **Figure 4A**). Dissected chunks of
1275 tissue were transferred first to a clean 35-mm dish containing ACSF and then to a 1.5mL
1276 Eppendorf tube containing 1mL of filtered ACSF/1% FBS. Tissue was then gently
1277 triturated until without visible chunks. Dissociated cells were diluted and poured into a
1278 Petri dish. Fluorescently marked cells were aspirated using mouth aspiration and moved
1279 into 3 consecutive wash dishes. Each cell was then aspirated a final time and deposited
1280 into an individual 0.5mL tube containing 9.5ul of nuclease-free water and 1ul of 10x
1281 Reaction Buffer (Smart-Seq V4 Ultra Low Input RNA kit, Takara Bio) and allowed to
1282 incubate at room temperature for 5 minutes before being stored at -80deg until cDNA
1283 synthesis. Single cells were converted to cDNA and amplified using Smart-Seq V4 Ultra
1284 Low Input RNA Kit (Takara Bio). The cDNA output was then processed with Nextera XT
1285 DNA Library Preparation Kit. Quantification and quality control were assessed with
1286 TapeStation. Libraries were then sequenced on either an Illumina HiSeq 2500 (50 base-
1287 pair, single-end) or NextSeq 500 (75-bp, paired-end) to a mean depth of ~4,000,000
1288 reads per cell.

1289 **scRNA-seq Analysis**

1290 <u>10X scRNA-seq data:</u> Transcriptome mapping (using the mm10 genome assembly) and
1291 demultiplexing were performed using the 10X Genomics Cell Ranger software (version
1292 3.0.2). Several data-filtering steps were performed on the matrix of transcript counts
1293 (using R version 3.5.3) prior to further analysis. First, we filtered out all genes detected in
1294 fewer than ten single-cell libraries, and filtered out all libraries with less than 4,500
1295 detected genes. This threshold was selected based on the histogram of gene detection
1296 for all single-cell libraries as initially called by the Cell Ranger cell detection algorithm,
1297 which appeared to reflect two different distributions corresponding to low-complexity
1298 versus high-complexity libraries. The low-complexity distribution was right-skewed and

1299 had a mode of less than 1,000 detected genes, whereas the high-complexity distribution
1300 was left-skewed and had a mode of ~7,500 detected genes. 4,500 genes was roughly
1301 the boundary between the two distributions; i.e. the minima between the two modes, and
1302 also corresponded to a sharp inflection point in the Barcodes versus UMI counts plot in
1303 the web_summary.html file generated by Cell Ranger. While many of these low-
1304 complexity libraries may have been misidentified as cells by Cell Ranger (e.g. droplets
1305 containing transcripts from lysed cells, rather than intact cells) examination of genes
1306 enriched in lower-complexity libraries suggested that some of them reflected unhealthy
1307 cells (e.g. libraries with high mitochondrial gene expression) or contaminating non-
1308 neuronal cells (e.g. libraries enriched for glial marker genes). Notably, the number of
1309 cells with high-complexity libraries corresponded well with our estimated number of
1310 EGFP positive cells used as input to the 10X chip. We further excluded libraries with: (1)
1311 evidence of glial contamination, based on high-outlier expression of glial marker genes,
1312 including *Plp1*, *Olig1*, and *Aqp4*, (2) absence or low-outlier levels of *Pet1/Fev* transcripts,
1313 (3) greater than fifteen percent of detected genes corresponding with mitochondrial
1314 genes, (4) less than two percent of detected genes corresponding with ribosomal genes
1315 (these appeared to be single-nuclei libraries, rather than single-cell), (5) high-outlier UMI
1316 counts, and (6) high-outlier gene detection. 2,350 single-cell libraries and 17,231 genes
1317 passed the above filtering criteria.

1318 Next, we created a Seurat object using these filtered data (Seurat version 3.0.2). Data
1319 were log-normalized using the NormalizeData function (using the default scale factor of
1320 1e4), and we identified the top two thousand genes (or in some cases non-coding RNAs)
1321 with the most highly variable transcript expression across single cells using the
1322 FindVariableFeatures function (selection.method = “vst”, nfeatures=2000). We then
1323 scaled and centered the log-normalized data using the ScaleData function and carried
1324 out principal components analysis (PCA) on the scaled expression values of the two
1325 thousand most highly variable genes. This allowed us to reduce the dimensionality of the
1326 data onto a smaller set of composite variables representing the most salient gene
1327 expression differences across single neurons. The procedure for identifying meaningful
1328 *Pet1* neuron subtype clusters is thoroughly described in the Results section of the main
1329 text. Briefly, we systematically varied the number of principal components included and
1330 the resolution parameter in the functions FindNeighbors, FindClusters, and RunUMAP,
1331 Dendrograms were created using BuildClusterTree and PlotClusterTree, and cluster-

1332 enriched genes were identified using the FindAllMarkers function, with min.pct = 0.25
1333 and logfc.threshold = 0.25, using Wilcoxon Rank Sum tests. This function adjusts p-
1334 values for multiple comparisons using the Bonferroni correction. All genes found to be
1335 significantly enriched or "de-enriched" (i.e. expressed at a significantly lower level) in
1336 each cluster, as well as the top two thousand highest variance genes, can be found in
1337 the Supplemental Excel Spreadsheet.

1338 Manual scRNA-seq data: Transcript mapping to the mm10 genome assembly and
1339 feature counts were performed using STAR (version 2.5.4) (Dobin and Gingeras, 2016).
1340 Given the high purity of manual cell sorting and the high sensitivity of SMART-Seq v4
1341 cDNA amplification, no data filtering was required; i.e. single-cell libraries showed no
1342 evidence for off-target contamination and showed consistently high gene detection
1343 (~9,000 genes per single-cell). Counts data were analyzed using Seurat as described
1344 for 10X scRNA-seq data.

1345 scRNA-seq data availability: RNA-seq data (manual and 10X) are available through the
1346 Gene Expression Omnibus (GEO), accession number GSE144980.

1347 Transfer of 10X cell type labels: In order to explore the correspondence between the
1348 fourteen 10X scRNA-seq data-defined *Pet1* neuron subtypes and other scRNA-seq data,
1349 including our manual scRNA-seq data, and the Huang, et al. 2019 and Ren, et al. 2019
1350 datasets, we employed the strategy outlined in (Stuart et al., 2019). Specifically, we used
1351 the Seurat functions FindTransferAnchors and TransferData, using the 10X data as the
1352 "reference" and the other datasets as the "query" group.

1353 **Electrophysiology methods**

1354 *In vitro* brainstem slice preparations containing dorsal raphe serotonin neurons were
1355 obtained from 4-5 week old mice. After isofluorane anesthesia, mice were perfused
1356 transcardially with a solution of artificial CSF ($NaHCO_3$-aCSF) containing the following
1357 (in mM): 124 NaCl, 25 NaHCO3, 3 KCl, 2 CaCl2, 2 $MgCl_2$, 1.2, NaH2PO4 and 25 d-
1358 Glucose, equilibrated with 95% O2 and 5% CO2 adjusted to 310 ± 5 mOsm/L. The
1359 brainstem was dissected and mounted on the stage of a VT1200S vibratome while
1360 immersed in an ice slush solution aCSF containing the following (in mM): NMDG 93, HCl
1361 93, KCL 2.5, NaH_2P0_4 1.2, $NaHCO_3$ 30, HEPES 20, d-Glucose 25, Na-Ascorbate 5,

1362 Thiourea 2, Na-Pyruvate 3, $MgSO_4$ 10, $CaCl_2$ 0.5 equilibrated with 95% O2 and 5% CO2
1363 adjusted to 310 ± 5 mOsm/L. Coronal slices 200 µm thick containing the dorsal nucleus
1364 raphe were recovered for 1h at 35-6 C in HEPES-aCSF containing: NaCl 92, KCl 2.5,
1365 NaH_2P0_4 1.2, $NaHCO_3$ 30, HEPES 20, Glucose 25, Na-Ascorbate 5, Thiourea 2,
1366 NaPyruvate 3, $MgSO_4$ 10, $CaCl_2$ 0.5 equilibrated with 95% O2 and 5% CO2 adjusted to
1367 310 ± 5 mOsm/L and placed at room temperature for storage. Individual slices were
1368 transferred to the recording chamber and superfused with NaHCO3-aCSF at
1369 34ºC. Electrodes (5–7 MΩ) were pulled from borosilicate glass. Pipettes were filled with
1370 (in mM): 140 K-gluconate, HEPES 10, KCl 5, Na-ATP 2, $MgCl_2$ 2, EGTA 0.02, biocytin
1371 0.1% Na_2GTP 0.5, Na_2-phosphocreatine 4, pH 7.4 adjusted with KOH and adjusted to
1372 285 ± 5 mOsm/L with sucrose. Somatic whole-cell recordings were obtained with a
1373 Multiclamp 700B amplifier, signals were acquired and sampled at 100 kHz
1374 using Digidata 1440A digitizing board. Pipette capacitance was compensated ≈70% in
1375 current clamp (CC). Series resistance (*R*s) was typically 9–15 MΩ. Cells with *R*s > 15
1376 MΩ were discarded. A measured liquid junction potential of ≈10 mV was corrected
1377 online. Cells were held at V_h= -80 mV unless otherwise indicated. To create action
1378 potential frequency-current curves, a protocol that applies a series of 750 ms current
1379 pulses ranging from -100 pA to 220 pA was created using Molecular Devices Clampex
1380 10.7 software running on Windows 7.

1381 **Acknowledgments**

1382 The authors thank the Biopolymers Facility at HMS for assistance with next-generation
1383 sequencing; the Microscopy Resources on the North Quad (MicRoN) core at Harvard
1384 Medical School for microscope use and training; Steve Liberles for providing
1385 *Npy2r::IRES-cre* and *P2ry1::IRES-cre* driver lines; ChangHee Lee and Jin Akagi for
1386 advice with the On-chip Sort; Kathryn Commons and the Dymecki lab for discussions
1387 and thoughtful comments on this manuscript; J.J Mai for reagents and animal
1388 husbandry. Grants supporting this work include NARSAD Young Investigator Grant
1389 (BWO), NIDA Grant RO1DA034022 (BWO, OVA, SMD), T32 HL 007901 (NS),
1390 NIH F31NS108406 (RAS), Howard Hughes Medical Institute Gilliam Fellowship (KAL),
1391 NIH F99-NS108515 (KAL), Harvard Brain Science Initiative Bipolar Disorder Seed Grant,
1392 supported by Kent and Liz Dauten (OVA), and the GVR Khodadad Fund for the Study of
1393 Genetic, Neurobiological, and Physiochemical Processes of EPS (OVA, BWO, SMD).

1394 **References**

1395 Abrams, J.K., Johnson, P.L., Hollis, J.H., and Lowry, C.A. (2004). Anatomic and
1396 functional topography of the dorsal raphe nucleus. Ann N Y Acad Sci 1018, 46-57.
1397 Aghajanian, G.K., and Gallager, D.W. (1975). Raphe origin of serotonergic nerves
1398 terminating in the cerebral ventricles. Brain Res 88, 221-231.
1399 Alfonso, J., Penkert, H., Duman, C., Zuccotti, A., and Monyer, H. (2015).
1400 Downregulation of Sphingosine 1-Phosphate Receptor 1 Promotes the Switch from
1401 Tangential to Radial Migration in the OB. J Neurosci 35, 13659-13672.
1402 Alonso, A., Merchan, P., Sandoval, J.E., Sanchez-Arrones, L., Garcia-Cazorla, A., Artuch,
1403 R., Ferran, J.L., Martinez-de-la-Torre, M., and Puelles, L. (2013). Development of the
1404 serotonergic cells in murine raphe nuclei and their relations with rhombomeric
1405 domains. Brain Struct Funct 218, 1229-1277.
1406 Amilhon, B., Lepicard, E., Renoir, T., Mongeau, R., Popa, D., Poirel, O., Miot, S., Gras, C.,
1407 Gardier, A.M., Gallego, J.*, et al.* (2010). VGLUT3 (vesicular glutamate transporter type
1408 3) contribution to the regulation of serotonergic transmission and anxiety. J
1409 Neurosci 30, 2198-2210.
1410 Andrade, R., and Haj-Dahmane, S. (2013). Serotonin neuron diversity in the dorsal
1411 raphe. ACS Chem Neurosci 4, 22-25.
1412 Asano, M., and Gruss, P. (1992). Pax-5 is expressed at the midbrain-hindbrain
1413 boundary during mouse development. Mech Dev 39, 29-39.
1414 Azmitia, E.C., and Segal, M. (1978). An autoradiographic analysis of the differential
1415 ascending projections of the dorsal and median raphe nuclei in the rat. J Comp
1416 Neurol 179, 641-667.
1417 Baker, K.G., Halliday, G.M., Halasz, P., Hornung, J.P., Geffen, L.B., Cotton, R.G., and
1418 Tork, I. (1991a). Cytoarchitecture of serotonin-synthesizing neurons in the pontine
1419 tegmentum of the human brain. Synapse 7, 301-320.
1420 Baker, K.G., Halliday, G.M., Hornung, J.P., Geffen, L.B., Cotton, R.G., and Tork, I.
1421 (1991b). Distribution, morphology and number of monoamine-synthesizing and
1422 substance P-containing neurons in the human dorsal raphe nucleus. Neuroscience
1423 42, 757-775.
1424 Baker, K.G., Halliday, G.M., and Tork, I. (1990). Cytoarchitecture of the human dorsal
1425 raphe nucleus. J Comp Neurol 301, 147-161.
1426 Bakken, T.E., Hodge, R.D., Miller, J.A., Yao, Z., Nguyen, T.N., Aevermann, B., Barkan, E.,
1427 Bertagnolli, D., Casper, T., Dee, N.*, et al.* (2018). Single-nucleus and single-cell
1428 transcriptomes compared in matched cortical cell types. PLoS One 13, e0209648.
1429 Banasr, M., Hery, M., Printemps, R., and Daszuta, A. (2004). Serotonin-induced
1430 increases in adult cell proliferation and neurogenesis are mediated through
1431 different and common 5-HT receptor subtypes in the dentate gyrus and the
1432 subventricular zone. Neuropsychopharmacology 29, 450-460.
1433 Bang, S.J., and Commons, K.G. (2012). Forebrain GABAergic projections from the
1434 dorsal raphe nucleus identified by using GAD67-GFP knock-in mice. J Comp Neurol
1435 520, 4157-4167.

1436 Bang, S.J., Jensen, P., Dymecki, S.M., and Commons, K.G. (2012). Projections and
1437 interconnections of genetically defined serotonin neurons in mice. Eur J Neurosci
1438 35, 85-96.
1439 Barrett, K.T., Dosumu-Johnson, R.T., Daubenspeck, J.A., Brust, R.D., Kreouzis, V., Kim,
1440 J.C., Li, A., Dymecki, S.M., and Nattie, E.E. (2016). Partial Raphe Dysfunction in
1441 Neurotransmission Is Sufficient to Increase Mortality after Anoxic Exposures in Mice
1442 at a Critical Period in Postnatal Development. J Neurosci 36, 3943-3953.
1443 Beaudet, A., and Descarries, L. (1976). Quantitative data on serotonin nerve
1444 terminals in adult rat neocortex. Brain Res 111, 301-309.
1445 Bellido, I., Hansson, A.C., Gomez-Luque, A.J., Andbjer, B., Agnati, L.F., and Fuxe, K.
1446 (2004). Corticosterone strongly increases the affinity of dorsal raphe 5-HT1A
1447 receptors. Neuroreport 15, 1457-1459.
1448 Brezun, J.M., and Daszuta, A. (1999). Depletion in serotonin decreases neurogenesis
1449 in the dentate gyrus and the subventricular zone of adult rats. Neuroscience 89,
1450 999-1002.
1451 Bruchas, M.R., Land, B.B., and Chavkin, C. (2010). The dynorphin/kappa opioid
1452 system as a modulator of stress-induced and pro-addictive behaviors. Brain Res
1453 1314, 44-55.
1454 Brust, R.D., Corcoran, A.E., Richerson, G.B., Nattie, E., and Dymecki, S.M. (2014).
1455 Functional and developmental identification of a molecular subtype of brain
1456 serotonergic neuron specialized to regulate breathing dynamics. Cell Rep 9, 2152-
1457 2165.
1458 Butler, A., Hoffman, P., Smibert, P., Papalexi, E., and Satija, R. (2018). Integrating
1459 single-cell transcriptomic data across different conditions, technologies, and species.
1460 Nat Biotechnol 36, 411-420.
1461 Calizo, L.H., Akanwa, A., Ma, X., Pan, Y.Z., Lemos, J.C., Craige, C., Heemstra, L.A., and
1462 Beck, S.G. (2011). Raphe serotonin neurons are not homogenous:
1463 electrophysiological, morphological and neurochemical evidence.
1464 Neuropharmacology 61, 524-543.
1465 Campbell, J.N., Macosko, E.Z., Fenselau, H., Pers, T.H., Lyubetskaya, A., Tenen, D.,
1466 Goldman, M., Verstegen, A.M., Resch, J.M., McCarroll, S.A*., et al.* (2017). A molecular
1467 census of arcuate hypothalamus and median eminence cell types. Nat Neurosci 20,
1468 484-496.
1469 Celada, P., Puig, M.V., Casanovas, J.M., Guillazo, G., and Artigas, F. (2001). Control of
1470 dorsal raphe serotonergic neurons by the medial prefrontal cortex: Involvement of
1471 serotonin-1A, GABA(A), and glutamate receptors. J Neurosci 21, 9917-9929.
1472 Challis, C., Boulden, J., Veerakumar, A., Espallergues, J., Vassoler, F.M., Pierce, R.C.,
1473 Beck, S.G., and Berton, O. (2013). Raphe GABAergic neurons mediate the acquisition
1474 of avoidance after social defeat. J Neurosci 33, 13978-13988, 13988a.
1475 Chang, R.B., Strochlic, D.E., Williams, E.K., Umans, B.D., and Liberles, S.D. (2015).
1476 Vagal Sensory Neuron Subtypes that Differentially Control Breathing. Cell 161, 622-
1477 633.
1478 Chavkin, C., James, I.F., and Goldstein, A. (1982). Dynorphin is a specific endogenous
1479 ligand of the kappa opioid receptor. Science 215, 413-415.

1480 Chen, C.H., Battaglioli, G., Martin, D.L., Hobart, S.A., and Colon, W. (2003). Distinctive
1481 interactions in the holoenzyme formation for two isoforms of glutamate
1482 decarboxylase. Biochim Biophys Acta 1645, 63-71.
1483 Chen, C.P., Eastwood, S.L., Hope, T., McDonald, B., Francis, P.T., and Esiri, M.M.
1484 (2000). Immunocytochemical study of the dorsal and median raphe nuclei in
1485 patients with Alzheimer's disease prospectively assessed for behavioural changes.
1486 Neuropathol Appl Neurobiol 26, 347-355.
1487 Commons, K.G. (2009). Locally collateralizing glutamate neurons in the dorsal raphe
1488 nucleus responsive to substance P contain vesicular glutamate transporter 3
1489 (VGLUT3). J Chem Neuroanat 38, 273-281.
1490 Commons, K.G. (2015). Two major network domains in the dorsal raphe nucleus. J
1491 Comp Neurol 523, 1488-1504.
1492 Commons, K.G. (2016). Ascending serotonin neuron diversity under two umbrellas.
1493 Brain Struct Funct 221, 3347-3360.
1494 Condomitti, G., and de Wit, J. (2018). Heparan Sulfate Proteoglycans as Emerging
1495 Players in Synaptic Specificity. Front Mol Neurosci 11, 14.
1496 Crawford, L.K., Craige, C.P., and Beck, S.G. (2010). Increased intrinsic excitability of
1497 lateral wing serotonin neurons of the dorsal raphe: a mechanism for selective
1498 activation in stress circuits. J Neurophysiol 103, 2652-2663.
1499 Dahlstroem, A., and Fuxe, K. (1964). Evidence for the Existence of Monoamine-
1500 Containing Neurons in the Central Nervous System. I. Demonstration of
1501 Monoamines in the Cell Bodies of Brain Stem Neurons. Acta Physiol Scand Suppl,
1502 SUPPL 232:231-255.
1503 Dengler-Crish, C.M., Smith, M.A., and Wilson, G.N. (2017). Early Evidence of Low
1504 Bone Density and Decreased Serotonergic Synthesis in the Dorsal Raphe of a
1505 Tauopathy Model of Alzheimer's Disease. J Alzheimers Dis 55, 1605-1619.
1506 Di Donato, V., De Santis, F., Albadri, S., Auer, T.O., Duroure, K., Charpentier, M.,
1507 Concordet, J.P., Gebhardt, C., and Del Bene, F. (2018). An Attractive Reelin Gradient
1508 Establishes Synaptic Lamination in the Vertebrate Visual System. Neuron 97, 1049-
1509 1062 e1046.
1510 Doan, R.N., Lim, E.T., De Rubeis, S., Betancur, C., Cutler, D.J., Chiocchetti, A.G.,
1511 Overman, L.M., Soucy, A., Goetze, S., Autism Sequencing, C., *et al.* (2019). Recessive
1512 gene disruptions in autism spectrum disorder. Nat Genet 51, 1092-1098.
1513 Dobin, A., and Gingeras, T.R. (2016). Optimizing RNA-Seq Mapping with STAR.
1514 Methods Mol Biol 1415, 245-262.
1515 Dymecki, S.M., Ray, R.S., and Kim, J.C. (2010). Mapping cell fate and function using
1516 recombinase-based intersectional strategies. Methods Enzymol 477, 183-213.
1517 El Mestikawy, S., Wallen-Mackenzie, A., Fortin, G.M., Descarries, L., and Trudeau, L.E.
1518 (2011). From glutamate co-release to vesicular synergy: vesicular glutamate
1519 transporters. Nat Rev Neurosci 12, 204-216.
1520 Ellegood, J., Nakai, N., Nakatani, J., Henkelman, M., Takumi, T., and Lerch, J. (2015).
1521 Neuroanatomical Phenotypes Are Consistent With Autism-Like Behavioral
1522 Phenotypes in the 15q11-13 Duplication Mouse Model. Autism Res 8, 545-555.
1523 Erbel-Sieler, C., Dudley, C., Zhou, Y., Wu, X., Estill, S.J., Han, T., Diaz-Arrastia, R.,
1524 Brunskill, E.W., Potter, S.S., and McKnight, S.L. (2004). Behavioral and regulatory

1525 abnormalities in mice deficient in the NPAS1 and NPAS3 transcription factors. Proc
1526 Natl Acad Sci U S A 101, 13648-13653.
1527 Erickson, J.D., Eiden, L.E., and Hoffman, B.J. (1992). Expression cloning of a
1528 reserpine-sensitive vesicular monoamine transporter. Proc Natl Acad Sci U S A 89,
1529 10993-10997.
1530 Erlander, M.G., Tillakaratne, N.J., Feldblum, S., Patel, N., and Tobin, A.J. (1991). Two
1531 genes encode distinct glutamate decarboxylases. Neuron 7, 91-100.
1532 Evrard, A., Barden, N., Hamon, M., and Adrien, J. (2006). Glucocorticoid receptor-
1533 dependent desensitization of 5-HT1A autoreceptors by sleep deprivation: studies in
1534 GR-i transgenic mice. Sleep 29, 31-36.
1535 Fernandez, S.P., Cauli, B., Cabezas, C., Muzerelle, A., Poncer, J.C., and Gaspar, P.
1536 (2016). Multiscale single-cell analysis reveals unique phenotypes of raphe 5-HT
1537 neurons projecting to the forebrain. Brain Struct Funct 221, 4007-4025.
1538 Fox, S.R., and Deneris, E.S. (2012). Engrailed is required in maturing serotonin
1539 neurons to regulate the cytoarchitecture and survival of the dorsal raphe nucleus. J
1540 Neurosci 32, 7832-7842.
1541 Fremeau, R.T., Jr., Burman, J., Qureshi, T., Tran, C.H., Proctor, J., Johnson, J., Zhang, H.,
1542 Sulzer, D., Copenhagen, D.R., Storm-Mathisen, J.*, et al.* (2002). The identification of
1543 vesicular glutamate transporter 3 suggests novel modes of signaling by glutamate.
1544 Proc Natl Acad Sci U S A 99, 14488-14493.
1545 Fu, W., Le Maitre, E., Fabre, V., Bernard, J.F., David Xu, Z.Q., and Hokfelt, T. (2010).
1546 Chemical neuroanatomy of the dorsal raphe nucleus and adjacent structures of the
1547 mouse brain. J Comp Neurol 518, 3464-3494.
1548 Funahashi, J., Okafuji, T., Ohuchi, H., Noji, S., Tanaka, H., and Nakamura, H. (1999).
1549 Role of Pax-5 in the regulation of a mid-hindbrain organizer's activity. Dev Growth
1550 Differ 41, 59-72.
1551 Fyodorov, D., Nelson, T., and Deneris, E. (1998). Pet-1, a novel ETS domain factor
1552 that can activate neuronal nAchR gene transcription. J Neurobiol 34, 151-163.
1553 Gagnon, D., and Parent, M. (2014). Distribution of VGLUT3 in highly collateralized
1554 axons from the rat dorsal raphe nucleus as revealed by single-neuron
1555 reconstructions. PLoS One 9, e87709.
1556 Gaspar, P., and Lillesaar, C. (2012). Probing the diversity of serotonin neurons.
1557 Philos Trans R Soc Lond B Biol Sci 367, 2382-2394.
1558 Goncalves, L., Nogueira, M.I., Shammah-Lagnado, S.J., and Metzger, M. (2009).
1559 Prefrontal afferents to the dorsal raphe nucleus in the rat. Brain Res Bull 78, 240-
1560 247.
1561 Gong, S., Doughty, M., Harbaugh, C.R., Cummins, A., Hatten, M.E., Heintz, N., and
1562 Gerfen, C.R. (2007). Targeting Cre recombinase to specific neuron populations with
1563 bacterial artificial chromosome constructs. J Neurosci 27, 9817-9823.
1564 Gras, C., Herzog, E., Bellenchi, G.C., Bernard, V., Ravassard, P., Pohl, M., Gasnier, B.,
1565 Giros, B., and El Mestikawy, S. (2002). A third vesicular glutamate transporter
1566 expressed by cholinergic and serotoninergic neurons. J Neurosci 22, 5442-5451.
1567 Guo, Y.P., and Commons, K.G. (2017). Serotonin neuron abnormalities in the BTBR
1568 mouse model of autism. Autism Res 10, 66-77.

1569 Hale, M.W., and Lowry, C.A. (2011). Functional topography of midbrain and pontine
1570 serotonergic systems: implications for synaptic regulation of serotonergic circuits.
1571 Psychopharmacology (Berl) 213, 243-264.
1572 Harburg, G.C., Hall, F.S., Harrist, A.V., Sora, I., Uhl, G.R., and Eisch, A.J. (2007).
1573 Knockout of the mu opioid receptor enhances the survival of adult-generated
1574 hippocampal granule cell neurons. Neuroscience 144, 77-87.
1575 Hempel, C.M., Sugino, K., and Nelson, S.B. (2007). A manual method for the
1576 purification of fluorescently labeled neurons from the mammalian brain. Nat Protoc
1577 2, 2924-2929.
1578 Hendricks, T., Francis, N., Fyodorov, D., and Deneris, E.S. (1999). The ETS domain
1579 factor Pet-1 is an early and precise marker of central serotonin neurons and
1580 interacts with a conserved element in serotonergic genes. J Neurosci 19, 10348-
1581 10356.
1582 Hendricks, T.J., Fyodorov, D.V., Wegman, L.J., Lelutiu, N.B., Pehek, E.A., Yamamoto, B.,
1583 Silver, J., Weeber, E.J., Sweatt, J.D., and Deneris, E.S. (2003). Pet-1 ETS gene plays a
1584 critical role in 5-HT neuron development and is required for normal anxiety-like
1585 and aggressive behavior. Neuron 37, 233-247.
1586 Hennessy, M.L., Corcoran, A.E., Brust, R.D., Chang, Y., Nattie, E.E., and Dymecki, S.M.
1587 (2017). Activity of Tachykinin1-Expressing Pet1 Raphe Neurons Modulates the
1588 Respiratory Chemoreflex. J Neurosci 37, 1807-1819.
1589 Herzog, E., Gilchrist, J., Gras, C., Muzerelle, A., Ravassard, P., Giros, B., Gaspar, P., and
1590 El Mestikawy, S. (2004). Localization of VGLUT3, the vesicular glutamate
1591 transporter type 3, in the rat brain. Neuroscience 123, 983-1002.
1592 Hioki, H., Fujiyama, F., Nakamura, K., Wu, S.X., Matsuda, W., and Kaneko, T. (2004).
1593 Chemically specific circuit composed of vesicular glutamate transporter 3- and
1594 preprotachykinin B-producing interneurons in the rat neocortex. Cereb Cortex 14,
1595 1266-1275.
1596 Hioki, H., Nakamura, H., Ma, Y.F., Konno, M., Hayakawa, T., Nakamura, K.C., Fujiyama,
1597 F., and Kaneko, T. (2010). Vesicular glutamate transporter 3-expressing
1598 nonserotonergic projection neurons constitute a subregion in the rat midbrain
1599 raphe nuclei. J Comp Neurol 518, 668-686.
1600 Hitoshi, S., Maruta, N., Higashi, M., Kumar, A., Kato, N., and Ikenaka, K. (2007).
1601 Antidepressant drugs reverse the loss of adult neural stem cells following chronic
1602 stress. J Neurosci Res 85, 3574-3585.
1603 Hodge, R.D., Bakken, T.E., Miller, J.A., Smith, K.A., Barkan, E.R., Graybuck, L.T., Close,
1604 J.L., Long, B., Johansen, N., Penn, O.*, et al.* (2019). Conserved cell types with divergent
1605 features in human versus mouse cortex. Nature 573, 61-68.
1606 Hoffman, B.J., Mezey, E., and Brownstein, M.J. (1991). Cloning of a serotonin
1607 transporter affected by antidepressants. Science 254, 579-580.
1608 Huang, K.W., Ochandarena, N.E., Philson, A.C., Hyun, M., Birnbaum, J.E., Cicconet, M.,
1609 and Sabatini, B.L. (2019). Molecular and anatomical organization of the dorsal raphe
1610 nucleus. Elife 8.
1611 Ishimura, K., Takeuchi, Y., Fujiwara, K., Tominaga, M., Yoshioka, H., and Sawada, T.
1612 (1988). Quantitative analysis of the distribution of serotonin-immunoreactive cell
1613 bodies in the mouse brain. Neurosci Lett 91, 265-270.

1614 Iyer, A., Kmiecik, T.E., Park, M., Daar, I., Blair, D., Dunn, K.J., Sutrave, P., Ihle, J.N.,
1615 Bodescot, M., and Vande Woude, G.F. (1990). Structure, tissue-specific expression,
1616 and transforming activity of the mouse met protooncogene. Cell Growth Differ 1, 87-
1617 95.
1618 Jacobs, B.L., and Azmitia, E.C. (1992). Structure and function of the brain serotonin
1619 system. Physiol Rev 72, 165-229.
1620 Jensen, P., Farago, A.F., Awatramani, R.B., Scott, M.M., Deneris, E.S., and Dymecki, S.M.
1621 (2008). Redefining the serotonergic system by genetic lineage. Nat Neurosci 11,
1622 417-419.
1623 Ji, X., Wang, H., Zhu, M., He, Y., Zhang, H., Chen, X., Gao, W., Fu, Y., and Alzheimer's
1624 Disease Neuroimaging, I. (2020). Brainstem atrophy in the early stage of
1625 Alzheimer's disease: a voxel-based morphometry study. Brain Imaging Behav.
1626 Johnson, M.D. (1994). Synaptic glutamate release by postnatal rat serotonergic
1627 neurons in microculture. Neuron 12, 433-442.
1628 Joyner, A.L., Kornberg, T., Coleman, K.G., Cox, D.R., and Martin, G.R. (1985).
1629 Expression during embryogenesis of a mouse gene with sequence homology to the
1630 Drosophila engrailed gene. Cell 43, 29-37.
1631 Joyner, A.L., and Martin, G.R. (1987). En-1 and En-2, two mouse genes with sequence
1632 homology to the Drosophila engrailed gene: expression during embryogenesis.
1633 Genes Dev 1, 29-38.
1634 Judge, S.J., Ingram, C.D., and Gartside, S.E. (2004). Moderate differences in circulating
1635 corticosterone alter receptor-mediated regulation of 5-hydroxytryptamine neuronal
1636 activity. J Psychopharmacol 18, 475-483.
1637 Kapoor, V., Provost, A.C., Agarwal, P., and Murthy, V.N. (2016). Activation of raphe
1638 nuclei triggers rapid and distinct effects on parallel olfactory bulb output channels.
1639 Nat Neurosci 19, 271-282.
1640 Kast, R.J., Wu, H.H., Williams, P., Gaspar, P., and Levitt, P. (2017). Specific
1641 Connectivity and Unique Molecular Identity of MET Receptor Tyrosine Kinase
1642 Expressing Serotonergic Neurons in the Caudal Dorsal Raphe Nuclei. ACS Chem
1643 Neurosci 8, 1053-1064.
1644 Kim, J.C., Cook, M.N., Carey, M.R., Shen, C., Regehr, W.G., and Dymecki, S.M. (2009).
1645 Linking genetically defined neurons to behavior through a broadly applicable
1646 silencing allele. Neuron 63, 305-315.
1647 Kimmel, R.A., Turnbull, D.H., Blanquet, V., Wurst, W., Loomis, C.A., and Joyner, A.L.
1648 (2000). Two lineage boundaries coordinate vertebrate apical ectodermal ridge
1649 formation. Genes Dev 14, 1377-1389.
1650 Kirby, L.G., Pernar, L., Valentino, R.J., and Beck, S.G. (2003). Distinguishing
1651 characteristics of serotonin and non-serotonin-containing cells in the dorsal raphe
1652 nucleus: electrophysiological and immunohistochemical studies. Neuroscience 116,
1653 669-683.
1654 Kosofsky, B.E., and Molliver, M.E. (1987). The serotoninergic innervation of cerebral
1655 cortex: different classes of axon terminals arise from dorsal and median raphe
1656 nuclei. Synapse 1, 153-168.
1657 Krueger, K.C., and Deneris, E.S. (2008). Serotonergic transcription of human FEV
1658 reveals direct GATA factor interactions and fate of Pet-1-deficient serotonin neuron
1659 precursors. J Neurosci 28, 12748-12758.

1660 Laaris, N., Haj-Dahmane, S., Hamon, M., and Lanfumey, L. (1995). Glucocorticoid
1661 receptor-mediated inhibition by corticosterone of 5-HT1A autoreceptor functioning
1662 in the rat dorsal raphe nucleus. Neuropharmacology 34, 1201-1210.
1663 Land, B.B., Bruchas, M.R., Lemos, J.C., Xu, M., Melief, E.J., and Chavkin, C. (2008). The
1664 dysphoric component of stress is encoded by activation of the dynorphin kappa-
1665 opioid system. J Neurosci 28, 407-414.
1666 Land, B.B., Bruchas, M.R., Schattauer, S., Giardino, W.J., Aita, M., Messinger, D.,
1667 Hnasko, T.S., Palmiter, R.D., and Chavkin, C. (2009). Activation of the kappa opioid
1668 receptor in the dorsal raphe nucleus mediates the aversive effects of stress and
1669 reinstates drug seeking. Proc Natl Acad Sci U S A 106, 19168-19173.
1670 Lazaro-Pena, M.I., Diaz-Balzac, C.A., Bulow, H.E., and Emmons, S.W. (2018).
1671 Synaptogenesis Is Modulated by Heparan Sulfate in Caenorhabditis elegans.
1672 Genetics 209, 195-208.
1673 Lesch, K.P., Wolozin, B.L., Estler, H.C., Murphy, D.L., and Riederer, P. (1993). Isolation
1674 of a cDNA encoding the human brain serotonin transporter. J Neural Transm Gen
1675 Sect 91, 67-72.
1676 Levine, E.S., and Jacobs, B.L. (1992). Neurochemical afferents controlling the activity
1677 of serotonergic neurons in the dorsal raphe nucleus: microiontophoretic studies in
1678 the awake cat. J Neurosci 12, 4037-4044.
1679 Lidov, H.G., Grzanna, R., and Molliver, M.E. (1980). The serotonin innervation of the
1680 cerebral cortex in the rat--an immunohistochemical analysis. Neuroscience 5, 207-
1681 227.
1682 Lidov, H.G., and Molliver, M.E. (1982). Immunohistochemical study of the
1683 development of serotonergic neurons in the rat CNS. Brain Res Bull 9, 559-604.
1684 Lin, J.H., Takano, T., Arcuino, G., Wang, X., Hu, F., Darzynkiewicz, Z., Nunes, M.,
1685 Goldman, S.A., and Nedergaard, M. (2007). Purinergic signaling regulates neural
1686 progenitor cell expansion and neurogenesis. Dev Biol 302, 356-366.
1687 Liu, C., and Deneris, E.S. (2011). Transcriptional control of serotonin-modulated
1688 behavior and physiology. Neuropsychopharmacology 36, 361-362.
1689 Liu, C., Maejima, T., Wyler, S.C., Casadesus, G., Herlitze, S., and Deneris, E.S. (2010).
1690 Pet-1 is required across different stages of life to regulate serotonergic function. Nat
1691 Neurosci 13, 1190-1198.
1692 Liu, Z., Zhou, J., Li, Y., Hu, F., Lu, Y., Ma, M., Feng, Q., Zhang, J.E., Wang, D., Zeng, J., *et al.*
1693 (2014). Dorsal raphe neurons signal reward through 5-HT and glutamate. Neuron
1694 81, 1360-1374.
1695 Lorez, H.P., and Richards, J.G. (1982). Supra-ependymal serotoninergic nerves in
1696 mammalian brain: morphological, pharmacological and functional studies. Brain Res
1697 Bull 9, 727-741.
1698 Lovatt, D., Ruble, B.K., Lee, J., Dueck, H., Kim, T.K., Fisher, S., Francis, C., Spaethling,
1699 J.M., Wolf, J.A., Grady, M.S., *et al.* (2014). Transcriptome in vivo analysis (TIVA) of
1700 spatially defined single cells in live tissue. Nat Methods 11, 190-196.
1701 Love, C.E., and Prince, V.E. (2012). Expression and retinoic acid regulation of the
1702 zebrafish nr2f orphan nuclear receptor genes. Dev Dyn 241, 1603-1615.
1703 Luo, J., Feng, Q., Wei, L., and Luo, M. (2017). Optogenetic activation of dorsal raphe
1704 neurons rescues the autistic-like social deficits in Shank3 knockout mice. Cell Res
1705 27, 950-953.

1706 Macosko, E.Z., Basu, A., Satija, R., Nemesh, J., Shekhar, K., Goldman, M., Tirosh, I.,
1707 Bialas, A.R., Kamitaki, N., Martersteck, E.M., *et al.* (2015). Highly Parallel Genome-
1708 wide Expression Profiling of Individual Cells Using Nanoliter Droplets. Cell 161,
1709 1202-1214.
1710 Maddaloni, G., Bertero, A., Pratelli, M., Barsotti, N., Boonstra, A., Giorgi, A., Migliarini,
1711 S., and Pasqualetti, M. (2017). Development of Serotonergic Fibers in the Post-Natal
1712 Mouse Brain. Front Cell Neurosci 11, 202.
1713 Madisen, L., Garner, A.R., Shimaoka, D., Chuong, A.S., Klapoetke, N.C., Li, L., van der
1714 Bourg, A., Niino, Y., Egolf, L., Monetti, C., *et al.* (2015). Transgenic mice for
1715 intersectional targeting of neural sensors and effectors with high specificity and
1716 performance. Neuron 85, 942-958.
1717 Makrides, N., Panayiotou, E., Fanis, P., Karaiskos, C., Lapathitis, G., and Malas, S.
1718 (2018). Sequential Role of SOXB2 Factors in GABAergic Neuron Specification of the
1719 Dorsal Midbrain. Front Mol Neurosci 11, 152.
1720 McDevitt, R.A., Tiran-Cappello, A., Shen, H., Balderas, I., Britt, J.P., Marino, R.A.,
1721 Chung, S.L., Richie, C.T., Harvey, B.K., and Bonci, A. (2014). Serotonergic versus
1722 nonserotonergic dorsal raphe projection neurons: differential participation in
1723 reward circuitry. Cell Rep 8, 1857-1869.
1724 Michaelson, J.J., Shin, M.K., Koh, J.Y., Brueggeman, L., Zhang, A., Katzman, A.,
1725 McDaniel, L., Fang, M., Pufall, M., and Pieper, A.A. (2017). Neuronal PAS Domain
1726 Proteins 1 and 3 Are Master Regulators of Neuropsychiatric Risk Genes. Biol
1727 Psychiatry 82, 213-223.
1728 Michelsen, K.A., Prickaerts, J., and Steinbusch, H.W. (2008). The dorsal raphe nucleus
1729 and serotonin: implications for neuroplasticity linked to major depression and
1730 Alzheimer's disease. Prog Brain Res 172, 233-264.
1731 Michelsen, K.A., Schmitz, C., and Steinbusch, H.W. (2007). The dorsal raphe nucleus--
1732 from silver stainings to a role in depression. Brain Res Rev 55, 329-342.
1733 Mikkelsen, J.D., Hay-Schmidt, A., and Larsen, P.J. (1997). Central innervation of the
1734 rat ependyma and subcommissural organ with special reference to ascending
1735 serotoninergic projections from the raphe nuclei. J Comp Neurol 384, 556-568.
1736 Minge, D., Senkov, O., Kaushik, R., Herde, M.K., Tikhobrazova, O., Wulff, A.B., Mironov,
1737 A., van Kuppevelt, T.H., Oosterhof, A., Kochlamazashvili, G., *et al.* (2017). Heparan
1738 Sulfates Support Pyramidal Cell Excitability, Synaptic Plasticity, and Context
1739 Discrimination. Cereb Cortex 27, 903-918.
1740 Mirzadeh, Z., Doetsch, F., Sawamoto, K., Wichterle, H., and Alvarez-Buylla, A. (2010).
1741 The subventricular zone en-face: wholemount staining and ependymal flow. J Vis
1742 Exp.
1743 Miyazaki, K., Narita, N., and Narita, M. (2005). Maternal administration of
1744 thalidomide or valproic acid causes abnormal serotonergic neurons in the offspring:
1745 implication for pathogenesis of autism. Int J Dev Neurosci 23, 287-297.
1746 Molliver, M.E. (1987). Serotonergic neuronal systems: what their anatomic
1747 organization tells us about function. J Clin Psychopharmacol 7, 3S-23S.
1748 Mosko, S.S., Haubrich, D., and Jacobs, B.L. (1977). Serotonergic afferents to the
1749 dorsal raphe nucleus: evdience from HRP and synaptosomal uptake studies. Brain
1750 Res 119, 269-290.

1751 Munster-Wandowski, A., Zander, J.F., Richter, K., and Ahnert-Hilger, G. (2016). Co-
1752 existence of Functionally Different Vesicular Neurotransmitter Transporters. Front
1753 Synaptic Neurosci 8, 4.
1754 Muzerelle, A., Scotto-Lomassese, S., Bernard, J.F., Soiza-Reilly, M., and Gaspar, P.
1755 (2016). Conditional anterograde tracing reveals distinct targeting of individual
1756 serotonin cell groups (B5-B9) to the forebrain and brainstem. Brain Struct Funct
1757 221, 535-561.
1758 Negoias, S., Croy, I., Gerber, J., Puschmann, S., Petrowski, K., Joraschky, P., and
1759 Hummel, T. (2010). Reduced olfactory bulb volume and olfactory sensitivity in
1760 patients with acute major depression. Neuroscience 169, 415-421.
1761 Niederkofler, V., Asher, T.E., Okaty, B.W., Rood, B.D., Narayan, A., Hwa, L.S., Beck, S.G.,
1762 Miczek, K.A., and Dymecki, S.M. (2016). Identification of Serotonergic Neuronal
1763 Modules that Affect Aggressive Behavior. Cell Rep 17, 1934-1949.
1764 Nyberg, J., Anderson, M.F., Meister, B., Alborn, A.M., Strom, A.K., Brederlau, A.,
1765 Illerskog, A.C., Nilsson, O., Kieffer, T.J., Hietala, M.A.*, et al.* (2005). Glucose-dependent
1766 insulinotropic polypeptide is expressed in adult hippocampus and induces
1767 progenitor cell proliferation. J Neurosci 25, 1816-1825.
1768 O'Hearn, E., and Molliver, M.E. (1984). Organization of raphe-cortical projections in
1769 rat: a quantitative retrograde study. Brain Res Bull 13, 709-726.
1770 Ogawa, S.K., Cohen, J.Y., Hwang, D., Uchida, N., and Watabe-Uchida, M. (2014).
1771 Organization of monosynaptic inputs to the serotonin and dopamine
1772 neuromodulatory systems. Cell Rep 8, 1105-1118.
1773 Okaty, B.W., Commons, K.G., and Dymecki, S.M. (2019). Embracing diversity in the 5-
1774 HT neuronal system. Nat Rev Neurosci.
1775 Okaty, B.W., Freret, M.E., Rood, B.D., Brust, R.D., Hennessy, M.L., deBairos, D., Kim,
1776 J.C., Cook, M.N., and Dymecki, S.M. (2015). Multi-Scale Molecular Deconstruction of
1777 the Serotonin Neuron System. Neuron 88, 774-791.
1778 Pelosi, B., Migliarini, S., Pacini, G., Pratelli, M., and Pasqualetti, M. (2014). Generation
1779 of Pet1210-Cre transgenic mouse line reveals non-serotonergic expression domains
1780 of Pet1 both in CNS and periphery. PLoS One 9, e104318.
1781 Peyron, C., Petit, J.M., Rampon, C., Jouvet, M., and Luppi, P.H. (1998). Forebrain
1782 afferents to the rat dorsal raphe nucleus demonstrated by retrograde and
1783 anterograde tracing methods. Neuroscience 82, 443-468.
1784 Peyron, C., Rampon, C., Petit, J.M., and Luppi, P.H. (2018). Sub-regions of the dorsal
1785 raphe nucleus receive different inputs from the brainstem. Sleep Med 49, 53-63.
1786 Pillai, A., Mansouri, A., Behringer, R., Westphal, H., and Goulding, M. (2007). Lhx1
1787 and Lhx5 maintain the inhibitory-neurotransmitter status of interneurons in the
1788 dorsal spinal cord. Development 134, 357-366.
1789 Pollak Dorocic, I., Furth, D., Xuan, Y., Johansson, Y., Pozzi, L., Silberberg, G., Carlen, M.,
1790 and Meletis, K. (2014). A whole-brain atlas of inputs to serotonergic neurons of the
1791 dorsal and median raphe nuclei. Neuron 83, 663-678.
1792 Poulin, J.F., Tasic, B., Hjerling-Leffler, J., Trimarchi, J.M., and Awatramani, R. (2016).
1793 Disentangling neural cell diversity using single-cell transcriptomics. Nat Neurosci
1794 19, 1131-1141.

1795 Prakash, N., Stark, C.J., Keisler, M.N., Luo, L., Der-Avakian, A., and Dulcis, D. (2019).
1796 Serotonergic plasticity in the dorsal raphe nucleus characterizes susceptibility and
1797 resilience to anhedonia. J Neurosci.
1798 Prouty, E.W., Chandler, D.J., and Waterhouse, B.D. (2017). Neurochemical differences
1799 betweentarget-specific populations of rat dorsal raphe projection neurons. Brain
1800 Res.
1801 Ray, R.S., Corcoran, A.E., Brust, R.D., Kim, J.C., Richerson, G.B., Nattie, E., and Dymecki,
1802 S.M. (2011). Impaired respiratory and body temperature control upon acute
1803 serotonergic neuron inhibition. Science 333, 637-642.
1804 Ren, J., Friedmann, D., Xiong, J., Liu, C.D., Ferguson, B.R., Weerakkody, T., DeLoach,
1805 K.E., Ran, C., Pun, A., Sun, Y.*, et al.* (2018). Anatomically Defined and Functionally
1806 Distinct Dorsal Raphe Serotonin Sub-systems. Cell 175, 472-487 e420.
1807 Ren, J., Isakova, A., Friedmann, D., Zeng, J., Grutzner, S.M., Pun, A., Zhao, G.Q., Kolluru,
1808 S.S., Wang, R., Lin, R.*, et al.* (2019). Single-cell transcriptomes and whole-brain
1809 projections of serotonin neurons in the mouse dorsal and median raphe nuclei. Elife
1810 8.
1811 Rood, B.D., Calizo, L.H., Piel, D., Spangler, Z.P., Campbell, K., and Beck, S.G. (2014).
1812 Dorsal raphe serotonin neurons in mice: immature hyperexcitability transitions to
1813 adult state during first three postnatal weeks suggesting sensitive period for
1814 environmental perturbation. J Neurosci 34, 4809-4821.
1815 Rosenberg, A.B., Roco, C.M., Muscat, R.A., Kuchina, A., Sample, P., Yao, Z., Graybuck,
1816 L.T., Peeler, D.J., Mukherjee, S., Chen, W.*, et al.* (2018). Single-cell profiling of the
1817 developing mouse brain and spinal cord with split-pool barcoding. Science 360, 176-
1818 182.
1819 Saunders, A., Macosko, E.Z., Wysoker, A., Goldman, M., Krienen, F.M., de Rivera, H.,
1820 Bien, E., Baum, M., Bortolin, L., Wang, S.*, et al.* (2018). Molecular Diversity and
1821 Specializations among the Cells of the Adult Mouse Brain. Cell 174, 1015-1030
1822 e1016.
1823 Sciolino, N.R., Plummer, N.W., Chen, Y.W., Alexander, G.M., Robertson, S.D., Dudek,
1824 S.M., McElligott, Z.A., and Jensen, P. (2016). Recombinase-Dependent Mouse Lines
1825 for Chemogenetic Activation of Genetically Defined Cell Types. Cell Rep 15, 2563-
1826 2573.
1827 Sengupta, A., Bocchio, M., Bannerman, D.M., Sharp, T., and Capogna, M. (2017).
1828 Control of Amygdala Circuits by 5-HT Neurons via 5-HT and Glutamate
1829 Cotransmission. J Neurosci 37, 1785-1796.
1830 Shikanai, H., Yoshida, T., Konno, K., Yamasaki, M., Izumi, T., Ohmura, Y., Watanabe,
1831 M., and Yoshioka, M. (2012). Distinct neurochemical and functional properties of
1832 GAD67-containing 5-HT neurons in the rat dorsal raphe nucleus. J Neurosci 32,
1833 14415-14426.
1834 Simic, G., Babic Leko, M., Wray, S., Harrington, C.R., Delalle, I., Jovanov-Milosevic, N.,
1835 Bazadona, D., Buee, L., de Silva, R., Di Giovanni, G.*, et al.* (2017). Monoaminergic
1836 neuropathology in Alzheimer's disease. Prog Neurobiol 151, 101-138.
1837 Siopi, E., Denizet, M., Gabellec, M.M., de Chaumont, F., Olivo-Marin, J.C., Guilloux, J.P.,
1838 Lledo, P.M., and Lazarini, F. (2016). Anxiety- and Depression-Like States Lead to
1839 Pronounced Olfactory Deficits and Impaired Adult Neurogenesis in Mice. J Neurosci
1840 36, 518-531.

1841 Soghomonian, J.J., and Martin, D.L. (1998). Two isoforms of glutamate
1842 decarboxylase: why? Trends Pharmacol Sci 19, 500-505.
1843 Sos, K.E., Mayer, M.I., Cserep, C., Takacs, F.S., Szonyi, A., Freund, T.F., and Nyiri, G.
1844 (2017). Cellular architecture and transmitter phenotypes of neurons of the mouse
1845 median raphe region. Brain Struct Funct 222, 287-299.
1846 Soumier, A., Banasr, M., Kerkerian-Le Goff, L., and Daszuta, A. (2010). Region- and
1847 phase-dependent effects of 5-HT(1A) and 5-HT(2C) receptor activation on adult
1848 neurogenesis. Eur Neuropsychopharmacol 20, 336-345.
1849 Spaethling, J.M., Piel, D., Dueck, H., Buckley, P.T., Morris, J.F., Fisher, S.A., Lee, J., Sul,
1850 J.Y., Kim, J., Bartfai, T.*, et al.* (2014). Serotonergic neuron regulation informed by in
1851 vivo single-cell transcriptomics. FASEB J 28, 771-780.
1852 Spencer, W.C., and Deneris, E.S. (2017). Regulatory Mechanisms Controlling
1853 Maturation of Serotonin Neuron Identity and Function. Front Cell Neurosci 11, 215.
1854 Stanco, A., Pla, R., Vogt, D., Chen, Y., Mandal, S., Walker, J., Hunt, R.F., Lindtner, S.,
1855 Erdman, C.A., Pieper, A.A.*, et al.* (2014). NPAS1 represses the generation of specific
1856 subtypes of cortical interneurons. Neuron 84, 940-953.
1857 Steinbusch, H.W. (1981). Distribution of serotonin-immunoreactivity in the central
1858 nervous system of the rat-cell bodies and terminals. Neuroscience 6, 557-618.
1859 Steinbusch, H.W., van der Kooy, D., Verhofstad, A.A., and Pellegrino, A. (1980).
1860 Serotonergic and non-serotonergic projections from the nucleus raphe dorsalis to
1861 the caudate-putamen complex in the rat, studied by a combined
1862 immunofluorescence and fluorescent retrograde axonal labeling technique.
1863 Neurosci Lett 19, 137-142.
1864 Steinbusch, H.W., Verhofstad, A.A., and Joosten, H.W. (1978). Localization of
1865 serotonin in the central nervous system by immunohistochemistry: description of a
1866 specific and sensitive technique and some applications. Neuroscience 3, 811-819.
1867 Stuart, T., Butler, A., Hoffman, P., Hafemeister, C., Papalexi, E., Mauck, W.M., 3rd, Hao,
1868 Y., Stoeckius, M., Smibert, P., and Satija, R. (2019). Comprehensive Integration of
1869 Single-Cell Data. Cell 177, 1888-1902 e1821.
1870 Tasic, B. (2018). Single cell transcriptomics in neuroscience: cell classification and
1871 beyond. Curr Opin Neurobiol 50, 242-249.
1872 Tasic, B., Menon, V., Nguyen, T.N., Kim, T.K., Jarsky, T., Yao, Z., Levi, B., Gray, L.T.,
1873 Sorensen, S.A., Dolbeare, T.*, et al.* (2016). Adult mouse cortical cell taxonomy
1874 revealed by single cell transcriptomics. Nat Neurosci 19, 335-346.
1875 Tasic, B., Yao, Z., Graybuck, L.T., Smith, K.A., Nguyen, T.N., Bertagnolli, D., Goldy, J.,
1876 Garren, E., Economo, M.N., Viswanathan, S.*, et al.* (2018). Shared and distinct
1877 transcriptomic cell types across neocortical areas. Nature 563, 72-78.
1878 Teissier, A., Chemiakine, A., Inbar, B., Bagchi, S., Ray, R.S., Palmiter, R.D., Dymecki,
1879 S.M., Moore, H., and Ansorge, M.S. (2015). Activity of Raphe Serotonergic Neurons
1880 Controls Emotional Behaviors. Cell Rep 13, 1965-1976.
1881 Teng, T., Gaillard, A., Muzerelle, A., and Gaspar, P. (2017). EphrinA5 Signaling Is
1882 Required for the Distinctive Targeting of Raphe Serotonin Neurons in the Forebrain.
1883 eNeuro 4.
1884 Tong, C.K., Chen, J., Cebrian-Silla, A., Mirzadeh, Z., Obernier, K., Guinto, C.D., Tecott,
1885 L.H., Garcia-Verdugo, J.M., Kriegstein, A., and Alvarez-Buylla, A. (2014). Axonal
1886 control of the adult neural stem cell niche. Cell Stem Cell 14, 500-511.

1887 Tritsch, N.X., Ding, J.B., and Sabatini, B.L. (2012). Dopaminergic neurons inhibit
1888 striatal output through non-canonical release of GABA. Nature 490, 262-266.
1889 Trivellin, G., Bjelobaba, I., Daly, A.F., Larco, D.O., Palmeira, L., Faucz, F.R., Thiry, A.,
1890 Leal, L.F., Rostomyan, L., Quezado, M., *et al.* (2016). Characterization of GPR101
1891 transcript structure and expression patterns. J Mol Endocrinol 57, 97-111.
1892 Trivellin, G., Hernandez-Ramirez, L.C., Swan, J., and Stratakis, C.A. (2018). An orphan
1893 G-protein-coupled receptor causes human gigantism and/or acromegaly: Molecular
1894 biology and clinical correlations. Best Pract Res Clin Endocrinol Metab 32, 125-140.
1895 Usoskin, D., Furlan, A., Islam, S., Abdo, H., Lonnerberg, P., Lou, D., Hjerling-Leffler, J.,
1896 Haeggstrom, J., Kharchenko, O., Kharchenko, P.V., *et al.* (2015). Unbiased
1897 classification of sensory neuron types by large-scale single-cell RNA sequencing. Nat
1898 Neurosci 18, 145-153.
1899 Vakalopoulos, C. (2017). Alzheimer's Disease: The Alternative Serotonergic
1900 Hypothesis of Cognitive Decline. J Alzheimers Dis 60, 859-866.
1901 Vasudeva, R.K., Lin, R.C., Simpson, K.L., and Waterhouse, B.D. (2011). Functional
1902 organization of the dorsal raphe efferent system with special consideration of
1903 nitrergic cell groups. J Chem Neuroanat 41, 281-293.
1904 Vasudeva, R.K., and Waterhouse, B.D. (2014). Cellular profile of the dorsal raphe
1905 lateral wing sub-region: relationship to the lateral dorsal tegmental nucleus. J Chem
1906 Neuroanat 57-58, 15-23.
1907 Vertes, R.P. (1991). A PHA-L analysis of ascending projections of the dorsal raphe
1908 nucleus in the rat. J Comp Neurol 313, 643-668.
1909 Vertes, R.P., and Kocsis, B. (1994). Projections of the dorsal raphe nucleus to the
1910 brainstem: PHA-L analysis in the rat. J Comp Neurol 340, 11-26.
1911 Vincent, M.Y., Donner, N.C., Smith, D.G., Lowry, C.A., and Jacobson, L. (2018). Dorsal
1912 raphe nucleus glucocorticoid receptors inhibit tph2 gene expression in male
1913 C57BL/6J mice. Neurosci Lett 665, 48-53.
1914 Vincent, M.Y., and Jacobson, L. (2014). Glucocorticoid receptor deletion from the
1915 dorsal raphe nucleus of mice reduces dysphoria-like behavior and impairs
1916 hypothalamic-pituitary-adrenocortical axis feedback inhibition. Eur J Neurosci 39,
1917 1671-1681.
1918 Voisin, A.N., Mnie-Filali, O., Giguere, N., Fortin, G.M., Vigneault, E., El Mestikawy, S.,
1919 Descarries, L., and Trudeau, L.E. (2016). Axonal Segregation and Role of the
1920 Vesicular Glutamate Transporter VGLUT3 in Serotonin Neurons. Front Neuroanat
1921 10, 39.
1922 Walther, D.J., and Bader, M. (2003). A unique central tryptophan hydroxylase
1923 isoform. Biochem Pharmacol 66, 1673-1680.
1924 Walther, D.J., Peter, J.U., Bashammakh, S., Hortnagl, H., Voits, M., Fink, H., and Bader,
1925 M. (2003). Synthesis of serotonin by a second tryptophan hydroxylase isoform.
1926 Science 299, 76.
1927 Wang, H.L., Zhang, S., Qi, J., Wang, H., Cachope, R., Mejias-Aponte, C.A., Gomez, J.A.,
1928 Mateo-Semidey, G.E., Beaudoin, G.M.J., Paladini, C.A., *et al.* (2019). Dorsal Raphe Dual
1929 Serotonin-Glutamate Neurons Drive Reward by Establishing Excitatory Synapses on
1930 VTA Mesoaccumbens Dopamine Neurons. Cell Rep 26, 1128-1142 e1127.

1931 Wang, R., Hausknecht, K., Shen, R.Y., and Haj-Dahmane, S. (2018). Potentiation of
1932 Glutamatergic Synaptic Transmission Onto Dorsal Raphe Serotonergic Neurons in
1933 the Valproic Acid Model of Autism. Front Pharmacol 9, 1185.
1934 Watanabe, M., Serizawa, M., Sawada, T., Takeda, K., Takahashi, T., Yamamoto, N.,
1935 Koizumi, F., and Koh, Y. (2014). A novel flow cytometry-based cell capture platform
1936 for the detection, capture and molecular characterization of rare tumor cells in
1937 blood. J Transl Med 12, 143.
1938 Weissbourd, B., Ren, J., DeLoach, K.E., Guenthner, C.J., Miyamichi, K., and Luo, L.
1939 (2014). Presynaptic partners of dorsal raphe serotonergic and GABAergic neurons.
1940 Neuron 83, 645-662.
1941 Wu, H.H., and Levitt, P. (2013). Prenatal expression of MET receptor tyrosine kinase
1942 in the fetal mouse dorsal raphe nuclei and the visceral motor/sensory brainstem.
1943 Dev Neurosci 35, 1-16.
1944 Wyler, S.C., Donovan, L.J., Yeager, M., and Deneris, E. (2015). Pet-1 Controls
1945 Tetrahydrobiopterin Pathway and Slc22a3 Transporter Genes in Serotonin Neurons.
1946 ACS Chem Neurosci 6, 1198-1205.
1947 Wyler, S.C., Spencer, W.C., Green, N.H., Rood, B.D., Crawford, L., Craige, C., Gresch, P.,
1948 McMahon, D.G., Beck, S.G., and Deneris, E. (2016). Pet-1 Switches Transcriptional
1949 Targets Postnatally to Regulate Maturation of Serotonin Neuron Excitability. J
1950 Neurosci 36, 1758-1774.
1951 Ye, W., Bouchard, M., Stone, D., Liu, X., Vella, F., Lee, J., Nakamura, H., Ang, S.L.,
1952 Busslinger, M., and Rosenthal, A. (2001). Distinct regulators control the expression
1953 of the mid-hindbrain organizer signal FGF8. Nat Neurosci 4, 1175-1181.
1954 Ye, Y., Zhao, Z., Xu, H., Zhang, X., Su, X., Yang, Y., Yu, X., and He, X. (2016). Activation of
1955 Sphingosine 1-Phosphate Receptor 1 Enhances Hippocampus Neurogenesis in a Rat
1956 Model of Traumatic Brain Injury: An Involvement of MEK/Erk Signaling Pathway.
1957 Neural Plast 2016, 8072156.
1958 Zeisel, A., Hochgerner, H., Lonnerberg, P., Johnsson, A., Memic, F., van der Zwan, J.,
1959 Haring, M., Braun, E., Borm, L.E., La Manno, G.*, et al.* (2018). Molecular Architecture
1960 of the Mouse Nervous System. Cell 174, 999-1014 e1022.
1961 Zeisel, A., Munoz-Manchado, A.B., Codeluppi, S., Lonnerberg, P., La Manno, G., Jureus,
1962 A., Marques, S., Munguba, H., He, L., Betsholtz, C.*, et al.* (2015). Brain structure. Cell
1963 types in the mouse cortex and hippocampus revealed by single-cell RNA-seq.
1964 Science 347, 1138-1142.
1965 Zhang, P., Lu, H., Peixoto, R.T., Pines, M.K., Ge, Y., Oku, S., Siddiqui, T.J., Xie, Y., Wu, W.,
1966 Archer-Hartmann, S.*, et al.* (2018). Heparan Sulfate Organizes Neuronal Synapses
1967 through Neurexin Partnerships. Cell 174, 1450-1464 e1423.
1968 Zweig, R.M., Ross, C.A., Hedreen, J.C., Steele, C., Cardillo, J.E., Whitehouse, P.J.,
1969 Folstein, M.F., and Price, D.L. (1988). The neuropathology of aminergic nuclei in
1970 Alzheimer's disease. Ann Neurol 24, 233-242.

1971

1972 **Figure Legends**

1973 Figure 1: High throughput scRNA-seq and clustering analyses reveal as many as
1974 fourteen distinct molecularly-defined subtypes (clusters) of *Pet1* neurons in the mouse
1975 DR. (A) Schematic depicting the experimental and analytical workflow, specifically: (1)
1976 brain dissection and DR microdissection, (2) cellular dissociation and microfluidic
1977 fluorescence-based cell sorting using the On-chip Sort, and (3) library preparation,
1978 sequencing, and analysis using 10X genomics, Illumina sequencing, and the R package
1979 Seurat, respectively. (B) Hierarchical clustering of *Pet1* neuron subtypes identified by
1980 Louvain clustering (using the top two thousand genes with the highest variance, PCs =
1981 1:5, 8:50, and resolution=0.9), with violin plots depicting the log-normalized expression
1982 of a common set of genes (*Tph2, Gad2, Gad1, Vglut3,* and *Met*) found useful for
1983 characterizing cluster structure across multiple resolutions (see Figure 1- figure
1984 supplement 2). (C) UMAP visualization of single-neuron transcriptome
1985 community/similarity structure, with colors and numbers indicating discrete clusters
1986 (same clustering parameters as (B)). (D) Heatmap depicting the scaled expression of the
1987 top five marker genes for each cluster (ranked by p-value, or in some cases fold
1988 enrichment).

1989 Figure 1 - figure supplement 1: Systematic variation of key clustering parameters allows
1990 for exploration of the community structure of DR *Pet1* single neuron transcriptomes at
1991 variable resolutions. (A) Scatterplot of the variance (standard deviation, Y-axis)
1992 explained by the first 250 principal components (X-axis). (B) Heat map depicting the
1993 number of clusters (DR *Pet1* neuron subtypes) resulting from variation of the number of
1994 included principle components (Y-axis) and the resolution parameter to the Seurat
1995 function FindClusters (X-axis). (C) Line graph of the frequency (Y-axis) that a given
1996 number of clusters (X-axis) arises from the analysis performed in B. (D) Plots showing
1997 the parameters (white) that lead to cluster numbers found to have the highest frequency
1998 (5, 11, 14, and 17 clusters, top left to bottom right respectively).

1999 Figure 1 - figure supplement 2: Analysis of clusters at successively increasing resolution
2000 values. (A, D, G) Hierarchical clustering of *Pet1* neuron subtypes identified by Louvain
2001 clustering at varying resolutions (specifically, the resolution value passed to the Seurat
2002 function FindClusters A= 0.1, D= 0.3, G= 0.7), and violin plots depicting the normalized
2003 expression of *Tph2, Gad2, Gad1, Vglut3,* and *Met.* (B, E, H) UMAP visualization of
2004 community structure at a given resolution (B= 0.1, E= 0.3, H= 0.7). (C, F, I) Heatmap

2005 depicting the scaled expression of the top five marker genes for each cluster (ranked by
2006 p-value).

2007 Figure 1 - figure supplement 3: Expression of serotonin-related genes across DR *Pet1*
2008 neuron subtypes. Violin plots depicting the log-normalized expression of serotonin
2009 neuron marker genes across the fourteen *Pet1* neuron clusters.

2010 Figure 1 – figure supplement 4: Correlation of 5-HT marker gene expression levels with
2011 *Fev* (*Pet1*) gene expression levels for clusters 13 and 14. Scatter plots showing the
2012 correlation between the normalized expression level of *Pet1* (X-axis) and other 5-HT
2013 marker genes (Y-axis) for clusters thirteen (light pink open circles) and fourteen (dark
2014 pink closed circles). Linear line of best fit for each plot shown in black with corresponding
2015 95% confidence interval in grey. Pearson correlation coefficient and p value displayed in
2016 the top left corner of each graph.

2017 Figure 2: Expression patterns of a subset of highly variable genes classified by biological
2018 function. Dot plots show the expression of a gene (Y-axis) in each cluster (X-axis),
2019 separated by biological function. The size of the dot represents the percentage of cells
2020 expressing the gene and saturation of color represents average normalized expression
2021 level. For convenience, the UMAP plot from Figure 1C is re-displayed at the bottom right
2022 to help link gene expression patterns to overall cluster structure. Minimum inclusion
2023 criteria for genes was that they were among the top 2000 highest variance genes and/or
2024 they were found to be significantly enriched or "de-enriched" in at least one subtype
2025 cluster (see **Methods**).

2026 Figure 3: Intersectionally targeted *Pet1* neuron subtypes have different anatomical
2027 distributions in subregions of the DR. (A-E) Low magnification view of 40 μm coronal
2028 sections showing the DR from rostral to caudal (1-6) in triple transgenic animals. Cell
2029 bodies are labeled by the intersectional expression of a Cre driver of interest, *Pet1::Flpe*,
2030 and the intersectional allele *FrePe* (green EGFP marked cells expressing both Cre and
2031 Flpe and red mCherry expressing *Pet1::Flpe* subtractive population) unless otherwise
2032 noted. (A) *Sert::cre; Pet1::Flpe; FrePe*, (B) *Vglut3::cre; Pet1::Flpe; hM3Dq* (green
2033 mCherry-hM3Dq marked cells expressing Cre and Flpe and red EGFP expressing
2034 *Pet1::Flpe* subtractive population), (C) *Npy2r::IRES-cre; Pet1::Flpe; FrePe*, (D)
2035 *P2ry1::IRES-cre; Pet1::Flpe; FrePe*. Top row shows violin plots depicting transcript

2036 expression (10X scRNA-seq data) of the respective gene corresponding with each Cre
2037 driver. Scale bar (A1) equals 100 µm. The expression of TPH2 and VGLUT3 was further
2038 investigated in Figure 3 – figure supplement 1 and 2, respectively.

2039 Figure 3 – figure supplement 1: Diversity of *Tph2* RNA transcripts and protein
2040 expression in dorsal raphe *Pet1* neurons. (A) Bar graph showing the percentage of the
2041 total population of EGFP-positive TPH2-negative cells counted in a specific anatomical
2042 subdivision of the DR in *En1::cre;Pet1::Flpe;RC::FrePe* animals (Green labeled neurons
2043 with intersectional expression of *En1::cre* and *Pet1::Flpe)*. n=2, bar graph depicting the
2044 mean with SEM. (B, C) Images showing co-visualization of EGFP (green) and TPH2
2045 (magenta) by immunofluorescence and *Tph2* transcripts (red) by RNAscope in
2046 *En1::cre;Pet1::Flpe;FrePe* neurons. Examples for a TPH2 immunopositive cell with high
2047 *Tph2* transcripts (white arrow in B), a TPH2 immunonegative cell with low *Tph2*
2048 transcripts (orange arrow in B), and a TPH2 immunopositive cell with medium levels of
2049 *Tph2* transcript (red arrow in C) are shown. Scale bars are 10 µm. (D) Violin plot
2050 depicting the number of *Tph2* puncta per um^2 of each counted EGFP+ cell (from an
2051 *En1::cre;Pet1::Flpe; FrePe* animal) that was TPH2 immunopositive (black) or TPH2
2052 immunonegative (pink). The violin plot is split into deciles, with fill color representing the
2053 percent of TPH2 immunopositive cells within a given decile. (E) Box plots depicting the
2054 number of *Tph2* puncta for each counted EGFP+ cell that was TPH2 immunopositive
2055 (darker shade, left) or TPH2 immunonegative (lighter shade, right), split across DR
2056 subanatomy (Rostral and Caudal, dorsomedial DR (blue), medial DR (tan), ventromedial
2057 DR (green), dorsolateral DR (turquoise)). (F) and (G) same as D and E, except depicting
2058 cell area.

2059 Figure 3 - figure supplement 2: VGLUT3 antibody staining of *Pet1* neurons is
2060 anatomically biased within different DR subdomains. (A-F) Quantification of the
2061 percentage of VGLUT3 immunoreactive *Vglut3::cre; Pet1::Flpe* lineage (dark green) and
2062 VGLUT3 immunoreactive subtractive *Pet1* lineage cells (dark red) within anatomical
2063 subdivisions of the dorsal raphe from rostral (A) to caudal (F), in comparison to VGLUT3
2064 immunonegative *Vglut3*::cre;*Pet1::Flpe* and subtractive *Pet1* neurons (light green and
2065 light red respectively). Low magnification images indicate representative quantified
2066 images. Anatomical subdivisions (dorsomedial (dm), medial (m), ventromedial (vm) and
2067 dorsolateral (dl)) are delineated with white brackets. Scale bar in D equals 100 µm, n=2,
2068 bar graph depicts mean with SEM. (G) Summary coronal brainstem schematic showing

2069 the distribution of VGLUT3 immunopositive and immunonegative *Vglut3::cre; Pet1::Flpe*
2070 (dark and light green) and subtractive *Pet1* neurons (dark and light red) in the DR from
2071 rostral (left) to caudal (right).

2072 Figure 4: scRNA-seq of *Pet1* neurons manually sorted from anatomical subdomains map
2073 onto specific 10X scRNA-seq clusters. (A) Schematic of the pipeline used for manual
2074 sorting and sequencing, including referenced anatomical subdomains mapped onto
2075 representative images of the DR. *Pet1* neurons are in green. (B) Dot plot mapping
2076 manually sorted cells from a given genotype and anatomical subdomain (Y-axis) to the
2077 fourteen 10X clusters (X-axis). The size of the dot indicates the percentage of single
2078 cells from a genotype/anatomical region attributed to a reference cluster. Note, the
2079 asterisks after *Drd2::cre;Pet1::Flpe* is to denote that these data come from a previously
2080 published study (Niederkofler, et al. 2016), and these particular single-cell libraries were
2081 prepared using the Nugen Ovation RNA-seq System v2 kit, rather than SMART-Seq v4.
2082 The expression of a selection of highly variable and cluster marker genes is depicted in
2083 Figure 4- figure supplement 1.

2084 Figure 4 – figure supplement 1: Expression patterns of a selection of highly variable and
2085 cluster marker genes that show anatomical bias. Dot plot depicting the expression of
2086 genes (Y-axis) across manually sorted cells from a specific subdomain and genotype
2087 (left) and 10X scRNA-seq clusters (right). The size of the dot represents the percentage
2088 of cells expressing the gene and saturation of color represents the average normalized
2089 expression level. As with Figure 4, the asterisks after *Drd2::cre;Pet1::Flpe* denotes that
2090 these data come from a previously published study (Niederkofler, et al. 2016), and these
2091 particular single-cell libraries were prepared using the Nugen Ovation RNA-seq System
2092 v2 kit, rather than SMART-Seq v4.

2093 Figure 4 - figure supplement 2: PAX5 and SATB2 are expressed predominately in rostral
2094 dorsomedial and dorsolateral *Pet1* neurons while NR2F2 is expressed predominately in
2095 caudal *Pet1* neurons. (A) Representative regions of the DR used for quantification of
2096 immunostaining from rostral (left) to caudal (right). Brackets indicate anatomical
2097 subdivisions- dorsomedial (dmDR, dark blue), medial (mDR, tan), ventromedial (vmDR,
2098 green), and dorsolateral (dlDR, light blue). (B-D) (top) Distribution of normalized
2099 transcript expression of *Pax5* (B), *Satb2* (C) or *Nr2f2* (D) within *Pet1* neuron subtypes
2100 and (bottom) the percentage of counted *Pet1* neurons immunoreactive for PAX5 (B),

2101 SATB2 (C) or NR2F2 (D) that are arising from *Vglut3::cre; Pet1::Flpe* neurons (dark
2102 grey) in comparison to the subtractive *Pet1* population (light grey). (B'-D') Bar graph
2103 depicting the percentage of *Pet1* neurons immunopositive for PAX5 (B'), SATB2 (C') or
2104 NR2F2 (D') in anatomical subdivisions of the DR from rostral to caudal. n=2- 4
2105 depending on rostral to caudal section, bar graph depicting mean with SEM. (B''-D'')
2106 Representative coronal confocal image depicting a region of the DR with *Pet1* neurons
2107 immunopositive for PAX5 (B''), SATB2 (C'') or NR2F2 (D''). *Vglut3::cre;Pet1::Flpe* cells
2108 are shown in green, subtractive *Pet1* cells in red, and antibody of interest in blue. (E)
2109 Coronal brainstem schematics depicting the anatomical distribution of *Pet1* neurons
2110 (top) expressing PAX5 and NR2F2, or (bottom) that are expressing *Gad2-Tph2, Vglut3-*
2111 *Tph2,* or *Vglut3* only from rostral (right) to caudal (left).

2112 Figure 5: *P2ry1::cre; Pet1::Flpe* neurons project throughout the ventricles and their fibers
2113 are in close apposition to proliferating cells in the SVZ and RMS. (A) Flat mount of the
2114 lateral wall of the lateral ventricle of a *P2ry1::cre;Pet1::Flpe;Ai65* animal, where
2115 *P2ry1::cre;Pet1::Flpe* fibers are in grey. Scale bar = 100 µm. (B-E) High magnification
2116 confocal images from regions of the lateral wall represented in red boxes in A. Scale bar
2117 (B) = 100 µm. (F) 3D brain schematic showing the *P2ry1::cre;Pet1:Flpe* cell bodies (dark
2118 orange) in the caudal part of the DR (light orange) and fibers (dark orange) projecting
2119 through the ventricles (grey) and along the migrating neuroblasts of the rostral migratory
2120 stream (RMS, blue). (G-H) Coronal confocal images depicting *P2ry1::cre;Pet1::Flpe*
2121 fibers (orange) from *P2ry1::cre;Pet1::Flpe;Ai65* animals in the SVZ (G) and RMS (H).
2122 Proliferating cells labeled with Ki67 (grey) and migrating neuroblasts labeled with
2123 doublecortin (DCX, blue). Scale bar (G, H) = 50 µm.

2124 Figure 5 – figure supplement 1: The caudal dorsal raphe is the major *Pet1* neuron
2125 source of supra-ependymal fibers. (A) Schematic depicting unilateral injection of AAVrg-
2126 hSyn-Cre into the lateral ventricle of either *Pet1::Flpe;FrePe* (EGFP marked cells
2127 expressing both Cre and Flpe and mCherry expressing *Pet1::Flpe* subtractive
2128 population) or *Pet1::Flpe;Ai65* (TdTomato marked cells expressing both Cre and Flpe),
2129 leading to labeling of *Pet1* cells in the caudal dorsal raphe predominantly, and a smaller
2130 group in the median raphe. (B-C) Coronal confocal images of the caudal dorsal raphe
2131 from rostral (left) to caudal (right) in a *Pet1::Flpe;FrePe* (B) or *Pet1::Flpe;Ai65* (C) animal
2132 depicting *Pet1::Flpe* neurons with Cre expression after lateral ventricle injection of
2133 AAVrg-hSyn-Cre (green) and the *Pet1::Flpe* subtractive population (red, B only).

2134 Figure 6: *P2ry1::cre;Pet1::Flpe* neurons have a distinct firing phenotype. (A) Frequency-
2135 Current (F-I) curves show *P2ry1::cre; Pet1::Flpe* neurons (tdTomato$^+$ *P2ry1::IRES-*
2136 *cre;Pet1::Flpe;Ai65,* n=9; 3 animals; red circles) are less excitable than nearby caudal
2137 dorsal raphe non-*P2ry1::cre;Pet1::Flpe* populations (EGFP$^+$ *P2ry1::IRES-*
2138 *cre;Pet1::Flpe;RC::FL-hM3Dq,* n=8; 3 animals; black squares) or neurons from the
2139 dorsomedial and dorsolateral dorsal raphe *Gad2::cre;Pet1::Flpe* population (tdTomato$^+$
2140 *Gad2::IRES-cre;Pet1::Flpe;Ai65*, n=12; 2 animals; blue circles) $p<0.0001$ Kruskal-Wallis
2141 test. (B) Example voltage traces from neuron patch-clamp recordings showing different
2142 firing types, specifically a neuron that started firing action potentials with (1) short latency
2143 (mean= 17.32 ms ± 6.61 at 200 pA), in response to 750 ms current pulses, (2) medium
2144 latency (mean= 64.18 ms ± 9.8 at 200 pA), (3) long latency (mean= 476.55 ms ± 223.64
2145 at 200 pA), or (4) short latency (mean= 12.6 ms ± 5.9 at 200 pA) with spike-frequency
2146 adaptation. (C) Heat map shows the percentage of cells recorded from each genotype
2147 corresponding to each firing type, note all recorded *P2ry1::cre; Pet1::Flpe* neurons
2148 belong to type 3.

2149 Figure 6- figure supplement 1: Key membrane properties distinguish serotonergic
2150 neuron firing types. Referenced groups are the same as described in Figure 6B; all
2151 *P2ry1::IRES-cre; Pet1::Flpe;RC::Ai65* neurons belong to group 3. (A) Scatterplot of
2152 rheobase (in pA) exhibited by each cell of the corresponding firing type. (B) Scatterplot
2153 of the latency of each cell to fire the first action potential after the onset of the
2154 depolarizing current pulse by the corresponding firing type. (C) Same as B except firing
2155 type 3 was split into subgroups 3a and 3b, based on bi-modality visible in B. (D)
2156 Scatterplot of the maximum firing frequency (in Hz) exhibited by each cell of the
2157 corresponding firing type. (E) Scatterplot of the membrane resistance (in MΩ), exhibited
2158 by each cell of the corresponding firing type. (F) Scatterplot of the average half-width of
2159 the action potential of each firing type at maximum firing rate (in ms). Dashed lines
2160 indicate the median. Asterisks indicate statistical significance, Kruskal-Wallis test *$p <$
2161 0.05, **$p < 0.01$, ***$p < 0.001$, ****$p < 0.0001$.

2162 Figure 7: Correspondence of serotonin subtypes identified in previous studies (Y-axis) to
2163 the fourteen 10X scRNA-seq clusters identified in this study (X-axis). The size of the dot
2164 indicates the percentage of single cells from the original cluster that are attributed to a
2165 given reference cluster.

2166 Figure 7 - figure supplement 1: The number of cells sampled and the max UMIs per cell
2167 influence the number of clusters found in the dataset. (A) Box plot depicting the number
2168 of clusters found at resolution 0.9 (Y-axis) when then number of cells included in the
2169 analysis was varied (X-axis). Cells were randomly sub-sampled to include 200 to 2300
2170 cells (in intervals of 100) and the analysis was repeated twenty times per iteration. (B)
2171 Box plots depicting the number of clusters found at resolution 0.9 (Y-axis), when the max
2172 UMIs per cell was varied. UMIs were randomly sub-sampled from 500 to 100,000, at
2173 intervals of 500, and the analysis was completed twenty times per iteration. (C) Box plot
2174 depicting the distribution of the number of clusters found when the dataset was randomly
2175 downsampled to 750 cells and 2500 UMIs per cell (analysis repeated 20 times).

2176 Figure 8: Fourteen *Pet1* subtypes in the DR can be defined by the combinatorial
2177 expression of transcription factors and other markers and have distinct anatomical
2178 organization. (A) Molecular markers (neurotransmitters (NTs), transcription factors (TFs),
2179 and other markers) on the left half of the table, with increasing specificity from left to
2180 right, that combinatorically define each identified *Pet1* subtype (colored column).
2181 Anatomical biases of each cluster are described on the right, with increasing specificity
2182 from right to left. Figure 8- figure supplement 1 outlines the combination of information
2183 used to inform the proposed anatomical bias. Note, cluster numbers have been re-
2184 ordered to highlight anatomical groupings. (B) Schematic depicting the anatomical
2185 distribution of each subtype based on the bias indicated in (A). B7 and B6 refer to the
2186 original Dahlström and Fuxe nomenclature for describing distinct anatomical clusters of
2187 5-HT neurons. The asterisks after B6 in A and B are to indicate that some authors only
2188 consider B6 to encompass the dorsal part of what we refer to as the caudal DR.

2189 Figure 8- figure supplement 1: Anatomical bias of *Pet1* DR subtypes can be inferred by a
2190 combination of histology, single cell RNAseq, data from previously published papers,
2191 and Allen Mouse Brain atlas RNA in situ hybridization data. Table depicting each cluster
2192 (column 1) and its proposed anatomical bias (column 2) based on a combination of
2193 analysis of histology from intersectional lines and single cell RNA seq (columns 3 and 5),
2194 immunostaining and in-situ hybridization (column 4), computational mapping of our
2195 subtypes to previously published datasets (column 6), and qualitative analysis of the
2196 anatomical distribution of subtype marker genes from the Allen Brain Atlas data set
2197 (column 7). As in Figure 8, B7 and B6 here refer to the original Dahlström and Fuxe
2198 nomenclature for describing distinct anatomical clusters of 5-HT neurons, and the

asterisk after B6 is to indicate that some authors only consider B6 to encompass the dorsal part of what we refer to as the caudal DR. † after "*Npy2r::cre; Pet1::Flpe* rDR scRNAseq and histology" in row 6 is to indicate that, while *Npy2r::cre; Pet1::Flpe* histology shows EGFP positive cell bodies in both dorsal and ventral aspects of the rDR, the scRNAseq data, combined with other evidence given, suggest a more dorsal bias for cluster six DR *Pet1* neurons. †† after "*Sert::cre;Pet1::Flpe* vmDR" in row 11 is to indicate that, while manually sorted *Sert::cre;Pet1::Flpe* vmDR scRNAseq libraries did not map to cluster 11 overall, cluster 11 neurons nonetheless express several marker genes enriched in the vmDR, which together with other evidence given in the table suggests a vmDR bias.

Supplemental Excel Spreadsheet: The "all_subgroup_markers" worksheet displays the output of the Seurat FindAllMarkers function. Column one is the gene symbol, column two is the p-value given by the Wilcoxon Rank Sum test, column three is the average "log fold change" (i.e. log-fold difference in transcript abundance between the in-group and out-group), where a positive value indicates that a gene is expressed at a higher level in a given cluster relative to all other clusters, and a negative value indicates that a gene is expressed at a lower level. Column four is the percent of cells within a particular cluster in which the gene was detected, column five is the percent of cells within all other clusters in which a gene was detected, column six gives the Bonferroni-corrected p-value, and column seven indicates the cluster in which the given gene is a positive or negative marker. Note, not all enriched genes are unique to only one cluster, as more similar clusters will share subsets of enriched genes. The "sig_var_genes" worksheet lists the top two thousand highest "standardized variance" genes, i.e. genes that vary significantly more than expected based on mean expression.

Figure 1

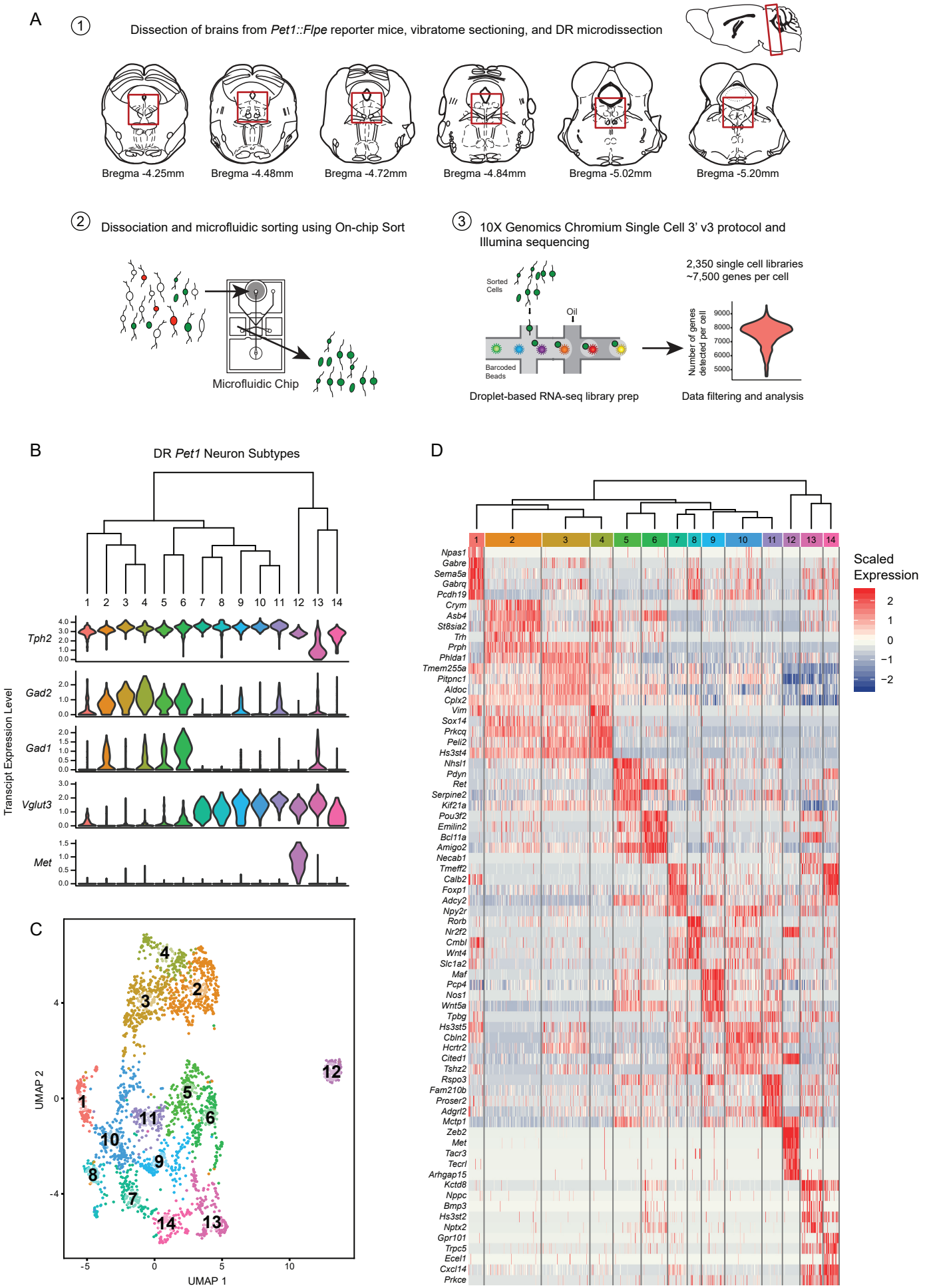
A
1
Dissection of brains from Pet1::Flpe reporter mice, vibratome sectioning, and DR microdissection
Bregma -4.25mm
Bregma -4.48mm
Bregma -4.72mm
Bregma -4.84mm
Bregma -5.02mm
Bregma -5.20mm
2
Dissociation and microfluidic sorting using On-chip Sort
Microfluidic Chip
3
10X Genomics Chromium Single Cell 3' v3 protocol and Illumina sequencing
Sorted Cells
Oil
Barcoded Beads
Droplet-based RNA-seq library prep
2,350 single cell libraries
~7,500 genes per cell
Number of genes detected per cell
Data filtering and analysis
B
DR Pet1 Neuron Subtypes
Tph2
Gad2
Gad1
Vglut3
Met
Transcipt Expression Level
C
UMAP 1
UMAP 2
D
Scaled Expression
Npas1
Gabre
Sema5a
Gabrq
Pcdh19
Crym
Asb4
St8sia2
Trh
Prph
Phlda1
Tmem255a
Pitpnc1
Aldoc
Cplx2
Vim
Sox14
Prkcq
Peli2
Hs3st4
Nhsl1
Pdyn
Ret
Serpine2
Kif21a
Pou3f2
Emilin2
Bcl11a
Amigo2
Necab1
Tmeff2
Calb2
Foxp1
Adcy2
Npy2r
Rorb
Nr2f2
Cmbl
Wnt4
Slc1a2
Maf
Pcp4
Nos1
Wnt5a
Tpbg
Hs3st5
Cbln2
Hcrtr2
Cited1
Tshz2
Rspo3
Fam210b
Proser2
Adgrl2
Mctp1
Zeb2
Met
Tacr3
Tecrl
Arhgap15
Kctd8
Nppc
Bmp3
Hs3st2
Nptx2
Gpr101
Trpc5
Ecel1
Cxcl14
Prkce

Figure 1- figure supplement 1

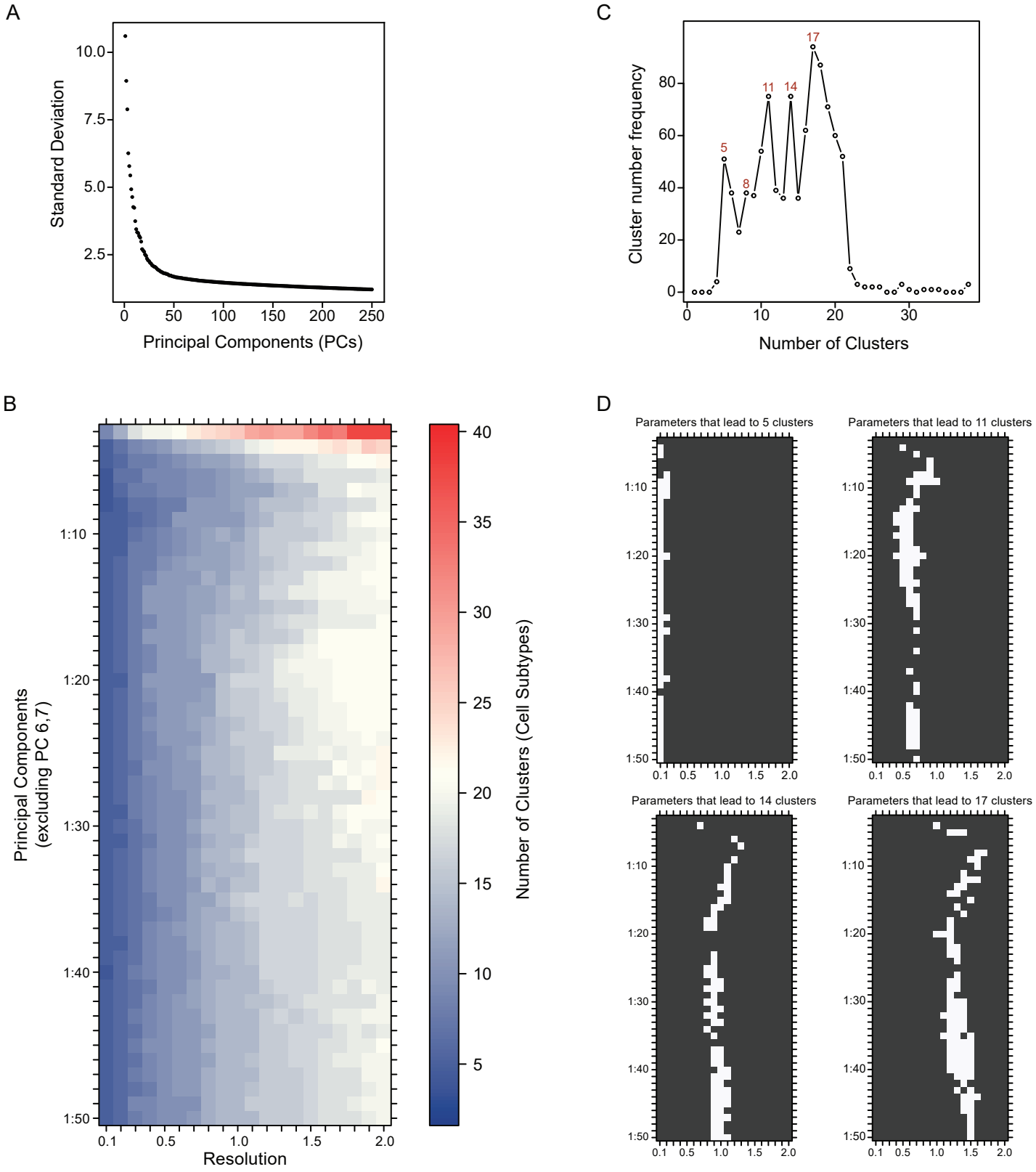

Figure 1- figure supplement 2

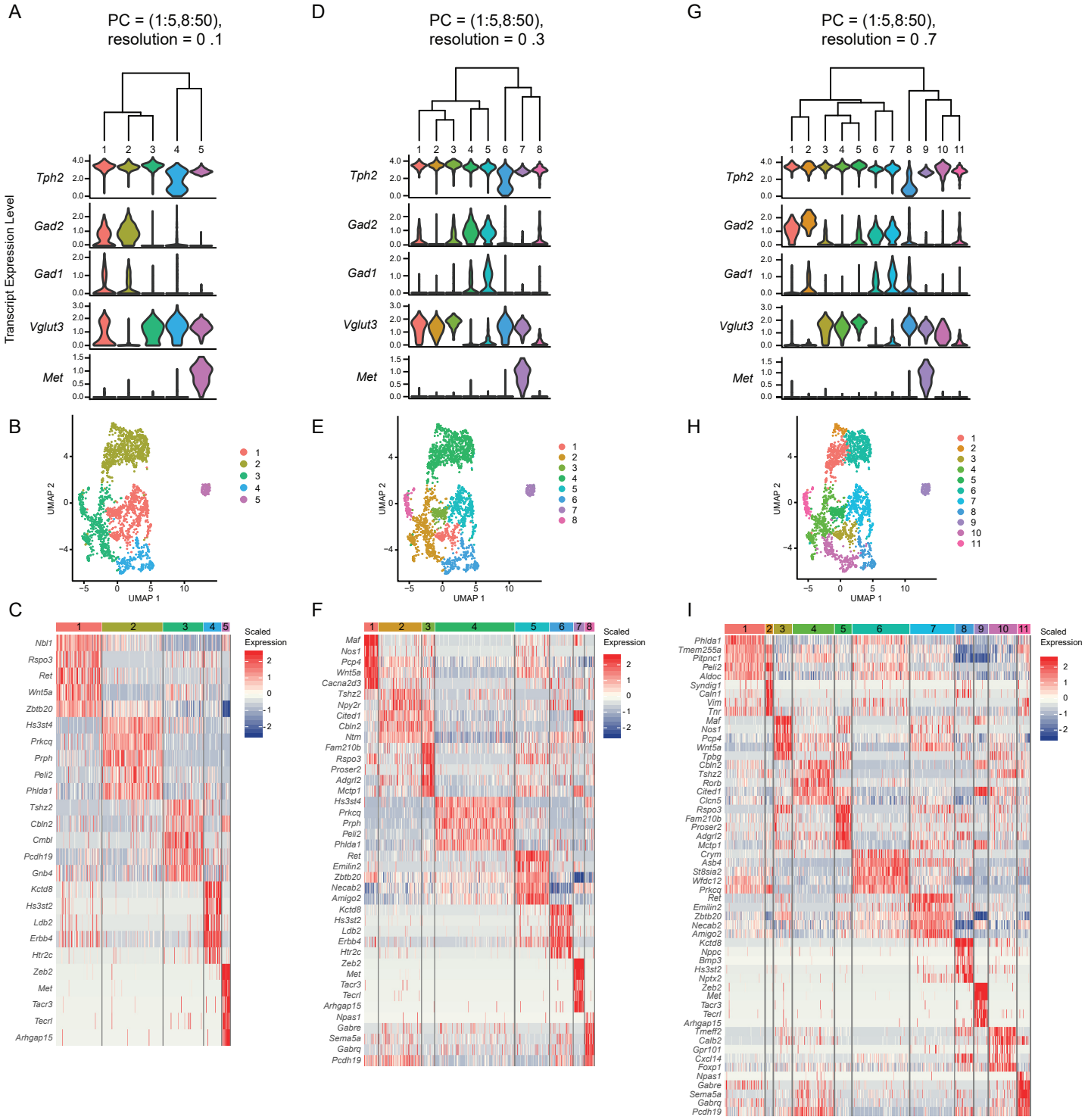

Figure 1- figure supplement 3

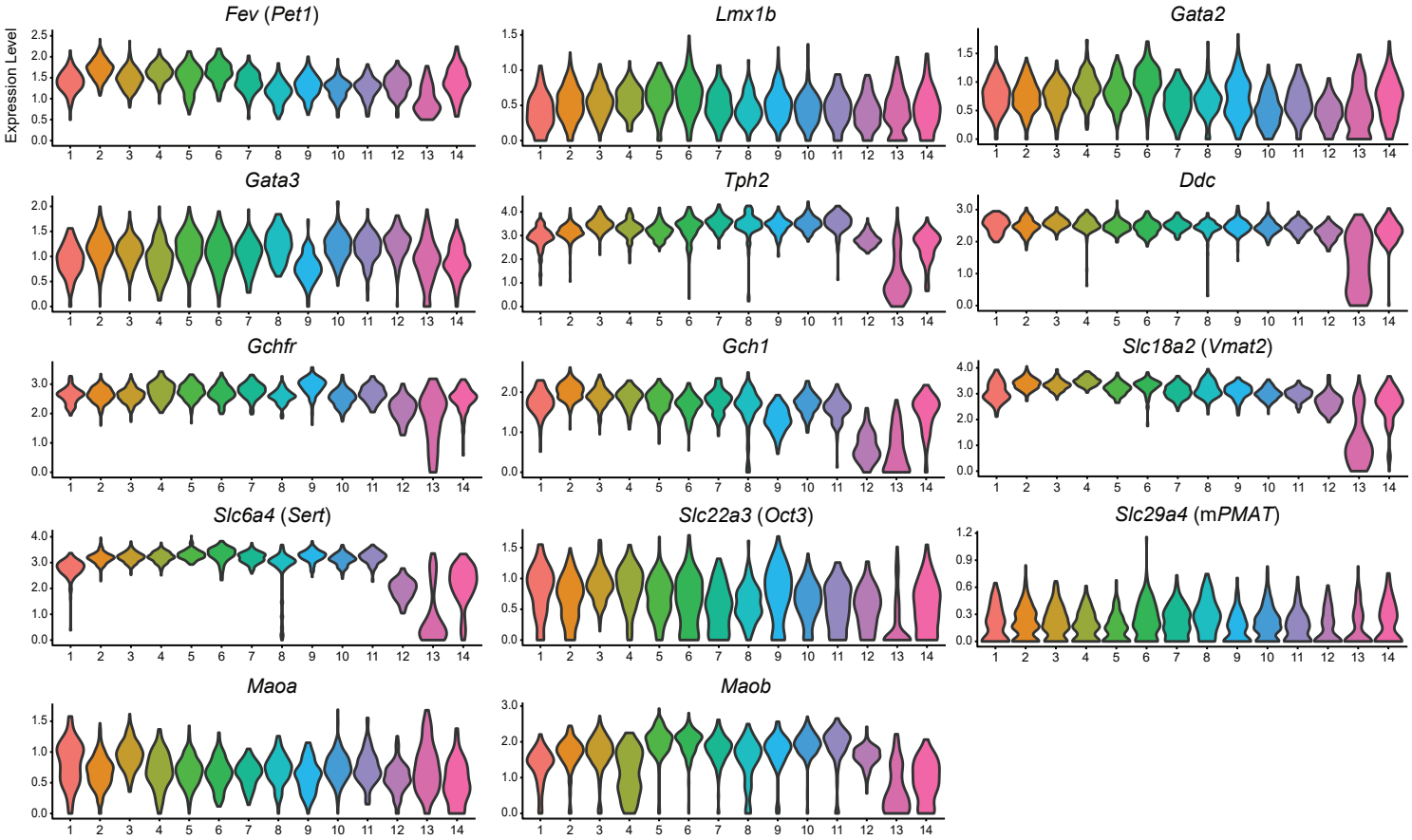

Figure 1- figure supplement 4

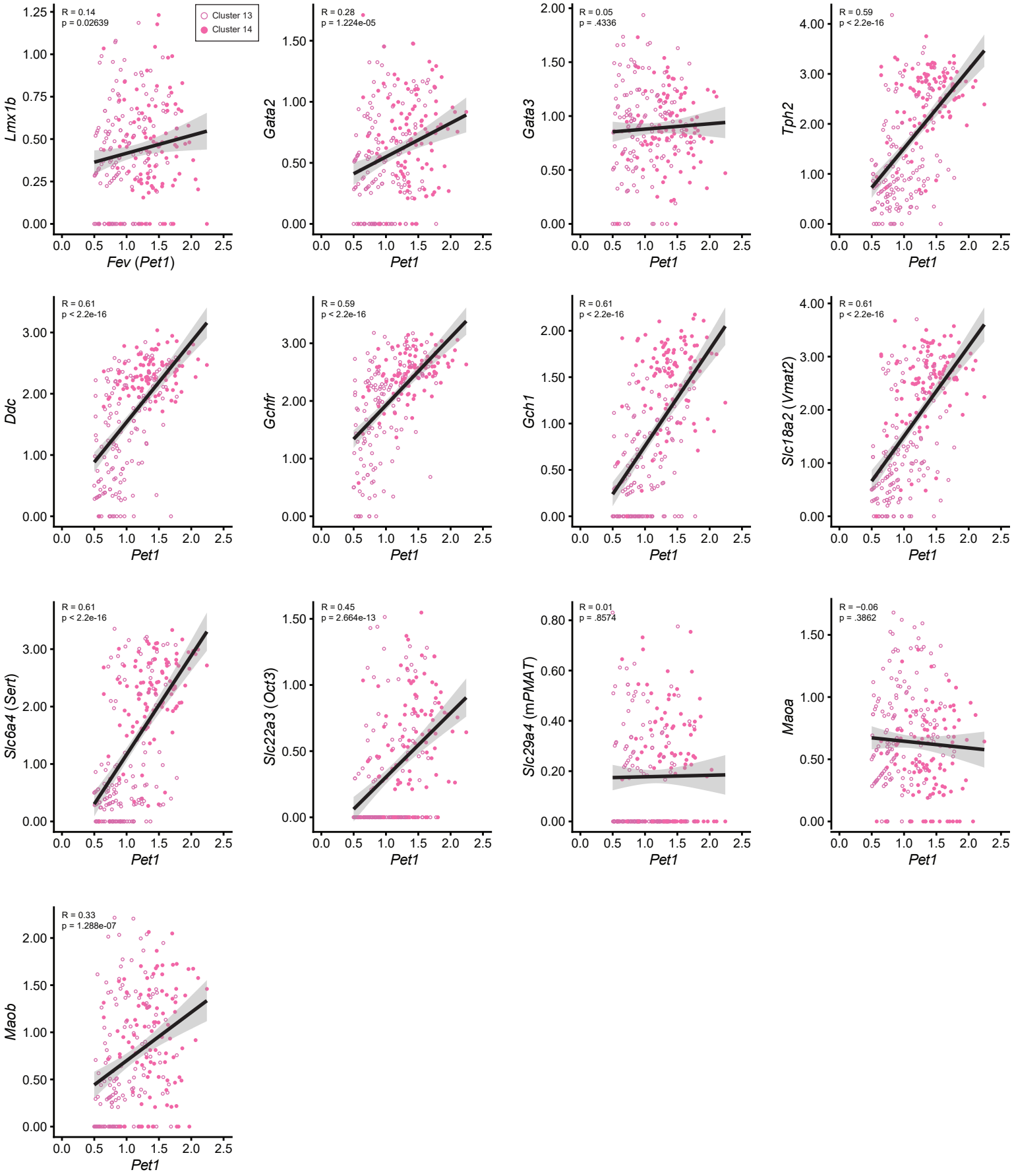

Figure 2

Transcription Factors
Fev
En1
En2
Nr3c1
Npas3
Pou3f1
Npas1
Pax5
Pou6f2
Klf5
Pou3f3
Sox14
Satb2
Barx2
Kit
Bcl11b
Esr2
Zbtb20
Pou3f2
Bcl11a
Id2
Scx
Zfp536
Foxp1
Lmo2
Sox5
Rorb
Mn1
Maf
Esr1
Mef2c
Foxa1
Mafb
Cited1
Nr2f2
Zeb2
Tox3
Lmo1
Uncx
Nr2f1
Lmo4
Tcf4
Egr1
Nfix
Nfib
Satb1
Ldb2
Sox4
Neurotransmitters and Neuropeptides
Tph2
Slc18a2
Chgb
Chga
Gad2
Gad1
Trh
Pdyn
Gal
Slc17a8
Ghrh
Adcyap1
Nos1
Crh
Nmb
Npb
Penk
Sst
Ionotropic Receptors
Gabrq
Gabre
Gria1
Grin3a
Gabrg3
Grin2a
Chrna4
Gabra2
Gabrg2
Gabra1
Gria3
Gabra5
Grik3
Cellular Calcium Ion Homeostasis
S100a10
S100a11
S100a16
Calb1
Necab2
Necab1
Calb2
Ryr2
S100b
Ryr3
G Protein-Coupled Receptors
Gabbr1
Adra1b
Adra2c
Htr1a
Htr1b
Htr1d
Hcrtr1
Hrh1
Grm1
Adra2a
Hrh3
Gpr149
Prokr2
Npy2r
Grm7
Htr5b
Ptger3
Cckar
Gpr35
Gpr88
Grm8
Hcrtr2
Crhr2
Oxtr
Calcr
Chrm2
Grm5
Lpar1
S1pr3
P2ry1
Rxfp1
Tacr3
Oprm1
Ptger4
Chrm1
Gabbr2
Cnr1
Htr2c
Gpr22
Htr7
Sstr2
Sstr1
Tacr1
Oprk1
Galr1
Gpr101
Plasma Membrane Ion Channels
Scn9a
Cacng3
Kcnh7
Kcnq3
Kcnc4
Cacng4
Kcnip1
Clic1
Scn7a
Kcng4
Kcnn3
Cacna1e
Cacna1i
Kcnab1
Kcnj4
Kcnc1
Hcn1
Kcnb2
Cachd1
Kcnc2
Cacna2d3
Kcnf1
Cacng5
Kcna1
Kcnj12
Kcnd2
Kcna4
Trpc3
Kctd8
Kcnk2
Kcnip4
Kctd4
Kcnh5
Kcnh8
Trpc5
Regulators of Heparan Sulfate Proteoglycans
Hs3st4
Hs3st5
Ndst3
Hs3st1
Ext1
Ndst4
Hs3st6
Sulf2
Hs3st2
Hs3st3a1
Sulf1
Regulators of Neuron Projections and Synaptic Connectivity
Fgf13
Pcdh19
Sema5a
Cdh11
Cdh18
Pcdh18
Prph
Robo2
Cdh13
Sema6a
Cdh22
Flrt2
Cdh4
Plxna2
Plxnd1
Cntn4
Amigo2
Robo1
Nptx1
Fgf18
Cbln1
Pcdh17
Wnt4
Wnt5a
Sema6d
Plxna4
Pcdh15
Fgf9
Ntn1
Cdh7
Pcdh7
Ntng1
Cbln2
Sema3c
Epha7
Fgf1
Epha6
Pcdh20
Fgf11
Epha3
Cbln4
Cdh8
Pcdh8
Ephb1
Sema3e
Reln
Epha4
Fgf10
Pcdh11x
Efna5
Efnb3
Slit2
Nrp2
Sema3d
Nrp1
Efnb2
Kinases and Kinase Inhibitors
Prkcb
Pkib
Prkca
Prkcq
Ret
Igf1r
Cdkn1a
Prkcd
Lats2
Ror2
Met
Camk2d
Erbb4
Prkg1
Prkg2
Average Expression
Percent Expressed
UMAP 1
UMAP 2

Figure 3

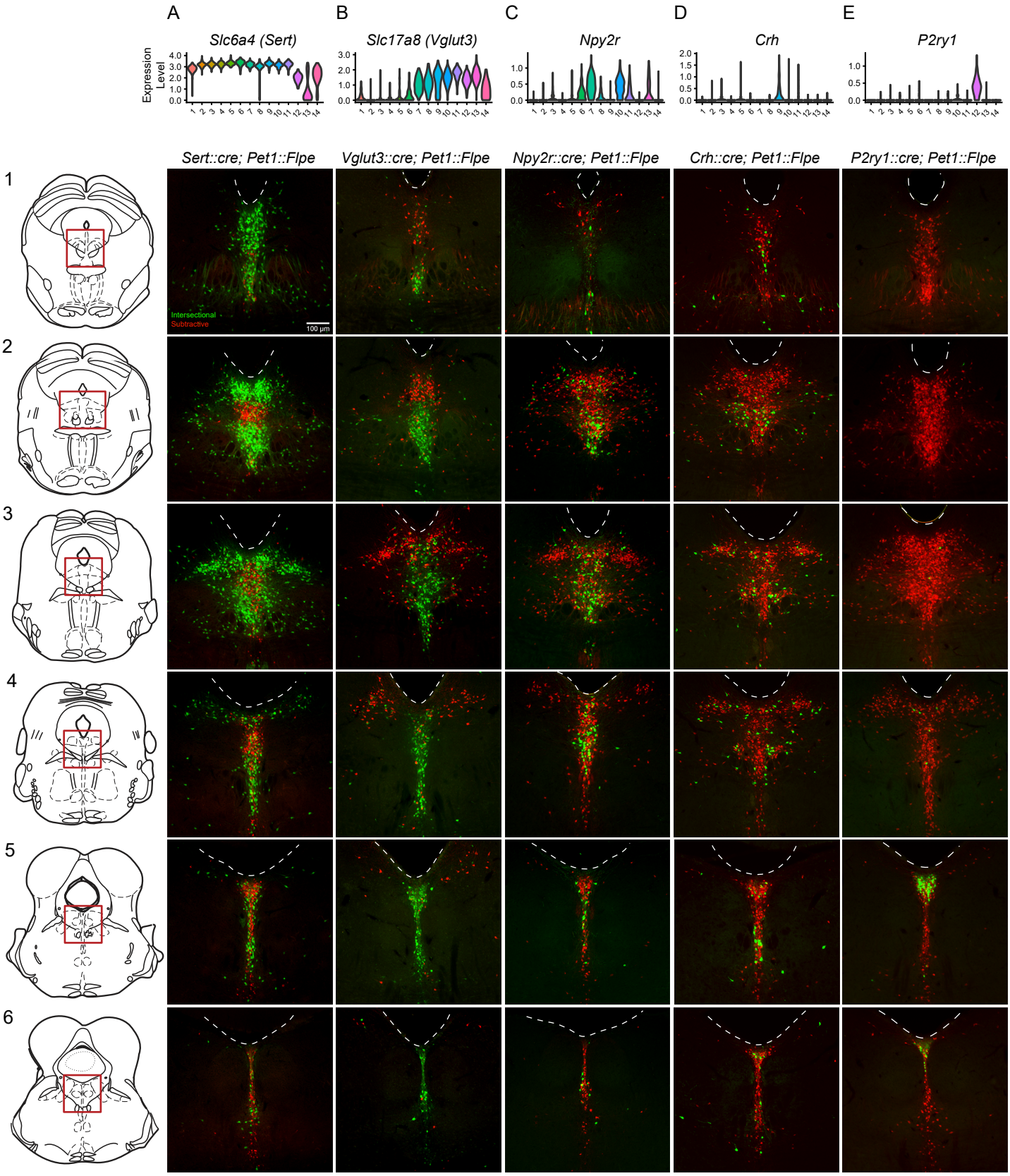
A
B
C
D
E
Slc6a4 (Sert)
Slc17a8 (Vglut3)
Npy2r
Crh
P2ry1
Expression Level
Sert::cre; Pet1::Flpe
Vglut3::cre; Pet1::Flpe
Npy2r::cre; Pet1::Flpe
Crh::cre; Pet1::Flpe
P2ry1::cre; Pet1::Flpe
1
2
3
4
5
6
Intersectional
Subtractive
100 µm

Figure 3 - figure supplement 1

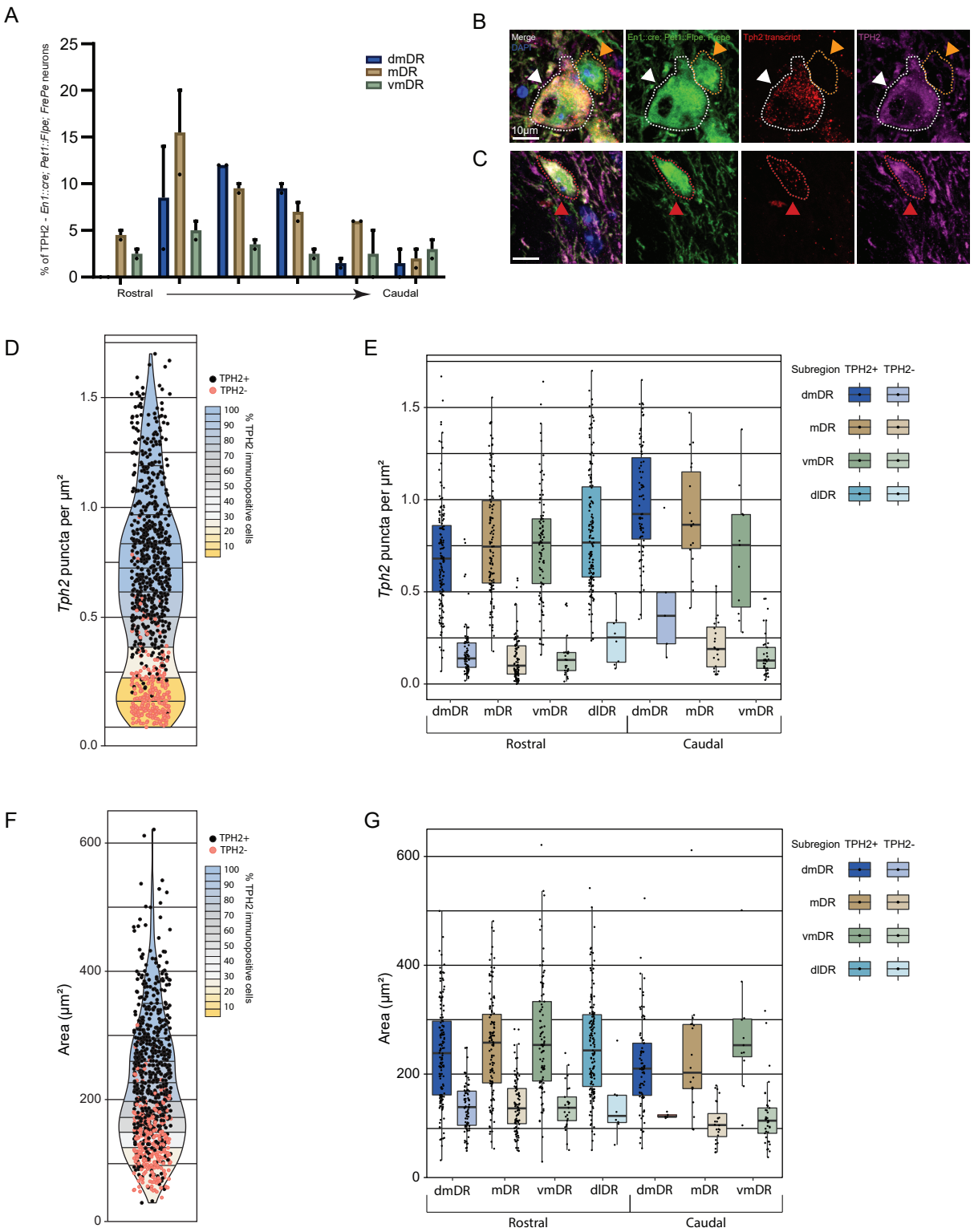

Figure 3 - figure supplement 2

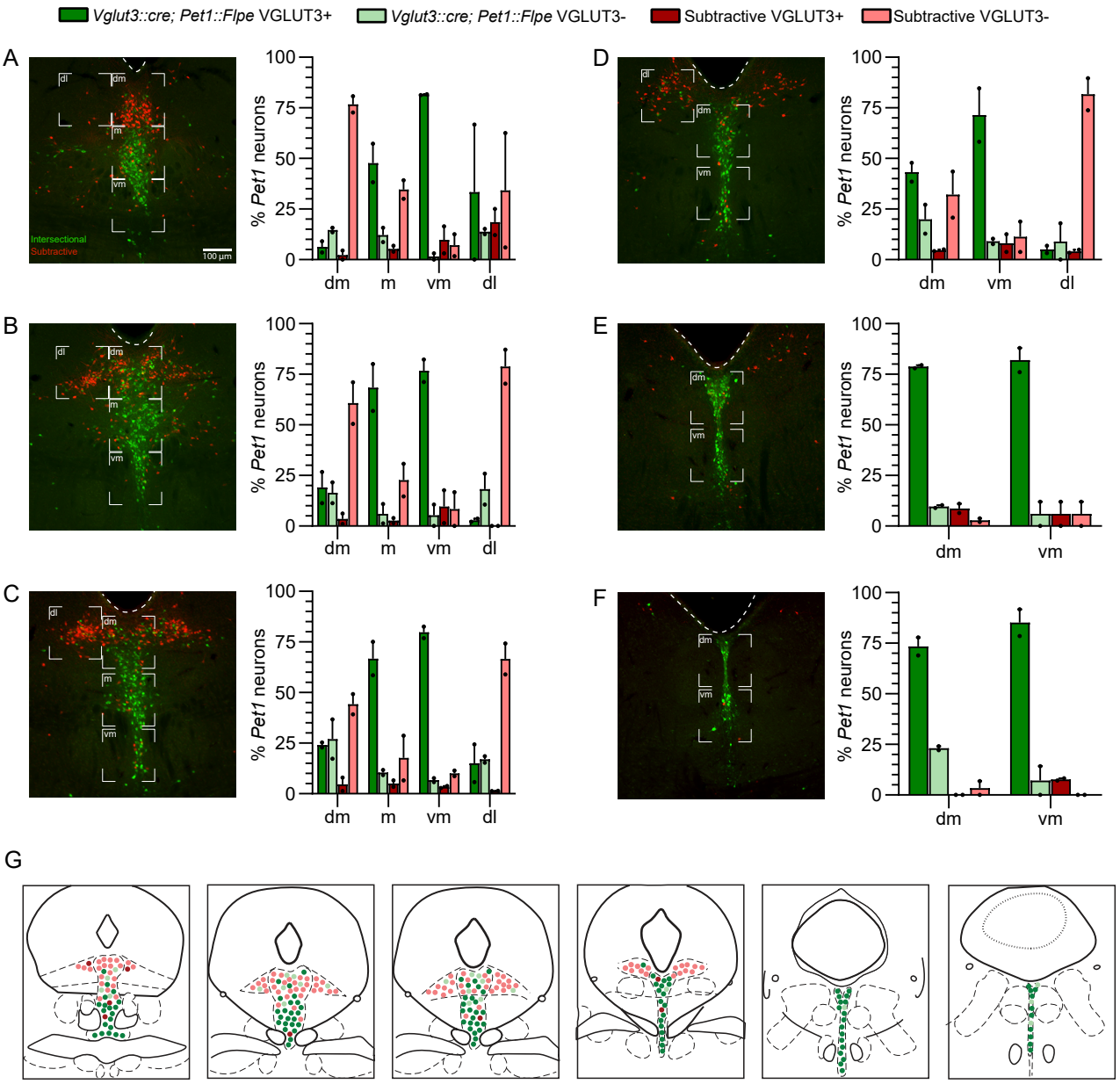

Figure 4

A

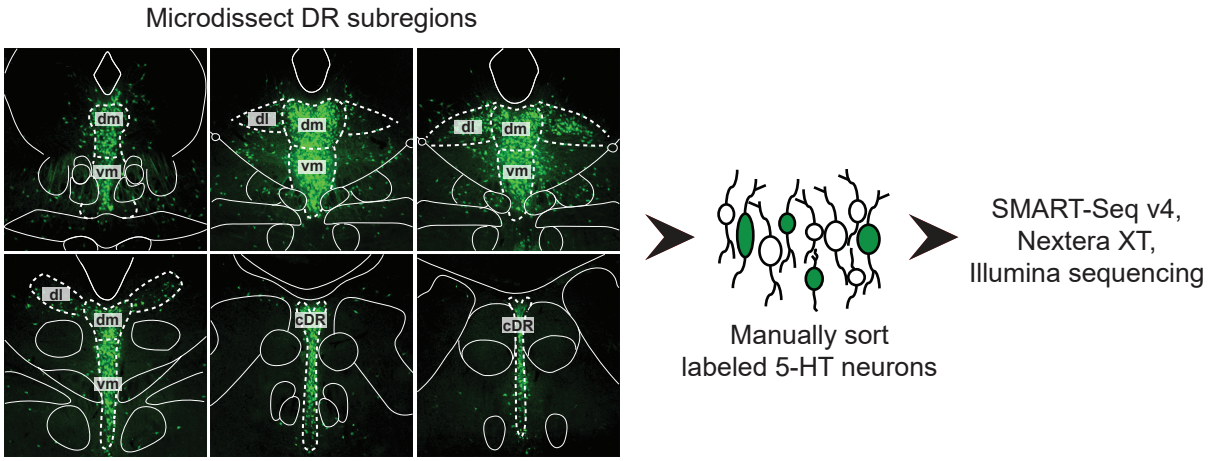
Microdissect DR subregions
dm
vm
dl
cDR
Manually sort
labeled 5-HT neurons
SMART-Seq v4,
Nextera XT,
Illumina sequencing

B

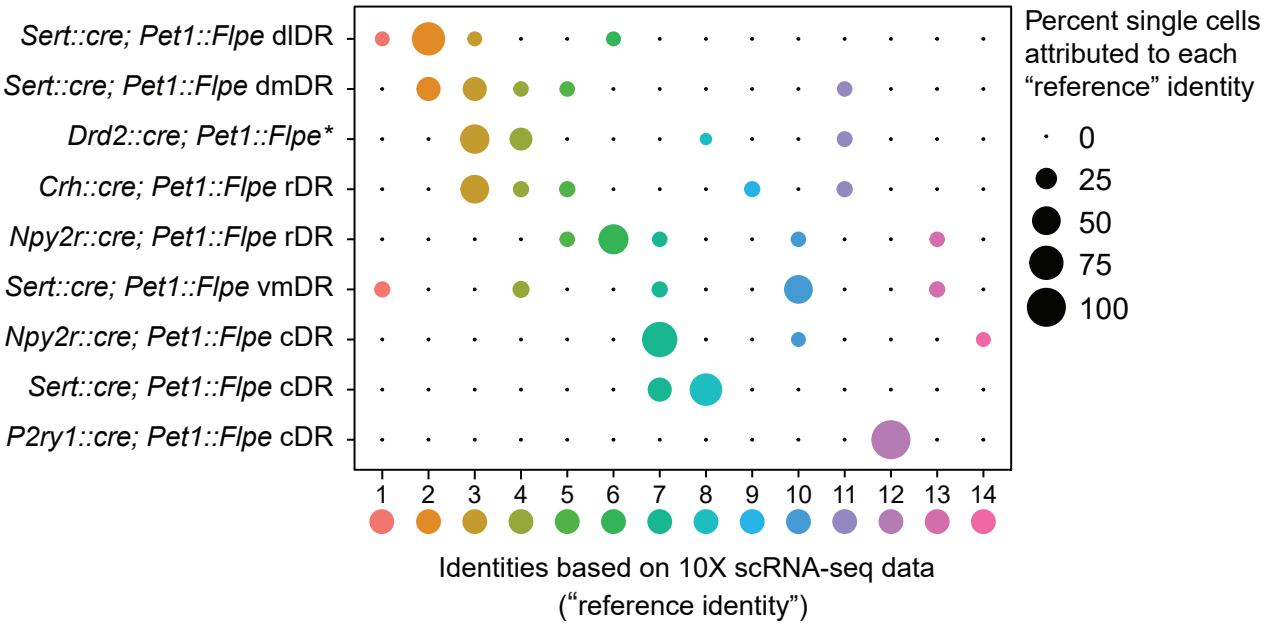
Sert::cre; Pet1::Flpe dlDR
Sert::cre; Pet1::Flpe dmDR
Drd2::cre; Pet1::Flpe*
Crh::cre; Pet1::Flpe rDR
Npy2r::cre; Pet1::Flpe rDR
Sert::cre; Pet1::Flpe vmDR
Npy2r::cre; Pet1::Flpe cDR
Sert::cre; Pet1::Flpe cDR
P2ry1::cre; Pet1::Flpe cDR
1 2 3 4 5 6 7 8 9 10 11 12 13 14
Identities based on 10X scRNA-seq data
("reference identity")
Percent single cells
attributed to each
"reference" identity
0
25
50
75
100

Figure 4 - figure supplement 1

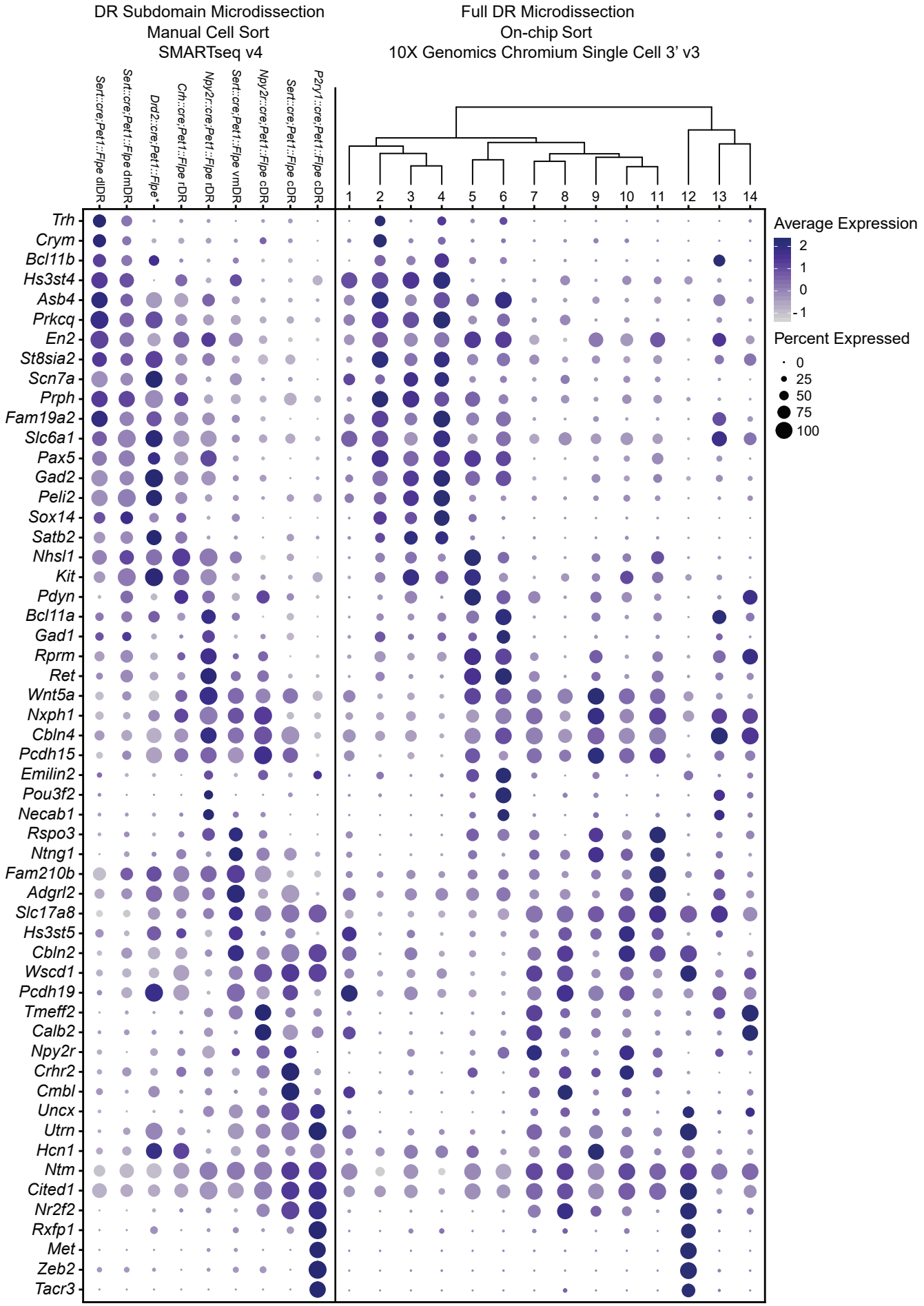

Figure 4 - figure supplement 2

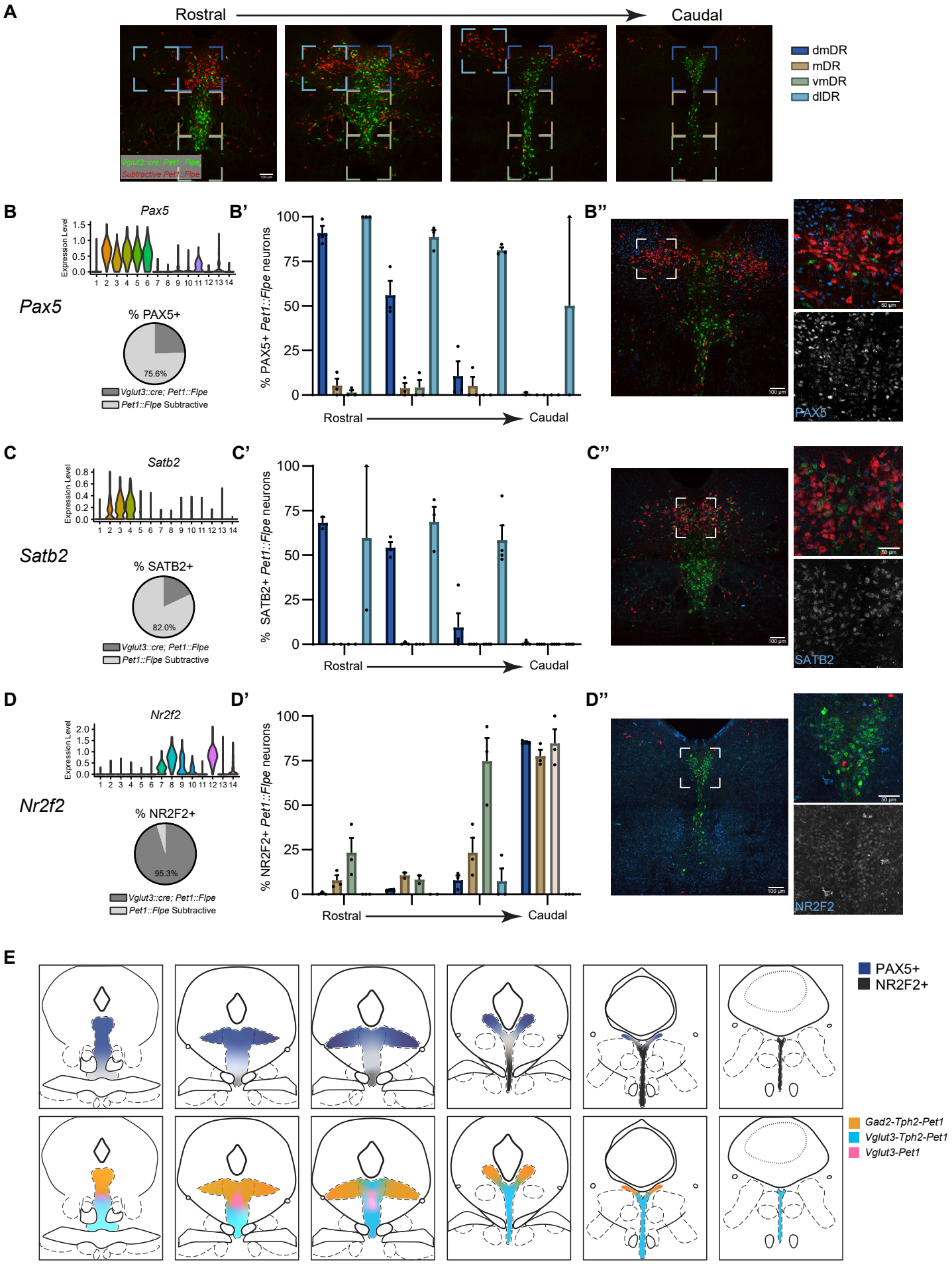

Figure 5

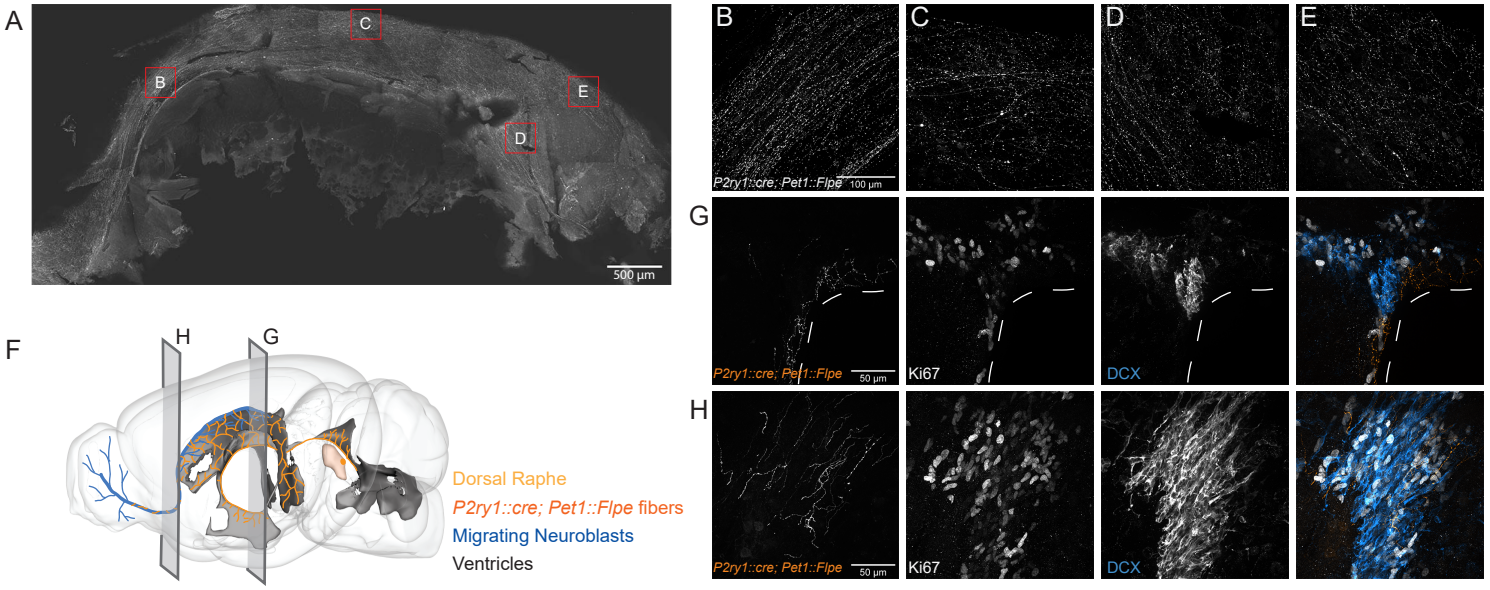
A
B
C
D
E
500 µm
F
H
G
Dorsal Raphe
P2ry1::cre; Pet1::Flpe fibers
Migrating Neuroblasts
Ventricles
B
C
D
E
P2ry1::cre; Pet1::Flpe
100 µm
G
P2ry1::cre; Pet1::Flpe
50 µm
Ki67
DCX
H
P2ry1::cre; Pet1::Flpe
50 µm
Ki67
DCX

Figure 5- figure supplement 1

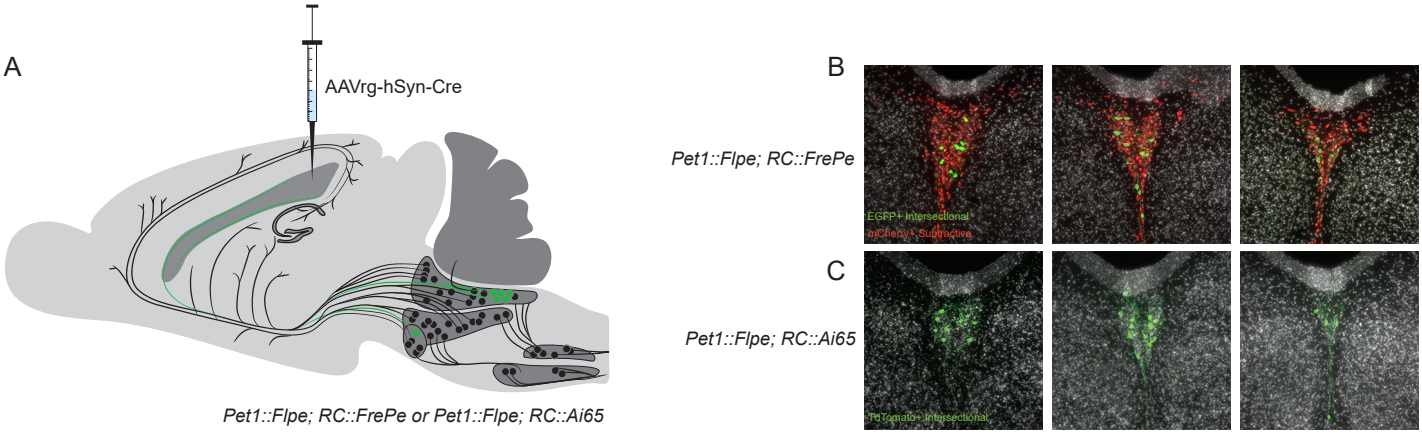

Figure 6

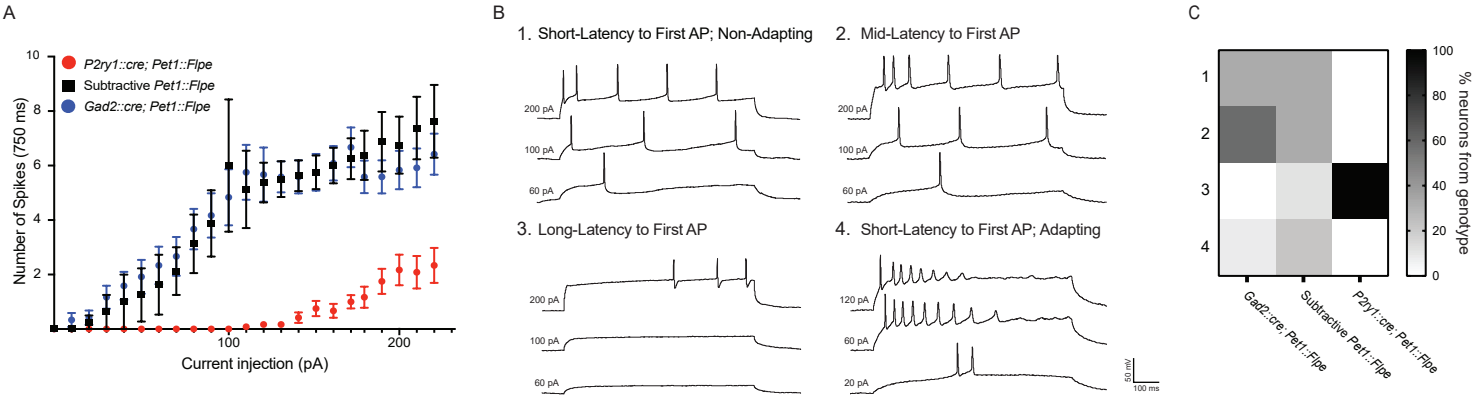
A
P2ry1::cre; Pet1::Flpe
Subtractive Pet1::Flpe
Gad2::cre; Pet1::Flpe
Number of Spikes (750 ms)
Current injection (pA)
B
1. Short-Latency to First AP; Non-Adapting
2. Mid-Latency to First AP
3. Long-Latency to First AP
4. Short-Latency to First AP; Adapting
200 pA
100 pA
60 pA
120 pA
20 pA
50 mV
100 ms
C
% neurons from genotype
Gad2::cre; Pet1::Flpe
Subtractive Pet1::Flpe
P2ry1::cre; Pet1::Flpe

Figure 6- figure supplement 1

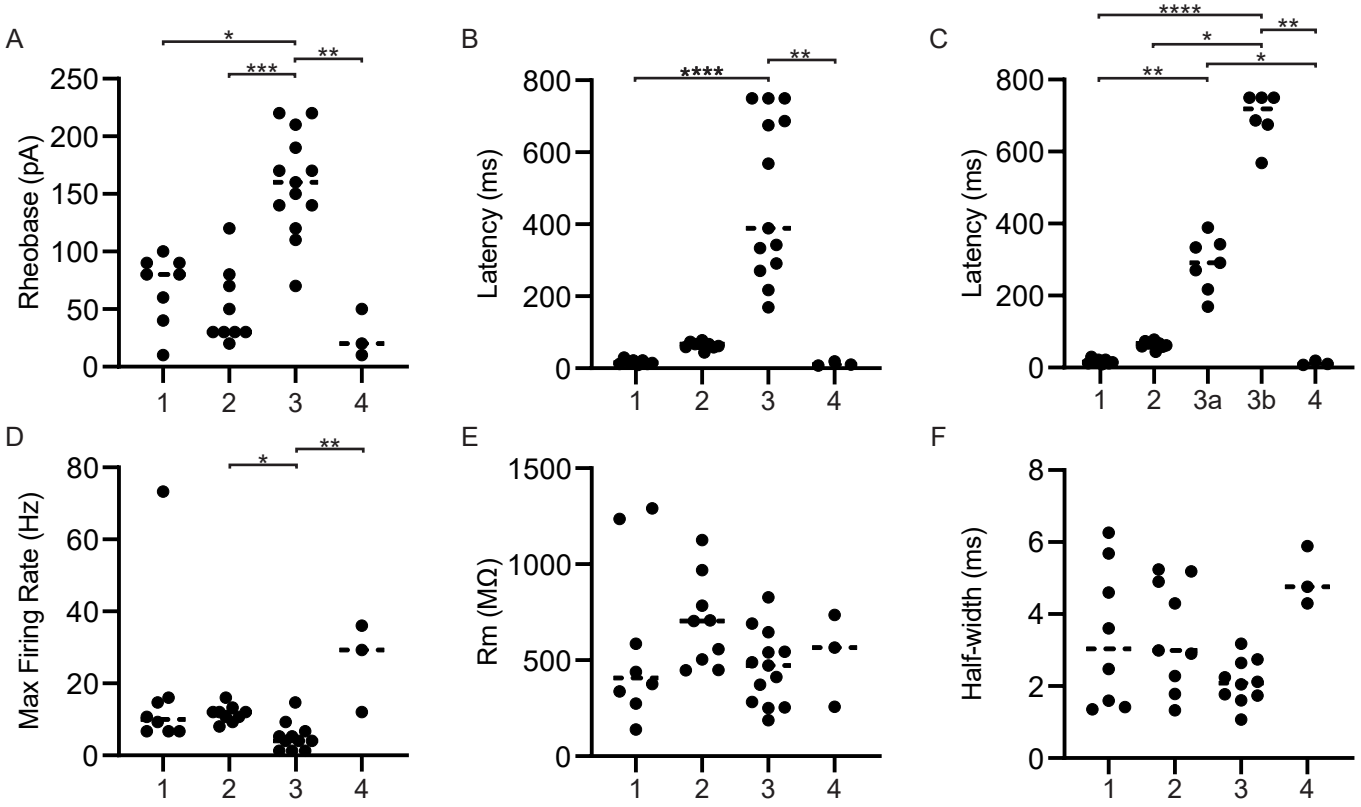

Figure 7

Projection of 10X data-based identities onto other data sets
Identities based on Huang, et al. 2019 and Ren,et al. 2019 data (used as "query")
Huang 5-HT I
Huang 5-HT II
Huang 5-HT III
Huang 5-HT IV
Huang 5-HT V
Huang Glu V
Ren DR 1
Ren DR 2
Ren DR 3
Ren DR 4
Ren DR 5
Ren DR 6
Ren cDR
Ren MR 1
1 2 3 4 5 6 7 8 9 10 11 12 13 14
Identities based on 10X data (used as "reference")
Percent single cells attributed to each "reference" identity
0
25
50
75
100

Figure 7- figure supplement 1

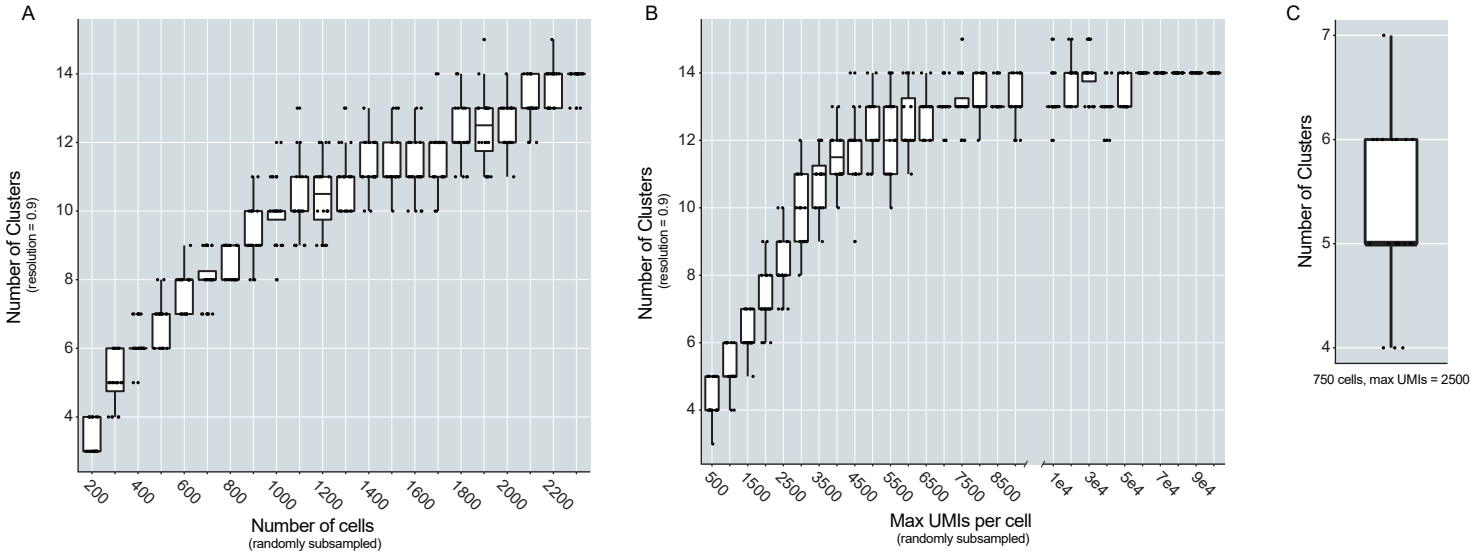

Figure 8

A

Molecular Organization | Anatomical Organization

NTs			TFs		Other Markers	Cluster	Subregion Bias		
Pet1	*Tph2*		*Npas1 Npas3*		*Gabre Gabrq*	1	Ventro-lateral	Rostral (B7)	Dorsal Raphe
		Gad2	high *Pax5*	*Sox14 Satb2*	*Crym Trh*	2	Dorso-lateral/ medial		
					Crct1	3	Dorsomedial		
					Vim	4			
					Pdyn Nhsl1	5			
				Pou3f2	*Emilin2*	6			
		Vglut3	low *Pax5*	*Foxa1*	*Rspo3*	11	Ventromedial		
			variable *Nr2f2*		*Maf Nos1*	9			
			Nr2f2		high *Cbln2*	10			
					Tmeff2	7		Caudal (B6*)	
				Rorb	*Wnt4*	8			
				Zeb2	*Met P2ry1*	12	Dorso-medial		
Pet1 low	*Tph2* low/variable		*Ldb2*	*Nfix Nfib*	*Kctd8 Nptx2*	13	Dorso-medial/ Medial	Distributed	
					Gpr101	14			

B

Schematic of Proposed Subregion Bias

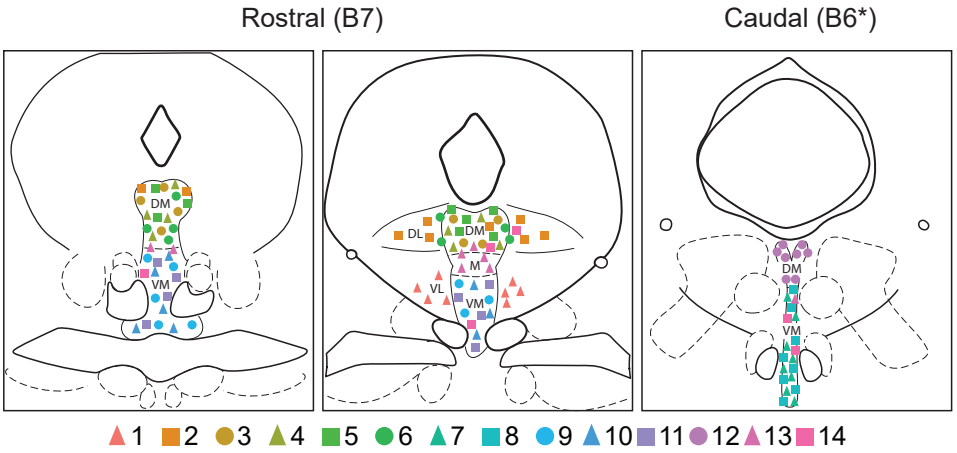

Figure 8- figure supplement 1

Subgroup	Proposed Anatomical Bias	**Vglut3::cre; Pet1::flpe Histology** (Fig 3)	**Immunostaining** (Fig 3 - supplement 1 and 2, and Fig 4- supplement 2)	**Manual scRNAseq and Histology** (Fig 3 and Fig 4)	**Previous Publications** Ren, et al. 2019[1], Huang, et al 2019[2] Okaty, et al 2015[3]	**Allen Brain Atlas In-Situ**
1	Rostral (B7) Ventrolateral	*Vglut3::cre; Pet1::Flpe* Subtractive Histology			*Tph2-Npas1* in-situ[1]	*Gabre* and *Gabrq*
2	Rostral (B7) Dorsolateral and Dorsomedial		PAX5 and SATB2	*Sert::cre; Pet1::Flpe* dlDR and dmDR scRNAseq	*Tph2/Sert-Trh* in-situ[1,2] 5-HT-I and II mapping[2]	*Trh* and *Crym*
3	Rostral (B7) Dorsomedial			*Sert::cre; Pet1::Flpe* dmDR scRNAseq	5-HT-II mapping[2]	*Kit*
4	Rostral (B7) Dorsomedial					*Prkcq*
5	Rostral (B7) Dorsomedial		PAX5		*Tph2-Ret* in-situ[1] *Sert-Pdyn* in-situ[2] 5-HT-III mapping[2]	*Pdyn*
6	Rostral (B7) Dorsomedial			*Npy2r::cre; Pet1::Flpe* rDR scRNAseq and histology[†]	*Tph2-Ret* in-situ[1] *Tph2-Gad1* in-situ[1] 5-HT-III mapping[2]	*Amigo2*
7	Caudal (B6*) Ventromedial	*Vglut3::cre; Pet1::Flpe* Intersectional Histology	VGLUT3 and TPH2 NR2F2	*Npy2r::cre; Pet1::Flpe* cDR scRNAseq and histology		
8	Caudal (B6*) Ventromedial			*Sert::cre; Pet1::Flpe* cDR scRNAseq and histology		*Rorb*
9	Rostral (B7) Ventromedial					*Nos1*
10	Rostral (B7) Ventromedial		VGLUT3 and TPH2	*Sert::cre; Pet1::Flpe* vmDR scRNAseq	5-HT-IV mapping[2]	
11	Rostral (B7) Ventromedial			*Rspo3, Foxa1, Proser2 Syt2* expression highest in *Sert::cre;Pet1::Flpe* vmDR[††]	*Tph2-Syt2* in-situ[1]	*Foxa1, Tpbg,* and *Pvrl3*
12	Caudal (B6) Dorsomedial		VGLUT3 and TPH2 NR2F2	*P2ry1:cre; Pet1::Flpe* cDR scRNAseq and histology	*Tph2-Met* in-situ[1] 5-HT-V mapping[2] MET immuno[3]	*Zeb2*
13	Dorsomedial and Medial		VGLUT3 and TPH2	*Sert::cre; Pet1::Flpe* subtractive histology		
14	Distributed		TPH2/*Tph2* immuno/in situ			*Gpr101*